NASA Technical Paper 3510

Aeroservoelastic Simulation of an Active Flexible Wing Wind Tunnel Model

---

Carey S. Buttrill, Barton J. Bacon, Jennifer Heeg, and Jacob A. Houck
Langley Research Center • Hampton, Virginia

David V. Wood
Unisys Corporation • Hampton, Virginia

National Aeronautics and Space Administration
Langley Research Center • Hampton, Virginia 23681-0001

April 1996

The use of trademarks or names of manufacturers in this report is for accurate reporting and does not constitute an official endorsement, either expressed or implied, of such products or manufacturers by the National Aeronautics and Space Administration.

Available electronically at the following URL address: http://techreports.larc.nasa.gov/ltrs/ltrs.html

Printed copies available from the following:

NASA Center for AeroSpace Information
800 Elkridge Landing Road
Linthicum Heights, MD 21090-2934
(301) 621-0390

National Technical Information Service (NTIS)
5285 Port Royal Road
Springfield, VA 22161-2171
(703) 487-4650

Contents

Symbols v

Abstract. 1

Introduction 1

Importance of Flutter in Airplane Design 1

Active Flexible Wing Program and Role of Simulation 2

Simulation Objectives and Results Organization 3

Wind Tunnel Model 3

Hot-Bench Overview 4

Hot-Bench Laboratory. 4

Hot-Bench Timescale 4

Mathematical Models 5

Turbulence Model 6

Implementation of modified Dryden model 6
Turbulence model parameters 7

Actuators 9

Structural Model 10

Aerodynamic Model 11

Aeroelastic Equations 12

Analog Filters 13

Tabulation of Mathematical Model Equations 14

Flutter Predictions and Frequency Response 14

Mathematical Model Summary. 15

Simulation Structure and Implementation 15

Model Reduction Method. 17

Rationale for Model Reduction. 17

Description 17

Numerical Robustness. 18

Error Properties 19

Application 19

Results of Reduction 20

Concluding Remarks 21

Appendix A—Derivation of Turbulence-Modeling Identities. 23

Appendix B—Explanation of Constant Power Assumption 24

Appendix C—Derivation of State Transition Equations 25

References 27

Tables 29

Figures 32

Symbols

$\mathbf{A}$	generic linear system plant matrix, (eq. (32))
$\mathbf{A}_0$	generalized aerodynamic stiffness matrix in rational function approximation
$\mathbf{A}_1$	generalized aerodynamic damping matrix in rational function approximation
$\mathbf{A}_2$	generalized aerodynamic mass matrix in rational function approximation
$\mathbf{A}_{2+m}$	generalized aerodynamic lag matrix in rational function approximation
$\mathbf{A}_0^{cc}$	$n_c \times n_c$ matrix where $\mathbf{A}_0^{cc}(i,j) = \partial\left(-F^{\delta_i}/\bar{q}\right)/\partial\delta_j$, F^{δ_i} is generalized aerodynamic force (hinge moment) on control mode *i*, δ_j is displacement of generalized coordinate representing control mode *j*, and $\bar{q}$ is dynamic pressure (eqs. (30))
$\mathbf{A}_1^{cc}$	$n_c \times n_c$ matrix where $\mathbf{A}_1^{cc}(i,j) = \partial\left(-F^{\delta_i}/\bar{q}\right)/\partial\left(\tau\dot{\delta}_j\right)$, F^{δ_i} is generalized aerodynamic force (hinge moment) on control mode *i*, $\dot{\delta}_j$ is rate of generalized coordinate representing control mode *j*, $\tau = \bar{c}/2V$, and $\bar{q}$ is dynamic pressure (eqs. (30))
$\mathbf{A}_2^{cc}$	$n_c \times n_c$ matrix where $\mathbf{A}_2^{cc}(i,j) = \partial\left(-F^{\delta_i}/\bar{q}\right)/\partial\left(\tau^2\ddot{\delta}_j\right)$, F^{δ_i} is generalized aerodynamic force (hinge moment) on control mode *i*, $\ddot{\delta}_j$ is acceleration of generalized coordinate representing control mode *j*, $\tau = \bar{c}/2V$, and $\bar{q}$ is dynamic pressure (eqs. (30))
$\mathbf{A}_{m+2}^{cc}$	$n_c \times n_c$ matrix where $\mathbf{A}_{m+2}^{cc}(i,j) = \partial\left(-\dot{x}^c_{a_{im}}\right)/\partial\dot{\delta}_j$, indicating effect of *j*th control mode rate on derivative of *m*th unsteady aerodynamic lag state associated with *i*th control mode, for $m = 1, 2, \ldots, n_{\text{lag}}$ (eqs. (30))
$\mathbf{A}_0^{cf}$	$n_c \times n_f$ matrix where $\mathbf{A}_0^{cf}(i,j) = \partial\left(-F^{\delta_i}/\bar{q}\right)/\partial\eta_j$, F^{δ_i} is generalized aerodynamic force (hinge moment) on control mode *i*, η_j is displacement of generalized coordinate representing elastic mode *j*, and $\bar{q}$ is dynamic pressure (eqs. (30))
$\mathbf{A}_1^{cf}$	$n_c \times n_f$ matrix where $\mathbf{A}_1^{cf}(i,j) = \partial\left(-F^{\delta_i}/\bar{q}\right)/\partial(\tau\dot{\eta}_j)$, F^{δ_i} is generalized aerodynamic force (hinge moment) on control mode *i*, $\dot{\eta}_j$ is rate of generalized coordinate representing elastic mode *j*, $\tau = \bar{c}/2V$, and $\bar{q}$ is dynamic pressure (eqs. (30))
$\mathbf{A}_2^{cf}$	$n_c \times n_f$ matrix where $\mathbf{A}_2^{cf}(i,j) = \partial\left(-F^{\delta_i}/\bar{q}\right)/\partial\left(\tau^2\ddot{\eta}_j\right)$, F^{δ_i} is generalized aerodynamic force (hinge moment) on control mode *i*, $\ddot{\eta}_j$ is acceleration of generalized coordinate representing elastic mode *j*, $\tau = \bar{c}/2V$, and $\bar{q}$ is dynamic pressure (eqs. (30))
$\mathbf{A}_{m+2}^{cf}$	$n_c \times n_f$ matrix where $\mathbf{A}_{m+2}^{cf}(i,j) = \partial\left(-\dot{x}^c_{a_{im}}\right)/\partial\dot{\eta}_j$, indicating effect of *j*th elastic mode rate on derivative of *m*th unsteady aerodynamic lag state associated with *i*th control mode, for $m = 1, 2, \ldots, n_{\text{lag}}$ (eqs. (30))
$\mathbf{A}_0^{cg}$	$n_c \times 1$ matrix where $\mathbf{A}_0^{cg}(i) = \partial\left(-F^{\delta_i}/\bar{q}\right)/\partial\xi_g$, F^{δ_i} is generalized aerodynamic force (hinge moment) on control mode *i*, ξ_g is displacement of generalized coordinate representing gust mode, and $\bar{q}$ is dynamic pressure (eqs. (30))
$\mathbf{A}_1^{cg}$	$n_c \times 1$ matrix where $\mathbf{A}_1^{cg}(i) = \partial\left(-F^{\delta_i}/\bar{q}\right)/\partial\left(\tau\dot{\xi}_g\right)$, F^{δ_i} is generalized aerodynamic force (hinge moment) on control mode *i*, $\dot{\xi}_g$ is rate of change of generalized coordinate representing gust mode, $\tau = \bar{c}/2V$, and $\bar{q}$ is dynamic pressure (eqs. (30))
$\mathbf{A}_{m+2}^{cg}$	$n_c \times 1$ matrix where $\mathbf{A}_{m+2}^{cg}(i) = \partial\left(-\dot{x}^c_{a_{im}}\right)/\partial\dot{\xi}_g$, indicating effect of gust mode rate on derivative of *m*th unsteady aerodynamic lag state associated with *i*th control mode, for $m = 1, 2, \ldots, n_{\text{lag}}$ (eqs. (30))

$\mathbf{A}_0^{fc}$	$n_f \times n_c$ matrix where $\mathbf{A}_0^{fc}(i, j) = \partial\left(-F^{\eta_i}/\bar{q}\right)/\partial\delta_j$, F^{η_i} is generalized aerodynamic force on elastic mode i, δ_j is displacement of generalized coordinate representing control mode *j*, and $\bar{q}$ is dynamic pressure (eqs. (29))
$\mathbf{A}_1^{fc}$	$n_f \times n_c$ matrix where $\mathbf{A}_1^{fc}(i, j) = \partial\left(-F^{\eta_i}/\bar{q}\right)/\partial\left(\tau\dot{\delta}_j\right)$, F^{η_i} is generalized aerodynamic force on elastic mode i, $\dot{\delta}_j$ is rate of generalized coordinate representing control mode *j*, $\tau = \bar{c}/2V$, and $\bar{q}$ is dynamic pressure (eqs. (29))
$\mathbf{A}_2^{fc}$	$n_f \times n_c$ matrix where $\mathbf{A}_2^{fc}(i, j) = \partial\left(-F^{\eta_i}/\bar{q}\right)/\partial\left(\tau^2\ddot{\delta}_j\right)$, F^{η_i} is generalized aerodynamic force on elastic mode i, $\ddot{\delta}_j$ is acceleration of generalized coordinate representing control mode *j*, $\tau = \bar{c}/2V$, and $\bar{q}$ is dynamic pressure (eqs. (29))
$\mathbf{A}_{m+2}^{fc}$	$n_f \times n_c$ matrix where $\mathbf{A}_{m+2}^{fc}(i, j) = \partial\left(-\dot{x}_{a_{im}}^{f}\right)/\partial\dot{\delta}_j$, indicating effect of *j*th control mode rate on derivative of *m*th unsteady aerodynamic lag state associated with *i*th control mode, for $m = 1, 2, \ldots, n_{\text{lag}}$ (eqs. (29))
$\mathbf{A}_0^{ff}$	$n_f \times n_f$ matrix where $\mathbf{A}_0^{ff}(i, j) = \partial\left(-F^{\eta_i}/\bar{q}\right)/\partial\eta_j$, F^{η_i} is generalized aerodynamic force on elastic mode i, η_j is displacement of generalized coordinate representing elastic mode *j*, and $\bar{q}$ is dynamic pressure (eqs. (29))
$\mathbf{A}_1^{ff}$	$n_f \times n_f$ matrix where $\mathbf{A}_1^{ff}(i, j) = \partial\left(-F^{\eta_i}/\bar{q}\right)/\partial\left(\tau\dot{\eta}_j\right)$, F^{η_i} is generalized aerodynamic force on elastic mode i, $\dot{\eta}_j$ is rate of generalized coordinate representing elastic mode *j*, $\tau = \bar{c}/2V$, and $\bar{q}$ is dynamic pressure (eqs. (29))
$\mathbf{A}_2^{ff}$	$n_f \times n_f$ matrix where $\mathbf{A}_2^{ff}(i, j) = \partial\left(-F^{\eta_i}/\bar{q}\right)/\partial\left(\tau^2\ddot{\eta}_j\right)$, F^{η_i} is generalized aerodynamic force on elastic mode i, $\ddot{\eta}_j$ is acceleration of generalized coordinate representing elastic mode *j*, $\tau = \bar{c}/2V$, and $\bar{q}$ is dynamic pressure (eqs. (29))
$\mathbf{A}_{m+2}^{ff}$	$n_f \times n_f$ matrix where $\mathbf{A}_{m+2}^{ff}(i, j) = \partial\left(-\dot{x}_{a_{im}}^{f}\right)/\partial\dot{\eta}_j$, indicating effect of *j*th elastic mode rate on derivative of *m*th unsteady aerodynamic lag state associated with *i*th elastic mode, for $m = 1, 2, \ldots, n_{\text{lag}}$ (eqs. (29))
$\mathbf{A}_0^{fg}$	$n_f \times 1$ matrix where $\mathbf{A}_0^{fg}(i) = \partial\left(-F^{\eta_i}/\bar{q}\right)/\partial\xi_g$, F^{η_i} is generalized aerodynamic force on elastic mode i, ξ_g is displacement of generalized coordinate representing gust mode, and $\bar{q}$ is dynamic pressure (eqs. (29))
$\mathbf{A}_1^{fg}$	$n_f \times 1$ matrix where $\mathbf{A}_1^{fg}(i) = \partial\left(-F^{\eta_i}/\bar{q}\right)/\partial\left(\tau\dot{\xi}_g\right)$, F^{η_i} is generalized aerodynamic force on elastic mode i, $\dot{\xi}_g$ is rate of change of generalized coordinate representing gust mode, $\tau = \bar{c}/2V$, and $\bar{q}$ is dynamic pressure (eqs. (29))
$\mathbf{A}_{m+2}^{fg}$	$n_f \times 1$ matrix where $\mathbf{A}_{m+2}^{fg}(i) = \partial\left(-\dot{x}_{a_{im}}^{f}\right)/\partial\dot{\xi}_g$, indicating effect of gust mode rate on derivative of *m*th unsteady aerodynamic lag state associated with *i*th elastic mode, for $m = 1, 2, \ldots, n_{\text{lag}}$ (eqs. (29))
a_δ	first-order pole of typical actuator transfer function, (eq. (18))
$\mathbf{B}$	generic linear system input matrix (eqs. (32) and (49))
$\mathbf{C}$	generic linear system output matrix (eq. (49))
C_l	rolling-moment coefficient (eq. (24))
$\bar{c}$	wing mean aerodynamic chord, reference length (eq. (27))
$\mathbf{D}$	generic linear system throughput matrix (eq. (49))
$\tilde{\mathbf{D}}$	matrix used in minimum state rational function approximation (eq. (28))
$\mathbf{E}$	error matrix defined in reduction methodology (eq. (60))

$\tilde{\mathbf{E}}$	matrix used in minimum state rational function approximation (eq. (28))
F_{HM}^{δ}	control surface hinge moment due to hydraulics (eq. (20))
$\mathbf{F}_{\mathrm{HM}}^{c}$	vector of control surface hinge moments due to hydraulics (eqs. (26))
F^{η_i}	total generalized aerodynamic force on elastic mode *i*
$\mathbf{F}_k$	general discrete system state transition matrix (eq. (34))
$\mathbf{G}$	damping matrix
$\mathbf{G}_k$	discrete system input transition matrix combined with $\mathbf{u}_k$ (eq. (34))
$\mathbf{G}_{k+1}$	discrete system input transition matrix combined with $\mathbf{u}_{k+1}$ (eq. (34))
$\mathbf{G}^{ff}$	diagonal modal damping matrix, $\mathbf{G}^{ff}(i, i) = 0.03$ (eqs. (29))
g	gravitational constant, 32.159 ft/sec^2
g_k	discrete system input transition scalar combined with $\mathbf{u}_k$ (eq. (46))
g_{k+1}	discrete system input transition scalar combined with $\mathbf{u}_{k+1}$ (eq. (46))
$H(\omega)$	general transfer function, function of frequency (eq. (7))
$\tilde{H}(s)$	transfer function relating output of Dryden spectra to random input (eq. (13))
h	simulation time period used for integration (eq. (33))
j	$=\sqrt{-1}$ (eq. (26))
$\mathbf{K}$	stiffness matrix
$\mathbf{K}^{ff}$	elastic mode stiffness matrix, diagonal for orthogonal elastic modes, $\mathbf{K}^{ff}(i, i) = m_i\omega_i^2$, where m_i is generalized mass of mode *i* and ω_i is frequency of mode *i* (eq. (26))
k	generic gain or factor (eq. (25))
k_{δ}	actuator steady-state gain (eq. (18))
L	scale length for turbulence (eq. (1))
$\mathbf{M}$	modal mass matrix (eq. (26))
$\mathbf{M}^{cc}$	modal mass matrix partition involving control modes only (eq. (26))
$\mathbf{M}^{cf}$	inertial coupling mass matrix between control modes and elastic modes, transpose of $\mathbf{M}^{fc}$ (eq. (26))
$\mathbf{M}^{fc}$	inertial coupling mass matrix between control modes and elastic modes, transpose of $\mathbf{M}^{cf}$ (eq. (26))
$\mathbf{M}^{ff}$	modal mass matrix involving elastic modes only (flex-flex), diagonal due to orthogonality of elastic modes (eq. (26))
N	number of states
n_c	number of control modes used in simulation equations
n_f	number of elastic modes used in simulation equations
n_{lag}	number of unsteady aerodynamic lag states (eqs. (27)–(30))
n_s	number of states in stable partition of equation (49) (eq. (56))
n_{sr}	number of states in reduced stable partition of equation (49) (eq. (56))
$\mathbf{Q}(\omega)$	matrix of generalized aerodynamic forces as function of frequency (eq. (26))
$\hat{\mathbf{Q}}(s)$	Laplace transform of estimate for $\mathbf{Q}(\omega)$ (eq. (27))
$\bar{q}$	dynamic pressure (eq. (26))
$\mathbf{R}$	matrix used in minimum state rational function approximation (eq. (28))
rl	rate limit (eq. (20))

S_υ	two-sided power spectral density of random input of turbulence (eq. (7))
$S_w(\omega)$	two-sided power spectral density of vertical component of turbulence (eq. (6))
s	Laplace variable (eq. (13))
$\mathbf{T}$	transformation matrix used in model reduction methodology (eq. (55))
$\mathbf{T}_1$	$n_s \times n_{sr}$ partition of **T** (eq. (56))
$\mathbf{T}_2$	$n_s \times (n_s - n_{sr})$ partition of **T** (eq. (56))
T_{cf}	time period required by computer to advance simulation time period h
T_υ	sampling period applied to the white-noise process υ (eq. (9))
t	time
$\mathbf{U}_1$	$n_s \times n_{sr}$ partition of matrix $\mathbf{T}^{-1}$ (eq. (56))
$\mathbf{U}_2$	$n_s \times (n_s - n_{sr})$ partition of matrix $\mathbf{T}^{-1}$ (eq. (56))
$\mathbf{U}_x$	unitary matrix, part of singular-value decomposition of controllability Gramian **X** (eq. (52))
$\mathbf{U}_w$	unitary matrix, part of singular-value decomposition of $\mathbf{U}_x\boldsymbol{\Sigma}_x^{1/2}\mathbf{U}_x^T\mathbf{Y}\mathbf{U}_x\boldsymbol{\Sigma}_x^{1/2}\mathbf{U}_x^T$ (eq. (54))
$\mathbf{u}$	input vector (eqs. (32) and (49))
$\mathbf{u}_k$	vector input at time $t = kh$ (eq. (33))
$u(s)$	Laplace variable of generic scalar input signal (eq. (31))
V	airspeed; free-stream velocity (eq. (27) and definition of τ)
$\mathbf{V}_x$	unitary matrix, part of singular-value decomposition of controllability Gramian **X** (eq. (52))
$\mathbf{X}$	controllability Gramian (eq. (51))
x	generic state; intermediate variable (eqs. (A3)–(A5))
$\mathbf{x}$	state vector (eqs. (32) and (49))
$\mathbf{x}_k$	state vector at time $t = kh$ (eq. (34))
x_δ	intermediate state used in mechanization of actuator dynamics (eq. (19))
$\mathbf{x}_{a_m}^f$	vector of unsteady aerodynamic lag states associated with elastic (flex) modes, $m = 1, 2, \ldots, 4$ (eqs. (29))
$\mathbf{x}_{a_m}^c$	vector of unsteady aerodynamic lag states associated with control modes, $m = 1, 2, \ldots, 4$ (eqs. (30))
$\mathbf{Y}$	observability Gramian (eq. (51))
$\mathbf{y}$	output vector (eq. (49))
$y(s)$	Laplace variable of generic scalar input signal (eq. (31))
β_m	nondimensional reduced frequency of *m*th unsteady aerodynamic lag state, $\beta = \omega\bar{c}/2V$ (eq. (27))
$\vec{\delta}$	vector of generalized coordinates consisting of control modes (eq. (26))
δ	generic individual control surface deflection as function of time (eq. (26))
$\delta(s)$	Laplace transform of a generic individual control surface deflection (eq. (18))
$\delta_c(s)$	Laplace transform of an individual control surface deflection command (eq. (18))
$\dfrac{\delta(s)}{\delta_c(s)}$	typical transfer function relating control surface position to control surface command
ε_B	error bound used in reduction methods (eq. (61))
ζ_δ	damping of second-order denominator term of typical actuator transfer function (eq. (18))

$\vec{\eta}$	vector of generalized coordinates consisting of elastic modes (eq. (26))
η_i	displacement of generalized coordinate, elastic mode *i*
η_j	displacement of generalized coordinate, elastic mode *j*
ξ_g	gust-mode participation coefficient, output of Dryden turbulence transfer function (eqs. (13) and (26))
ρ	fluid density used in definition of $\bar{q} = \frac{1}{2}\rho V^2$ (eq. (26))
Σ_w	diagonal matrix in singular-value decomposition of $\mathbf{U}_x\Sigma_x^{1/2}\mathbf{U}_x^T\mathbf{Y}\mathbf{U}_x\Sigma_x^{1/2}\mathbf{U}_x^T$ (eq. (54))
Σ_x	diagonal matrix in singular-value decomposition of controllability Gramian **X** (eq. (52))
$\Sigma_x^{1/2}$	diagonal matrix where $\Sigma_x^{1/2}(i, j) = \sqrt{\Sigma_x(i, i)}$ (eq. (54))
σ	root-mean-square (rms) of random process, $\sigma = \sqrt{E\{x^2\}}$, where E is expected value operator; also calculated by integration of power spectral density (eq. (2)), singular value (eq. (61))
$\bar{\sigma}$	maximum singular value (eq. (61))
σ_g	rms gust velocity (eq. (1)) often referred to as turbulence intensity (see MIL-STD-1797A, p. 17)
σ_h	Hankel singular value (eq. (61))
σ_υ	rms of random process υ (eq. (8))
τ	time constant, $\tau = \bar{c}/2V$, where $\bar{c}$ is the wing mean aerodynamic chord reference length, used in unsteady aerodynamic approximations (eq. (27)); generic time constant (eq. (40))
τ_g	time constant, $\tau_g = L/V$ where L is a reference scale length used in turbulence equations (eq. (5))
υ	digitally generated Gaussian random input to turbulence spectral form, function of time (eq. (7))
Φ	one-sided Dryden power spectral density (psd)
$\Phi(\Omega)$	one-sided Dryden psd as function of spatial frequency Ω (eq. (1))
$\Phi_u(\Omega)$	one-sided Dryden longitudinal psd as function of spatial frequency Ω (eq. (A2))
$\hat{\Phi}_u(L\Omega)$	one-sided Dryden longitudinal psd as function of $L\Omega$ (eq. (A4))
$\Phi_v(\Omega)$	one-sided Dryden side (and lateral) psd
$\Phi_w(\Omega)$	one-sided Dryden vertical (and lateral) psd as function of spatial frequency Ω (eq. (A1))
$\tilde{\Phi}_w(\omega)$	one-sided Dryden vertical (and lateral) psd as function of ω (eq. (4))
$\hat{\Phi}_w(L\Omega)$	one-sided Dryden vertical (and lateral) psd as function of $L\Omega$ (eq. (A7))
Ω	spatial frequency of frozen turbulence field, rad/ft (eq. (1))
ω	frequency, rad/sec (eq. (3))
ω_δ	frequency of second-order denominator term of typical actuator transfer function, rad/sec (eq. (18))
ω_{aa}	break frequency of antialiasing transfer function (eq. (31))
[ ]	matrix
{ }	column vector

Subscripts:

a	aerodynamic
aa	antialiasing
as	antisymmetric
c	commanded

e	equivalent
g	quantity associated with turbulence
HM	hinge moment
lag	aerodynamic lag quantity
lin	linear
neg	negative
nl	no load
pos	positive
r	reduced model matrix (eq. (59))
s	stable (eq. (50))
sr	reduced model stable matrix, (eq. (58))
STALL	actuator dynamic stall
sy	symmetric
v	lateral (side) component of turbulence
w	vertical component of turbulence
u	unstable (eq. (50)); longitudinal component of turbulence (eq. (A2))
δ	associated with actuator or control surface
υ	associated with Gaussian random process (eq. (7))
0	aerodynamic RFA matrix associated with position (eqs. (27)–(30))
1	aerodynamic RFA matrix associated with rate (eqs. (27)–(30))
2	aerodynamic RFA matrix associated with acceleration (eqs. (27)–(30))

Superscripts:

c	associated with control mode equations
cc	effect on hinge moment due to control
cf	effect on hinge moment due to flex (control-flex)
cg	effect on hinge moment due to gust input
f	associated with elastic (flex) mode equations
fc	effect on elastic due to control (flex-control)
ff	effect on elastic due to elastic (flex-flex)
fg	effect on elastic due to gust input (flex-gust)
trap	associated with trapezoidal integration
zero	associated with zero-order hold integration
*	complex conjugate transpose
δ_i	associated with generalized coordinate, control mode *i*
η_i	associated with generalized coordinate, elastic mode *i*

Notations:

$(\bar{\ })$	bar over symbol denotes mean value
$(\dot{\ })$	dot over symbol denotes first derivative with respect to time
$(\ddot{\ })$	two dots over symbol denote second derivative with respect to time

Abbreviations:

AFW	active flexible wing
CCFR	control computer frame rate
CFD	computational fluid dynamics
DOF	degree of freedom (fig. 5)
EU	engineering unit
ISAC	interaction of structures, aerodynamics, and controls
LaRC	Langley Research Center
LEI	leading edge inboard
LEO	leading edge outboard
LLEI	left leading edge inboard
LLEO	left leading edge outboard
LQG	linear quadratic Gaussian
LTEI	left trailing edge inboard
LTEO	left trailing edge outboard
psd	power spectral density
RFA	rational function approximation
RLEI	right leading edge inboard
RLEO	right leading edge outboard
RTEI	right trailing edge inboard
RTEO	right trailing edge outboard
RVDT	rotary variable differential transducer
rms	root mean square
SIC	structural influence coefficient
TDT	Transonic Dynamics Tunnel
TEI	trailing edge inboard
TEO	trailing edge outboard
TOGW	takeoff gross weight

Abstract

Mathematical models and implementation issues are described for simulations developed in the active flexible wing wind tunnel test program, which resulted in successful application of active flutter control. The wind tunnel test program required a truth batch simulation for off-line tests of proposed control designs and functional, hot-bench tests of digital controller hardware and software. To provide the hot-bench test environment, a real-time simulation of the wind tunnel model and test environment was desired. Although mathematical model complexity and computing power limitations prevented attainment of real-time operation, essential test goals were met with a hot-bench simulation running at a timescale ratio no slower than 1:5. To achieve the required timescale, model reduction methods were applied to the aeroservoelastic portion of the full-order mathematical model. The reduction method was based on the internally balanced realization of a linear dynamic system. The error-bound properties of the internally balanced realization contributed to the method utility in the model reduction process. The state dimensions of the aeroservoelastic model were reduced by a factor of 2. The errors due to reduction appeared beyond the 10th bit of the analog-to-digital converters for all 560 combinations of simulation inputs and outputs.

Introduction

Importance of Flutter in Airplane Design

Weight minimization is vital to successful airplane design. However, if structural weight is minimized, airplanes will deform appreciably under load. An interacting feedback process results wherein deformation changes the distribution of the aerodynamic load, which in turn changes the deformation. At certain dynamic pressures and Mach numbers, this process may lead to flutter, a self-excited and often destructive oscillation wherein energy is absorbed from the fluid stream. (See Garrick and Reed (1981).)

An airplane must be flutter-free beyond the operating envelope. For military airplanes (MIL-A-8870B (AS)), a flutter-free margin is required that is equal to a 15-percent increase in equivalent airspeed beyond the design limit speed envelope (fig. 1) at both constant altitude and constant Mach number. For commercial airplanes (FAR Part 25, Section 25.629 (1992)) the flutter-free margin is a 15-percent increase in equivalent airspeed beyond the speed envelope. Prior to 1992, the required commercial airplane margin had been 20 percent. Traditional passive remedies for flutter problems add weight in the form of additional structure or mass ballast. If the flutter-free requirement for airplane design can be met by active suppression with the use of existing control surfaces (at least in the margin beyond the operational envelope), weight savings may be possible. Preliminary design studies of a supersonic transport concept estimate that an airplane weight reduction of 2 to 4 percent of the total structural weight is possible with the use of active flutter suppression instead of passive remedies. (See Thompson and Kass (1972).)

Technology studies at the Douglas Aircraft Company (1975, vol. 1, pp. 1–78) on a Mach-2.2 supersonic transport concept indicate that provision for passive flutter clearance without placard restrictions to the flight envelop and also within aeroelastic constraints involving static wing twist results in an incremental structural weight penalty of 8802 lb. If placard envelop restrictions were allowed for certain fuel conditions, the weight penalty dropped to 2702 lb. In addition, the total fuel capacity was reduced by 5 to 10 percent because passive flutter remedies required that no fuel be stored in the outboard wing. These weight penalties were calculated for a design with a takeoff gross weight (TOGW) of 707 600 lb and an operating empty weight of 297 182 lb. Because of the large fuel fraction characteristic of supersonic transports, small changes in operational empty weight produce large changes in TOGW; the TOGW and cost are roughly proportional.

Recent studies performed at the Boeing Commercial Aircraft Company by Ray, Carlin, and Lambregts (1992) of high-speed commercial transports state that “substantial saving in structural weight may be achieved by relying on an active flutter suppression system . . . , particularly if metal structures are used.” Studies at Rockwell International Corporation on an advanced fighter concept suggest that, when coupled with an active flexible wing (AFW) concept for an advanced fighter, active flutter suppression may allow TOGW to be reduced by 2 to 5 percent. (See Miller (1988).)

Active Flexible Wing Program and Role of Simulation

Wind tunnel tests of active flutter suppression control systems were conducted in the Langley Transonic Dynamics Tunnel (TDT). The test model (fig. 2) was a full-span, free-to-roll, aeroservoelastically scaled model of an advanced fighter and is referred to herein as the AFW wind tunnel model. This model has been used in two research programs involving four TDT tests. Rockwell International Corporation, USAF, and NASA collaborated to perform wind tunnel tests in 1986 and 1987, which constituted the first AFW research program described by Miller (1988). The test in 1986 produced basic force- and moment-coefficient data and control surface effectiveness data. In the 1987 test, static pressure data were taken, active roll control was demonstrated, and preliminary structural mode control and maneuver load alleviation functions were tested.

The second AFW research program was a joint effort of NASA and Rockwell International Corporation and is described by Noll et al. (1989); Perry et al. (1990); Perry, Cole, and Miller (1992); and Taylor (1991). The second AFW research program, which resulted in wind tunnel tests in 1989 and 1991, is discussed herein. The primary objectives of the 1989 test were to evaluate flutter suppression and rolling maneuver load control systems as individual functions. The primary objective of the 1991 test was to demonstrate active flutter suppression during simultaneous performance of aggressive rolling maneuvers in which wing loads were controlled.

The flutter mechanism of the AFW model was a classical clean-wing flutter. In clean-wing flutter, a wing bending elastic mode couples with a wing torsion elastic mode to produce two new modes, one of which has eigenvalues that move rapidly into the unstable region of the complex plane as dynamic pressure increases. Early in the program, researchers recognized that failure of the active flutter suppression system during open-loop flutter test conditions would put both the model and the wind tunnel at risk. Therefore, extensive simulation-based, end-to-end tests and validation of the controller hardware and software systems were performed. Simulations to support the 1989 and 1991 wind tunnel tests are also discussed by Buttrill and Houck (1990), Buttrill and Bacon (1991), and Buttrill et al. (1992). In this report, simulations and mathematical models are discussed and identified by the year (either 1989 or 1991) of the wind tunnel test that they were intended to support.

Both batch and hot-bench simulations were developed for each wind tunnel test. The batch simulations served as truth models and were used to evaluate the control laws by predicting performance and establishing stability margins, provide data files for the hot-bench simulations, and verify the hot-bench simulations. The batch simulations of 1989 and 1991 incorporated both symmetric and antisymmetric elastic modes,[1] rate-limiting actuator models, wind tunnel turbulence representation, and the digital controller model with attendant computational time delays and sampling effects. The hot-bench simulations (1989 and 1991) of the AFW model in the wind tunnel environment supported digital controller hardware and software tests. The digital controller was a complex system that consisted of a Sun workstation augmented with three special-purpose processor boards. (See Hoadley (1992); Pototzky et al. (1990); and Wieseman, Hoadley, and McGraw (1992).) In addition to implementing both the roll and flutter control laws at 200 Hz, the digital controller generated excitation signals and collected data to support on-line assessment of both open- and closed-loop plant stabilities. The stability assessments were performed on another companion computer.

A key strategy, which was adopted early in the AFW test program, was to recognize that hot-bench tests could be performed with a slower timescale than real time. This decision permitted use of the existing LaRC central real-time facility. The mathematical models were sufficiently complex so that real-time computer simulation at the LaRC central facility was impossible. Because the controller was digital, tests at a different timescale were straightforward. Special accommodations were required for nondigital dynamic elements in the test loop, which were limited to the analog antialiasing and notch filters. Although the requirement that the digital controller complete its calculations in 5 msec (200 Hz) could not be tested at a slow timescale, virtually all other required controller functions could be evaluated. Completion of the calculations in 5 msec was verified without the hot-bench simulation in the loop. Experience before the 1989 test had shown that hot-bench tests conducted at timescales slower than 1:5, while theoretically permissible, became operationally burdensome, particularly when the system was being debugged.

The state dimension of the simulation mathematical model developed for the 1991 wind tunnel test became too large for an effective hot-bench simulation based on the same procedures used for the smaller 1989 mathematical model. This growth in state dimension is discussed in more detail in the section “Simulation Structure and Implementation.”

To achieve an acceptable timescale, the simulation state dimension had to be reduced substantially without compromising the response accuracy. The model reduction method applied to the 1991 mathematical model was based on the well-known properties of the internally balanced realization of a linear time-invariant system. (See Moore (1981), Glover (1984), and Enns (1985).) When an asymptotically stable system is transformed into internally balanced coordinates, the resulting states are ordered according to their importance to system input and output behavior. The nature of this ordering is made more precise in the section “Error Properties.” The internally balanced method was extended by Enns (1985), who developed an approach whereby frequency regions could be selected for emphasis by the use of weighting filters, which has come to be known as the frequency-weighted internally balanced reduction method. Bacon (1991) extended the frequency-weighted internally balanced approach and produced a frequency-weighted pole-preserving method to better accommodate a system with unstable or neutrally stable components.

---

[1] Let $\phi(x, y, z)$ describe an elastic mode displacement field as a function of the undeformed coordinates $x, y,$ and z. An elastic mode is called symmetric (about the X-Z plane) if $\phi(x, y, z) = \phi(x, -y, z)$ and antisymmetric if $\phi(x, y, z) = -\phi(x, -y, z)$.

For the work described herein, the classical internally balanced method of handling unstable subsystems by decoupling the stable and unstable portions was applied without frequency weighting. When the classical internally balanced method was combined with appropriate scaling and a conservative choice for an error bound, a relatively hands-off reduction method emerged. The successful application of an internally balanced approach to the large and complex systems that support control law design for aeroservoelastic systems is significant; the method offers an additional approach to the research of Tiffany and Adams (1988) and Tiffany and Karpel (1989), in minimizing the impact of unsteady aerodynamic states on the size of aeroservoelastic systems.

Simulation Objectives and Results Organization

The principal goal of this report is to document the modeling and simulation methods of the AFW program. An important part is an assessment of the many engineering judgment decisions that were required. In addition, this paper is a detailed guide for definition and implemention of time domain simulations of realistic aeroservoelastic models consistent with full-envelope flight simulations. The literature is scant with regard to time domain simulations of realistic aeroservoelastic models. Some exceptions are Cutchins, Purvis, and Bunton (1983); Waszak, Davidson, and Schmidt (1987); Waszak and Schmidt (1988); Buttrill, Arbuckle, and Zeiler (1987); Morino and Baillieul (1987); and Arbuckle, Buttrill, and Zeiler (1989). A more typical case is the recent and excellent text of Stevens and Lewis (1992) on airplane dynamics, simulation, and control; however, they mention the subject of elastic dynamics only in passing.

In this report the wind tunnel, the test model, and the hot-bench laboratory are described. Next, the rationale is given for using a variable timescale, and its utility in the hot-bench test environment is demonstrated. The mathematical models, as developed to implement the simulations, are presented and the differences in the mathematical models used to support the 1989 and 1991 tests are characterized. Comparisons between experimental and predicted responses are made. Next, the simulation structure and implementation issues are addressed. The implementation issues of the hot-bench simulation are described in detail; the batch simulation implementation, being simpler, is only briefly mentioned. Then, the theory behind and methodology for the model reduction are presented, along with comparisons of full- and reduced-order models that demonstrate model reduction technique effectiveness for the AFW program. The “Concluding Remarks” section summarizes the key points and lessons learned.

Wind Tunnel Model

Figure 2 shows the AFW wind tunnel model mounted in the Langley TDT. The AFW sting mount had an internal ball-bearing arrangement that allowed the model to roll approximately ±145° about the sting axis. A hydraulically powered pivot connected the fuselage to the sting so that the model pitch could be remotely adjusted from approximately –1.5° to 13.5°. (See Perry, Cole, and Miller (1992).)

The TDT is a closed-circuit, continuous flow wind tunnel capable of testing at stagnation pressures ranging from 0 to atmospheric and at Mach numbers ranging from 0 to 1.2. (See Perry, Cole, and Miller (1992).) Dynamic pressure and Mach number can be varied independently; that is, fan speed can be used to control the free-stream Mach number and the wind tunnel can be evacuated to achieve a desired dynamic pressure. (See Adams et al. (1992).) Figure 3 shows the operationing envelope of the TDT with air as the test medium. For all AFW tests in the second AFW research program, air was the test medium.

For the flutter suppression investigations, destabilizing mass ballast was added to each wingtip so that the model would flutter within the TDT operating envelope. The wingtip ballast lowered the wing first-torsion elastic mode *in vacuo* frequency and to a lesser extent the *in vacuo* frequency of the wing first-bending mode. The result was that *in vacuo* frequencies of the wing first-bending and first-torsion elastic modes were closer and, as dynamic pressure was increased, these elastic modes combined to form the primary flutter mechanism at a lower dynamic pressure than that for the original wind tunnel model with no wingtip ballast.

The wingtip ballast (fig. 4) could also be rapidly decoupled in pitch from the wingtip by the release of a hydraulic brake. Ideally, when decoupled, the wingtip ballast would be sufficiently free to rotate about the pivot mechanism so that, as the wing twists, the wingtip ballast would remain level. In practice, the wingtip ballast was restrained in pitch by a soft spring (fig. 4), which was stiff enough to prevent the wingtip ballast from departing in pitch from static aerodynamic load yet soft enough to maintain the decoupled boundary well beyond the wind tunnel operating envelope. Decoupling the wingtip ballast proved effective in suppressing flutter during the tests and also provided an additional safety margin for the wind tunnel model and the TDT. When the hydraulic brake in the wingtip ballast was engaged, the wingtip ballast with its attendant high inertia was coupled with the wing torsion modes to lower the *in vacuo* frequencies. Additional information on the wingtip ballast design can be obtained from Perry et al. (1990) and Perry, Cole, and Miller (1992).

As indicated in figure 5, the AFW wind tunnel model had eight control surfaces that could be commanded. Each wing had four pairs of control surfaces consisting of the following right and left symmetric members: the leading edge outboard (LEO), the leading edge inboard (LEI), the trailing edge outboard (TEO), and the trailing edge inboard (TEI). The model instrumentation included the following 40 sensor outputs: 8 control surface position measurements, 13 accelerometer outputs, 8 strain gage outputs, 8 hinge moment measurements, 1 model pitch position, 1 model roll position, and 1 model roll rate. Two wing accelerometers, previously collocated with the LEI control surfaces, were moved to the wingtip ballast devices. The AFW wind tunnel model without the wingtip ballast devices is described in detail by Miller (1988). The input-output signals for the wind tunnel model and for the supporting simulations are listed in table I.

Hot-Bench Overview

Hot-Bench Laboratory

The hot-bench laboratory provided a test environment as close as possible to that of the control computer hardware system in the TDT. The analog communication links were the same for the digital controller when connected to the hot-bench laboratory components as when connected to the model at the wind tunnel. Ideally, the hot-bench test environment would permit tests of the full functionality of the digital controller. The digital controller functions included model control, input excitation, general data acquisition, and data acquisition for subsequent stability analysis on a separate computer. (See Wieseman, Hoadley, and McGraw (1992).) To support full-functionality testing, all 40 of the wind tunnel model data outputs had to be simulated at the hot-bench laboratory.

The AFW hot-bench simulation setup, depicted schematically in figure 6, was linked to the central real-time facility at LaRC. As described by Crawford and Cleveland (1986), the LaRC real-time facility contains nodes that communicate through a fiber-optic digital network. For the AFW hot-bench simulation, a Cyber 175 system (the real-time simulation computer then available) was used to integrate the equations of motion. A graphics computer provided a real-time display that approximately simulated the view through the wind tunnel test-section windows.

During the hot-bench simulation and wind tunnel tests, the interface electronics processed signals to and from the digital controller. (See fig. 6.) The interface contained logic that tested the signals to ensure that conservative safety limits were not exceeded. If a violation occurred, the controller would be taken off-line and a trip signal would be sent to the wind tunnel control electronics. In addition, the interface electronics included analog filters that conditioned the signals from the wind tunnel model before the digital controller sampled them. The analog filters were specified by the control law designers and consisted of antialiasing and notch filters. Both 25- and 100-Hz antialiasing filters were available, as were various notch filters.

The hot-bench real-time display is shown in figure 7. The display presents model roll, control surface deflections, and total structural deformation of the simulated wind tunnel model. The display also depicts the model in a roll attitude with the left wing down and with the left and right trailing-edge inboard (LTEI and RTEI) surfaces deflected antisymmetrically (−10.003° LTEI and 10.003° RTEI) to produce the roll. The dynamic pressure Q is shown as 350 psf, the magnification factor (MAG) is 2 (used to exaggerate the elastic deflections for display purposes), the control computer frame rate (CCFR) is 20, and the simulation case (IMCASE) is 6. This simulation case includes 20 elastic degrees of freedom (DOF) appropriate to the free-to-roll (i.e., roll-brake-off) boundary condition. All other control surfaces are at a commanded deflection of zero so that any apparent deflection (apart from LTEI and RTEI) is due to elastic deflection of the simulated model wing structure.

Hot-Bench Timescale

Several factors prevented the AFW hot-bench simulation from operating in real time. The control computer runs at 200 Hz in the wind tunnel. To prevent excessive digitally induced time delays, engineering judgment was used to determine that the hot-bench simulation needed to be updated twice for each digital controller frame, requiring an update rate of 400 Hz if the hot-bench simulation was to run in real time. That simulation update rate would require solution of the aeroservoelastic simulation equations in 2.5 msec on the Cyber 175 system. For a full-order model with 20 elastic modes, the required computational frame time exceeded 25 msec. Even had the Cyber 175 central processing unit been able to complete the equations-of-motion calculations in 2.5 msec (400 Hz), the minimum frame time available on the Cyber 175 system because of the real-time operating system architecture was 5 msec (200 Hz).

An additional constraint on real-time computing resources existed. During the hot-bench phase, many other research programs competed for the two production real-time computers at the LaRC central facility. Consequently, the hot-bench simulation often shared a Cyber 175 system with another job, which left only half of the Cyber system computing power available. Thus, the timescale had to be an easily adjusted parameter for any dynamic component in the hot-bench loop.

The AFW hot-bench simulation (fig. 6) operated more slowly than real time (1:1). Timescale is a function of the integration step h and the computing frame time (T_{cf}) of the simulation. If T_{cf} is larger than h, the simulation runs at a timescale of 1:(T_{cf}/h), which is slower than real time. During the tests in the hot-bench laboratory, the analog filters in the model-controller interface electronics were bypassed (see switch in fig. 6) because a timescale could not be applied to the analog filter dynamics. However, the analog filter dynamics were part of the dynamic system that the digital controller would see in the wind tunnel tests and needed to be accounted for in the hot-bench simulations.

For the 1991 AFW test, five separate control laws were validated with hot-bench simulation: three were flutter suppression controllers (Christhilf and Adams (1992), Mukhopadhyay (1992), and Waszak and Srinathkumar (1992)), and two were roll controllers combined with load alleviation (Moore (1992) and Woods-Vedeler and Pototzky (1992)). A fourth flutter control law (Klepl (1992)) was designed and had some wind tunnel test time in 1991 but had no validation by hot-bench simulation.

All the control laws used the 25-Hz analog antialiasing filters. At least one flutter controller used additional analog notch filters to further condition inputs to the digital controller. Because the choice of analog notch filters was generally unique to the control law (as opposed to the antialiasing filters), the burden of digitally simulating the notch filters fell to the control law designers. In the hot-bench simulations, the control law dynamics were augmented with the required notch filters. The controller was operating on a slow timescale so the additional computational burden was not a problem, as would have been the case during real-time runs. The antialiasing filter dynamics, however, were included in the mathematical model discretization represented by the box labeled "Simulation computer" in figure 6. Because all controllers used the same antialiasing filter set, the antialiasing dynamics were conveniently accounted for in the plant dynamics.

Digital simulation of the analog filters ensured that all dynamic elements in the hot-bench loop could be represented at selectable timescales. Therefore, the dynamic elements of the hot-bench loop and the control and simulation computers were run synchronously at a slow timescale, and dynamic validity was maintained.

When the 25-Hz antialiasing filters were bypassed, none remained in the hot-bench loop. Antialiasing filters are normally required for digital control of hardware or analog systems. However, in the hot-bench simulations, the hardware is also digitally simulated. The hot-bench environment is relatively free of electronic and measurement noise when compared with that of the wind tunnel. The LaRC real-time simulator sites are tested to determine whether any analog signals contain excessive noise; the noisy signals are filtered as necessary with low-pass Bessel filters, which may have cutoff frequencies of 10, 20, 80, or 100 Hz as required. The hot-bench hardware used an existing tested simulator site, and the absence of antialiasing filters in the hot-bench setup did not cause problems. Real-time simulations supported at the LaRC facility are typically run without antialiasing filters unless problems are noted.

Mathematical Models

Figure 8 shows the structure of the batch and hot-bench simulations and the data flow between them. Depicted are 10 inputs and 56 outputs for the simulation mathematical model. The inputs consist of eight actuator commands and two Gaussian random numbers (1991 simulation) used to drive the turbulence models. Of the 56 outputs, the first 40 represent the first 40 simulated wind tunnel model sensor outputs listed in table I. The last 16 outputs are the displacements of the generalized coordinates associated with 16 elastic modes; the 8 lowest frequency symmetric and asymmetric elastic modes are used to drive the real-time graphics display. (See fig. 7.) When the simulated model was in the free-to-roll condition, the first antisymmetric elastic mode was actually the roll degree of freedom.

This section is organized as follows: The turbulence models used in both the 1989 and 1991 simulation models are described and evaluated. The principal source of disturbances that the flutter suppression laws must reject is wind tunnel turbulence, and adequate characterization of that turbulence for an assessment of actuator activity is critical to control law design. The model of the plant to be controlled is then described. The plant model contains the following subsystem models: actuator dynamics, structural dynamics, aerodynamics, and antialiasing filter dynamics, all of which are described in successive sections. The subsystem models are then integrated in the next section which describes the aeroservoelastic equations. Finally, an assessment of the validity of these models is made in the section entitled “Flutter Predictions and Frequency Response.”

The level of complexity of these mathematical models were typical of industry and government practice. The establishment of an integrated batch and real-time aeroservoelastic simulation methodology represented one of the technical contributions of the AFW program because the synthesis of the various component models in a nonlinear simulation framework is not widespread.

Turbulence Model

Wind tunnel turbulence is the principal component of disturbances seen by the controller-model system. Characterization of the wind tunnel turbulence can significantly affect estimates of control surface activity. This section first describes the structure of the turbulence models and then the model parameters.

Implementation of modified Dryden model. The turbulence model used in the AFW simulation was a modified form of the Dryden atmospheric turbulence model. (See Hoblit (1988).) The Dryden spectral form for the vertical and lateral component of turbulence is given by

$$\Phi(\Omega) = \frac{\sigma_g^2 L}{\pi} \frac{(1 + 3L^2\Omega^2)}{(1 + L^2\Omega^2)^2} \tag{1}$$

where L is scale length, Ω is the spatial frequency (rad/ft) of the frozen turbulence field, and σ_g is the rms magnitude of the gust velocity. The symbol Φ is replaced by Φ_w in equation (1) for a vertical gust and by Φ_v for a side or lateral gust. The rms magnitude σ_g is often referred to and specified as a gust intensity with units of velocity in the literature. (See MIL-STD-1797A.) This expression can be found in several references, including Hoblit (1988) and Roskam (1979). Equation (1) defines a one-sided power spectral density Φ. When the power spectral density (psd) is integrated over the complete frequency range (in this case, from 0 to infinity), the total power in the signal should be recovered. For a random signal, total power is given by the expected value of the square of the signal (i.e., the square of the rms). In the Dryden psd, σ_g is the rms. Therefore, as given by Hoblit ((1988), p. 34),

$$\sigma_g^2 = \int_0^\infty \Phi(\Omega)\, d\Omega \tag{2}$$

A proof of equation (2) is given in appendix A.

When the argument of the spectrum function Φ is changed, the relationship of equation (2) must be preserved. To convert the spectrum function from the spatial frequency Ω to a function of ω (rad/sec), we define a change of variables by

$$\left.\begin{aligned} \Omega &= \left(V^{-1}\right)\omega \\ d\Omega &= \left(V^{-1}\right) d\omega \end{aligned}\right\} \tag{3}$$

where V is the free-stream velocity. Equations (2) and (3) are combined to give

$$\int_0^\infty \Phi(\Omega)\, d\Omega = \int_0^\infty \Phi(\omega/V)\left(V^{-1}\right) d\omega$$

which gives the following definition for $\tilde{\Omega}(\omega)$, which is the Dryden psd function in terms of ω:

$$\int_0^\infty \tilde{\Phi}(\omega)\, d\omega = \frac{1}{V}\int_0^\infty \Phi(\omega/V)\, d\omega = \int_0^\infty \Phi(\Omega)\, d\Omega = \sigma_g^2 \tag{4}$$

Equations (1) and (4) can be combined to produce

$$\tilde{\Phi}(\omega) = \frac{\sigma_g^2 \tau_g}{\pi} \frac{\left[1 + 3(\tau_g\omega)^2\right]}{\left[1 + (\tau_g\omega)^2\right]^2} \tag{5}$$

where $\tau_g = L/V$. Whereas equations (1) and (5) (or versions thereof) can be found in several sources (Roskam (1979), Hoblit (1988), and MIL-STD-1797A), the digital implementation of equation (5) may not be obvious and requires elaboration. The exact implementation equations and theoretical justifications are discussed next.

The theoretical derivations that follow rely heavily on Hardin (1986) whose convention was to deal with two-sided spectra. Define the two-sided psd S_w as follows:

$$S_w(\omega) = \frac{1}{2}\tilde{\Omega}(\omega) = \frac{\sigma_g^2 \tau_g}{2\pi} \frac{\left[1 + 3(\tau_g\omega)^2\right]}{\left[1 + (\tau_g\omega)^2\right]^2} \tag{6}$$

To support the digital implementation of a Dryden turbulence model, a transfer function must be defined such that when implemented digitally and driven by a Gaussian digitally generated random number sequence, the transfer function will produce a signal with the two-sided psd defined in equation (6). The relationship between the psd of an output signal S_w, the psd of an input signal S_υ, and the linear transfer function H, which relates input to output, is given by (eq. (5.2) of Hardin (1986))

$$S_w(\omega) = H^*(\omega)H(\omega)S_\upsilon \tag{7}$$

where H^* is the complex conjugate of H and S_υ is the psd of a Gaussian random process having an rms $\sigma_\upsilon = 1$. Therefore,

$$\sigma_\upsilon^2 = 1 = \int_{-\infty}^{\infty} S_\upsilon(\omega)\,d\omega \tag{8}$$

If the random number generator that produces the input signal υ is a good simulation of a white-noise process and is sampled and held every T_υ sec, then υ can, for the following derivations, be assumed to have constant power over the Nyquist frequency interval defined by $(-\pi/T_\upsilon, \pi/T_\upsilon)$ where $2\pi/T_\upsilon$ is the sampling frequency (rad/sec). The input signal υ is further assumed to have zero power outside the Nyquist frequency interval. The reasons for these assumptions are addressed in appendix B. Equation (8) then becomes

$$1 = \int_{-\pi/T_\upsilon}^{\pi/T_\upsilon} S_\upsilon d\omega = S_\upsilon \frac{2\pi}{T_\upsilon} \tag{9}$$

where S_υ is a constant. The solution for S_υ gives

$$S_\upsilon = \frac{T_\upsilon}{2\pi} \tag{10}$$

Equations (6), (7), and (10) are combined to give

$$\frac{\sigma_g^2\tau_g}{2\pi}\frac{\left[1 + 3(\tau_g\omega)^2\right]}{\left[1 + (\tau_g\omega)^2\right]^2} = H^*(\omega)H(\omega)\frac{T_\upsilon}{2\pi} \tag{11}$$

For simulation implementation, a transfer function $\tilde{H}(s)$ is defined in the Laplace variable s such that, when s is replaced by $j\omega$, results in

$$\tilde{H}(-j\omega)\tilde{H}(j\omega) = H^*(\omega)H(\omega) = \frac{\sigma_g^2\tau}{T_\upsilon}\frac{\left[1 + 3(\tau_g\omega)^2\right]}{\left[1 + (\tau_g\omega)^2\right]^2} \tag{12}$$

where $j = \sqrt{-1}$. The reader can verify that the transfer function definition of $\tilde{H}(s)$ shown in equation (13) satisfies equation (12)

$$\tilde{H}(s) = \frac{\xi_g(s)}{\upsilon(s)} = \sigma_g\sqrt{\frac{\tau_g}{T_\upsilon}}\frac{\left[1 + \sqrt{3}(\tau_g s)\right]}{(1 + \tau_g s)^2} \tag{13}$$

The transfer function $\tilde{H}(s)$ relates the Laplace transform of the gust-mode participation coefficient $\xi_g(s)$ to the Laplace transform of the digital random process $\upsilon(s)$. For the AFW simulation, two gust-mode participation coefficients were used: one for the symmetric gust mode and one for the antisymmetric gust mode. The actual state equations used in the simulation models to implement the transfer function defined in equation (13) are given by

$$\ddot{x}_g = -2\tau_g^{-1}\dot{x}_g - \tau_g^{-2}x + \sigma_g\tau_g^{-3/2}T_\upsilon^{-1/2}\upsilon \tag{14}$$

where υ is a Gaussian random process that is sampled and held every T_υ sec and σ_g is the desired rms velocity magnitude of the turbulence output. In both the batch and hot-bench simulations T_υ is the integration step size. The output equations

$$\left.\begin{aligned} \xi_g &= x_g + \tau_g\sqrt{3}\dot{x}_g \\ \dot{\xi}_g &= \dot{x}_g + \tau_g\sqrt{3}\ddot{x}_g \end{aligned}\right\} \tag{15}$$

define the modal participation coefficient ξ_g for the gust mode. In the limit, as the reduced frequency goes to zero, the symmetric gust-mode shape is equivalent to a simple uniform downwash mode. A more complete description of the gust-mode shapes used to model the turbulence can be found in Adams et al. (1992). Two sets of state and output equations were implemented, one for symmetric elastic dynamics and one for antisymmetric elastic dynamics.

Turbulence model parameters. Wind tunnel tests of the AFW model before the wingtip ballasts were installed had revealed resonance peaks in various model outputs due to natural wind tunnel turbulence at 10 Hz. In addition, the predicted flutter frequency of the AFW model with the wingtip ballast was expected to be near 10 Hz. A break frequency of 17.23 Hz produces a peak magnitude at 10 Hz in the transfer function defined in equation (13). A value of $\tau_g = 1/(2\pi 17.23)$ for the turbulence transfer function was used to approximate the expected wind tunnel turbulence.

Before the November 1989 test, the effect of TDT turbulence on the AFW aeroservoelastic response was unknown. As stated by Adams et al. (1992),

> No accurate representation of the wind-tunnel turbulence levels was available. Furthermore, the effect on the plant of any given turbulence intensity would be highly dependent on the configuration and the gust-mode shapes used to characterize the turbulence. Based on prior wind-tunnel entries, the rms turbulence velocity magnitude was estimated to be approximately 1 ft/sec at the wingtips at a Mach number of 0.5 and a dynamic pressure of 300 psf. This magnitude was conservatively assumed to apply at all test conditions.

A further decision was made to allocate the turbulence between the symmetric and antisymmetric models according to an 85:15-percent distribution as measured at the wingtips. The following symmetric and antisymmetric intensities resulted and were used before the 1989 test:

$$\left.\begin{aligned}\sigma_{g_{\rm sy}} &= 10.2 \text{ in/sec}\\ \sigma_{g_{\rm as}} &= 1.8 \text{ in/sec}\end{aligned}\right\} \qquad (16)$$

The antisymmetric intensity in equation (16) is the velocity induced at the wingtip of an antisymmetric gust mode. The symmetric intensity in equation (16) is the maximum velocity of a frozen sinusoidal symmetric gust mode moving with the free stream and having no variation in the spanwise *y* direction. As mentioned earlier, a more complete description of the gust mode shapes used to model the turbulence can be found in Adams et al. (1992).

In the batch and hot-bench simulations for the 1989 test, a single Gaussian random number sequence was used to generate both symmetric and antisymmetric gust velocity components. As pointed out by Adams et al. (1992), the use of two uncorrelated random numbers with the rms gust velocity components of $\sigma_{g_{\rm sy}} =$ 11.82 in/sec and $\sigma_{g_{\rm as}} = 2.085$ in/sec would have achieved a distribution of 85 and 15 percent, respectively, with a vector sum of 12 in/sec and would have been a better implementation. The simulation developed for the 1991 wind tunnel test used two independent random number inputs.

When the model is in the wind tunnel with a flutter suppression control law engaged and is subjected to only natural turbulence as excitation, control surface activity results. Figure 9 shows the rms value of commanded control surface rate for the TEO control surface plotted as a function of dynamic pressure for the three flutter control laws tested in November 1989. As figure 9 reveals, all three different flutter control laws generally resulted in the same observed rms levels of control surface activity in the TDT and generally the same levels of simulation overprediction of rms control activity. Although not explicitly shown in figure 9, analysis of data from the November 1989 wind tunnel test revealed that the rms simulation-predicted control surface activity was higher than the observed data.

When the turbulence intensities σ_g are defined as functions of dynamic pressure, simulation-predicted rms levels for control activity can be made to agree with the observed data. As shown in figure 9, the 1989 flutter suppression control law which produced experimental data the farthest beyond the open-loop flutter condition was the “traditional pole/loci” design described by Adams et al. (1992) and Waszak and Srinathkumar (1992). Figure 10 shows an example of tuning turbulence intensities based on the 1989 control activity levels for the case of the control law designed by traditional pole-zero loci methods.

Plotted in figure 10 as functions of dynamic pressure are the symmetric and antisymmetric intensities required to bring batch-simulation-generated rms results for the 1989 traditional pole-zero loci control law into agreement with various target metrics of control surface activity. Below 275 psf, the target metrics consisted of experimentally determined rms values of control surface position and rate. The filled circles represent the values of $\sigma_{g_{\rm as}}$ required to bring about agreement with rms antisymmetric control rate data. The open circles represent the values of $\sigma_{g_{\rm as}}$ required to bring about agreement with rms antisymmetric control position data; ideally, these would be the same. Similarly, the filled and open squares represent symmetric intensities $\sigma_{g_{\rm sy}}$ required to bring about agreement with symmetric control rate and position rms data. Above the dynamic pressure of 275 psf where no experimental data from the 1989 test were taken, the target rms values of control surface position and rate metrics were established by extrapolation of a smooth curved line through the 1989 rms data.

Note, that for each symmetry, one intensity function is required to bring about agreement between the predicted and the measured rms control positions, and another intensity function is required for agreement between the predicted and the measured rms commanded control rates. Because only one intensity function exists per symmetry, either the rms rate results or the rms position results—not both—can be matched. The solid lines (one per symmetry) in figure 10 represent the turbulence intensities selected for use after the 1989 test and are given by the following functions:

$$\left.\begin{aligned}\sigma_{g_{\rm sy}} &= 0.4 + 1.0\frac{\bar{q}}{100}\\ \sigma_{g_{\rm as}} &= 1.6 + 2.4\frac{\bar{q}}{100}\end{aligned}\right\} \qquad (17)$$

where dynamic pressure $\bar{q}$ is in psf and turbulence intensities σ_g are in in/sec. A simulation model was required that could be used up to 350 psf. The turbulence intensities shown in equation (17) were intended to satisfy the twin requirements of simplicity (a linear function of dynamic pressure) and to bound in a conservative manner the set of required intensity levels indicated in figure 10. Again, these intensity estimates depend both on the configuration and on the gust-mode shapes used to characterize the turbulence.

Figure 11 shows predicted versus observed control surface rms activity (1991 test) for the traditional pole-zero loci control law used to estimate the turbulence intensities by the procedure indicated in figure 10. Because this control law did not materially change between 1989 and 1991, the predicted and observed results are expected to be similar, and they are.

Figure 12 shows the predicted rms commanded control rates before the 1991 test versus those observed for an alternate flutter suppression control law described by Christhilf and Adams (1992). This optimization-based control law was changed substantially between the 1989 and 1991 tests. Because the optimization-based control law was not used in the estimation of turbulence intensities, it is a fair test of the turbulence intensity estimates. For the case shown, attempts to be conservative were generally successful. Above a dynamic pressure of 200 psf, the symmetric control rate activity was overpredicted. (See fig. 12.)

Actuators

Individual frequency responses for the eight actuators were measured with the wing elastic motion restrained with sandbags placed on the wings. Third-order transfer functions, with parameters optimized by the least-squares method, produced good fits to the measured frequency response data in the 3- to 30-Hz frequency range of interest. (See fig. 13.) In general, right and left members of a pair of actuated control surfaces (e.g., right TEO and left TEO) required different parameters to achieve a good fit and were, therefore, modeled individually. The third-order transfer function models allowed position, velocity, and acceleration of individual control surfaces to be predicted. The outputs of the right and left actuator models were resolved into symmetric and antisymmetric components that became inputs to the aeroelastic equations.

All the actuator position and command transfer functions had the following form:

$$\frac{\delta(s)}{\delta_c(s)} = \frac{k_\delta a_\delta \omega_\delta^2}{(s + a_\delta)\,(s^2 + 2\zeta_\delta \omega_\delta s + \omega_\delta^2)} \tag{18}$$

where $\delta(s)$ is the control surface deflection, $\delta_c(s)$ is the command, k_δ is the steady-state gain, $-a_\delta$ is the first-order pole location, ζ_δ is the damping of the complex pair, and ω_δ is the natural frequency of the complex pair. The first-order pole reflects the dynamics of hydraulic fluid flow through a small orifice, of which the size is regulated by an error signal consisting of the difference between the commanded and the measured actuator positions. The second-order complex pair results from the compressibility of the hydraulic fluid, the inertia of the control surface, the compliance of the structure, and the magnitude of the position error feedback gain. Rate limits, as a function of load, were specified by the manufacturer. In a first-order approximation, the rate limit is proportional to the maximum flow rate of a hydraulic fluid through a small orifice for a given difference between supply and chamber pressures. The mechanization of the rate limits is indicated in figure 14. An initial linear rate $\dot{x}_{\delta_{\text{lin}}}$ was first calculated as follows:

$$\dot{x}_{\delta_{\text{lin}}} = a_\delta\,(k_\delta \delta_c - x_\delta) \tag{19}$$

Positive and negative rate limits based on no-load rate limits modified by the hinge moment were formed as

$$rl_{\text{pos}} = rl_{\text{nl}} \sqrt{1 - \frac{F^\delta_{\text{HM}}}{F^\delta_{\text{HM STALL}}}} \tag{20}$$

$$rl_{\text{neg}} = -rl_{\text{nl}} \sqrt{1 + \frac{F^\delta_{\text{HM}}}{F^\delta_{\text{HM STALL}}}} \tag{21}$$

where the hinge moment F^δ_{HM} is positive for external load resisting positive actuator motion and $F^\delta_{\text{HM STALL}}$ represents the magnitude of actuator maximum load. Note that an assisting load will produce a rate limit that is larger than the no-load rate limit rl_{nl}. An assisting load occurs when a leading-edge surface is driven away from the zero deflection condition and when a trailing-edge surface is driven toward a zero deflection. The positive and negative limits were imposed on the linear rate $\dot{x}_{\delta_{\text{lin}}}$ as follows:

$$\dot{x}_\delta = \begin{cases} rl_{\text{pos}} & (\dot{x}_{\delta_{\text{lin}}} > rl_{\text{pos}}) \\ \dot{x}_{\delta_{\text{lin}}} & (rl_{\text{neg}} \le \dot{x}_{\delta_{\text{lin}}} \le rl_{\text{pos}}) \\ rl_{\text{neg}} & (\dot{x}_{\delta_{\text{lin}}} < rl_{\text{neg}}) \end{cases} \tag{22}$$

The state derivative $\dot{x}_\delta$ was integrated in time to produce the state x_δ, which was then used as a command to the second-order term of the actuator transfer function

$$\ddot{\delta} = \omega_\delta^2\,(x_\delta - \delta) - 2\zeta_\delta \omega_\delta \dot{\delta} \tag{23}$$

After the control surface positions, velocities, and accelerations were obtained, they were resolved into symmetric and antisymmetric components that became inputs of the aeroelastic equations. Figure 14 presents a signal flow diagram of the actuator dynamics described by equations (19)–(23).

In the simulation as mechanized for the AFW tests, the rate limits resulting from applied hinge moments were applied in the first-order pole part of the transfer function, the part associated with flow through a small orifice. Subsequent investigations have indicated that a better choice may have been to apply the limits to the final outputs of the actuator transfer functions.

Structural Model

Two finite-element structural representations of the AFW wind tunnel model were available. These structural models had ≈3400 degrees of freedom and represented the symmetric and the antisymmetric wind tunnel model fixed in roll with the wingtip store coupled. From these two finite-element structural models, six sets of reduced-order structural influence coefficient matrices were generated by defining a set of load points on the model, generally in the z direction (i.e., perpendicular to the wing plane). The six structural influence coefficient matrices are associated with the wind tunnel model in the different boundary and symmetry conditions shown in table II; each column entry indicates a unique structural influence coefficient matrix.

The symmetric influence coefficient matrices remain unchanged when the wind tunnel model sting condition changes from a fixed to a free-to-roll condition. A column of the structural influence coefficient matrix was generated by imposing a unit force at one load point and recording the resulting deflections induced at all the load points. These structural influence coefficient (SIC) matrices were combined with an appropriately dimensioned lumped-mass matrix in an eigenvalue analysis to generate natural frequencies and mode shapes. The resulting eigenvectors (mode shapes) were scaled to produce a generalized mass matrix of the form

$$\mathbf{M} = \frac{1}{12g}\begin{bmatrix} 1 & 0 & \dots & 0 \\ 0 & & \ddots & \vdots \\ \vdots & & \ddots & 0 \\ 0 & & \dots & 1 \end{bmatrix}$$

where $g = 32.159\ \text{ft/sec}^2$.

Ground vibration tests (GVT) were performed on both models before the wind tunnel tests. Mode shapes and natural frequencies corresponding to several of the lowest frequency modes were obtained and compared with the analytical predictions. The measured natural frequencies of these configurations were scaled to account for the differences between laboratory bench and wind tunnel mountings. For an earlier configuration of the AFW wind tunnel model, similar but without the wingtip ballast, ground vibration test data were available for both the laboratory bench and wind tunnel mountings. For this earlier configuration, ratios of measured frequencies (wind tunnel versus calibration laboratory) could be calculated for each mode. These ratios were applied to the GVT-measured frequencies of the AFW wind tunnel models that are discussed herein.

Despite the fact that the wind tunnel model was structurally unchanged between the 1989 and 1991 tests, several differences were evident in the modeling strategy, which was intended to improve dynamic predictions at and above the onset of flutter. For the 1989 models, 146 load points were used in the calculation of the symmetric SIC matrices, and 160 load points were used in the calculation of the antisymmetric SIC matrices. To build up the generalized aerodynamic coefficients that describe the aerodynamic interactions between elastic modes, slopes and displacements at the collocation points of the aerodynamic boxes had to be derived by interpolation from neighboring points where elastic deformation is defined. To provide more points for interpolation and to improve the aerodynamic model for the 1991 simulation, the symmetric load points were increased to 204 and the antisymmetric load points to 218.

Another difference between the 1989 and 1991 structural models involved the selection and frequencies of the elastic modes used to build up the aeroservoelastic model. For the 1989 test, only those elastic modes which (with one exception) could be clearly identified in 1989 GVT's conducted in the TDT calibration laboratory were used to formulate the simulation models. Analytically derived mode shapes were used in conjunction with the GVT-measured frequencies. An attempt was made to characterize mode shapes empirically so the measured frequencies could be correlated with the predicted frequencies. Table III shows that in the 1989 simulation model eight symmetric elastic modes and seven antisymmetric, fixed-in-roll, elastic modes (rows labeled "1989 Used") were used in the mathematical model. The analytically predicted symmetric modes E5 and E10 were not retained in the 1989 simulation model. Similarly, analytically predicted antisymmetric fixed-in-roll modes E4, E8, and E10 were not included in the 1989 simulation model. Despite the fact that the antisymmetric fixed-in-roll mode E9 was not clearly identified by its mode shape in the GVT, the antisymmetric E9 mode was used in the simulation model (the one exception) as it contributed to the flutter solution. As with the other modes, the analytically predicted mode shape was used. The frequency used for antisymmetric E9 was obtained by scaling the predicted E9 frequency according to the ratio between the predicted and measured values of frequency for antisymmetric fixed-in-roll mode E7. The free-to-roll case was not included in the 1989 simulation, as free-to-roll flutter suppression was not part of the wind tunnel test plan.

After the 1989 test, an attempt was made to improve the flutter prediction capability of the equations of motion. The finite-element structural models were adjusted so that analytically generated frequencies agreed more closely with the GVT frequencies. The *in vacuo* frequencies for the modal structural degrees of freedom were also changed. Generally, the frequencies for the symmetric modes were derived from a combination of 1989 and 1986 GVT results. For the 1986 wind tunnel test, GVT tests were conducted on the model mounted in both the TDT and the TDT calibration laboratory. For these data a set of ratios was derived by division of the frequency measured in the wind tunnel by the frequency measured in the calibration laboratory. The difference in the frequencies results from the calibration laboratory mounting apparatus, by necessity, being more rigid than the wind tunnel sting. For the 1991 simulation model, these ratios were applied to the 1989 GVT frequencies for symmetric modes E1–E4 and E6–E9. (See table III.) For the 1991 symmetric mathematical model, analytically predicted finite-element model frequencies were used for symmetric modes E5 and E10. For the 1991 fixed-in-roll antisymmetric mathematical model, analytically predicted finite-element model frequencies were used for antisymmetric modes E7 and E8. The frequencies for the remaining antisymmetric modes were derived, in the manner just previously described, from 1989 GVT results and 1986 GVT ratios. The 1991 free-to-roll model used analytically predicted finite-element-model frequencies, as GVT results could not be obtained for the free-to-roll boundary condition.

The first 10 symmetric modes and the first 9 antisymmetric modes were used to form the 1991 aeroservoelastic models. For the case of the antisymmetric free-to-roll condition, mode 1 was the rigid roll mode, and modes 2–10 were elastic modes E1–E9. For the fixed-in-roll case, simulation implementation was made easier and more consistent by retention of the same mode order as that of the free-to-roll case. Thus, the rigid roll mode remained mode 1 in the fixed-in-roll case but was kept frozen.

Aerodynamic Model

The unsteady aerodynamics induced by the elastic motion of the AFW were computed with the doublet-lattice lifting surface method (Giesing, Kalman, and Rodden (1971)) as implemented in the interaction of structures, aerodynamics, and controls system (ISAC) (Peele and Adams (1979), Adams and Hoadley (1993)) of computer codes. Doublet-lattice theory is a linear, frequency domain theory limited to subsonic flows. The wind tunnel model was represented aerodynamically as a half model with a plane of symmetry at the fuselage centerline. In doublet-lattice theory, lifting surfaces are modeled as zero-thickness plates with aerodynamic boxes as shown in figure 15. The aerodynamic paneling was defined so that box boundaries coincided with control surface edges.

To improve the prediction of the aerodynamic loads induced by control surface deflections, the analytical control derivatives were corrected from wind tunnel measurements of lift and rolling moment. The control derivatives were assumed to consist of a rigid component and an elastic increment; the elastic increment is a function of dynamic pressure $\bar{q}$. The resulting decomposition is shown in the following equation and in figure 16(a) with the use of the rolling-moment coefficient C_l as an example. Thus,

$$C_{l_\delta} = C_{l_{\delta_{\text{rigid}}}} + C_{l_{\delta_{\text{elastic}}}}(\bar{q}) \tag{24}$$

Both analytical predictions and experimental data (fig. 16(b)) were decomposed into these two terms. The rigid values of the analytical model were then scaled to match the rigid values of the experimental data. The scaling was accomplished as indicated in

$$C_{l_\delta} = k_{\text{rigid}}\left(C_{l_{\delta_{\text{rigid}}}}\right)_{\text{analytical}} + k_{\text{elastic}}\left[C_{l_{\delta_{\text{elastic}}}}(\bar{q})\right]_{\text{analytical}} \tag{25}$$

where

$$k_{\text{rigid}} = \frac{\left(C_{l_{\delta_{\text{rigid}}}}\right)_{\text{experimental}}}{\left(C_{l_{\delta_{\text{rigid}}}}\right)_{\text{analytical}}}$$

and

$$k_{\text{elastic}} = \left[\frac{\left(C_{l_{\delta_{\text{elastic}}}}\right)_{\text{experimental}}}{\left(C_{l_{\delta_{\text{elastic}}}}\right)_{\text{analytical}}}\right]_{\text{average}}$$

Because of limited experimental data, the scaling factor for the elastic increment was assumed to be constant with dynamic pressure. The elastic increments of the analytical model were scaled with correction factors based on the average ratio of analytical to experimental data for a dynamic pressure range of 250 psf.

Before the 1989 test, an extensive trade-off study was performed to model the wingtip ballast stores either as flat lifting surfaces or as slender bodies. The flat-plate representation of the wingtip ballast store was selected, primarily because more time was required to perform the repeated slender-body analyses. The flat-plate aerodynamic model was equal in width, but shorter in length, than the actual wingtip ballast stores. The box layout and overall dimensions were chosen so that results for the flat-plate and slender-body models matched at Mach 0.9 for heavy gas. A flat-plate model was then used for the remainder of the program.

Aeroelastic Equations

The aeroelastic equations in a frequency domain format of Tiffany and Adams (1988) follow:

$$\left\{-\omega^2\begin{bmatrix}\mathbf{M}^{ff} & \mathbf{M}^{fc}\\ \mathbf{M}^{cf} & \mathbf{M}^{cc}\end{bmatrix} + j\omega\begin{bmatrix}\mathbf{G}^{ff} & \mathbf{0}\\ \mathbf{0} & \mathbf{0}\end{bmatrix} + \begin{bmatrix}\mathbf{K}^{ff} & \mathbf{0}\\ \mathbf{0} & \mathbf{0}\end{bmatrix} + \bar{q}\begin{bmatrix}\mathbf{Q}^{ff}(\omega) & \mathbf{Q}^{fc}(\omega)\\ \mathbf{Q}^{cf}(\omega) & \mathbf{Q}^{cc}(\omega)\end{bmatrix}\right\}$$

$$\times\begin{Bmatrix}\vec{\eta}\\ \vec{\delta}\end{Bmatrix} = -\bar{q}\begin{Bmatrix}\mathbf{Q}^{fg}(\omega)\\ \mathbf{Q}^{cg}(\omega)\end{Bmatrix}\frac{\xi_g}{V} - \begin{Bmatrix}\mathbf{0}\\ \mathbf{F}^{\delta}_{\mathrm{HM}}\end{Bmatrix} \qquad (26)$$

where $j = \sqrt{-1}$, ω is the frequency in rad/sec, $\bar{q} = (1/2)\rho V^2$ is the dynamic pressure, ρ is density, V is the airspeed, **M** is the mass matrix, **G** is the damping matrix, **K** is the stiffness matrix, $\mathbf{Q}(\omega)$ is a matrix of generalized aerodynamic forces, and ξ_g is an external input representing the gust-mode participation coefficient.

The format in equation (26) proceeds from the second-order matrix structural equations wherein the *in vacuo* elastic modes are basis functions or generalized coordinates. The elastic modes in the vector $\vec{\eta}$ are orthogonal so the elastic mode mass and stiffness matrices $\mathbf{M}^{ff}$ and $\mathbf{K}^{ff}$ are diagonal. Modal damping of 0.03 is assumed for each mode and is represented in the diagonal matrix $\mathbf{G}^{ff}$. The *in vacuo* elastic modes were augmented with control modes δ that represent control surface deflections. The *in vacuo* elastic and control modes are used as basis functions to describe structural and control surface displacements, velocities, and accelerations by superposition.

The control modes in equation (26) represent idealized control surfaces that are free to rotate; hence, the control modes have zero stiffness or, equivalently, $\mathbf{K}^{cc} = \mathbf{0}$. The effect of actuator stiffness is assumed to be captured by the actuator transfer functions. When equation (26) is adjoined to equation (18), individual control surfaces have the effect of stiffness but are not coupled with each other or with the elastic modes by a stiffness matrix. The result is that acceleration cannot be induced in control surface j by *in vacuo* displacement in control surface i. Coupling between the elastic and the control modes occurs only by inertial coupling $\mathbf{M}^{fc}$ and induced aerodynamic loads $\mathbf{Q}^{fc}$ and $\mathbf{Q}^{cf}$.

Control mode position, rate, and accelerations are provided as inputs to equation (26) by the actuator transfer function models described in the section "Actuators." If the control mode motion is treated as prescribed, the δ components in equation (26) can be solved for the vector of hinge moments $\mathbf{F}^{\delta}_{\mathrm{HM}}$, which are then used in the actuator rate limit calculations. To complete equation (26), the second-order matrix structural equations in the generalized coordinate vector $\begin{Bmatrix}\vec{\eta}\\ \vec{\delta}\end{Bmatrix}$ are augmented with generalized aerodynamic force coefficient matrices $\mathbf{Q}(\omega)$. Equation (26) applies either to symmetric or antisymmetric motion. Low-frequency subsets of the elastic modes of free vibration from a large-order structural model are typically used in an aeroelastic formulation. For the AFW simulations, 7–10 flexible modes $\vec{\eta}$ per symmetry were retained. (See table III.)

The matrices $\mathbf{Q}(\omega)$ that augment the *in vacuo* second-order matrix structural equations result when steady harmonic motion is assumed in the solution of the linear form of the governing equation for unsteady, compressible flow. For subsonic flow, these solutions can be computed using doublet-lattice theory and are tabulated at specific frequencies; the generalized solution would be a continuous function of frequency. To formulate the aeroelastic equations in the time domain, the generalized aerodynamic forces should be obtained as functions of the Laplace variable s. The matrix function $\mathbf{Q}(\omega)$ can be approximated by matrix expressions that are rational in s. Several methods and theories can be used to construct rational function approximations (RFA's) to the functions $\mathbf{Q}(\omega)$, most of which are discussed by Tiffany and Adams (1988). The least-squares form of approximation (Tiffany and Adams (1988)) is given by

$$\hat{\mathbf{Q}}(s) = \mathbf{A}_0 + \mathbf{A}_1\tau s + \mathbf{A}_2(\tau s)^2 + \sum_{m=1}^{n_{\mathrm{lag}}}\mathbf{A}_{2+m}\left(\frac{\tau s}{\tau s + \beta_m}\right) \qquad (27)$$

where $\tau = (\bar{c}/2V)$, $\bar{c}$ is a reference length (the wing mean aerodynamic chord), V is the airspeed, β_m is a nondimensional reduced frequency, and $\mathbf{A}_i$ are matrix constants that must be solved for in the approximation. The order of the least-squares fit is indicated by n_{lag} and is typically, 3, or 4. The circumflex (or hat) above the matrix symbol $\hat{\mathbf{Q}}(s)$ indicates that it is an estimate of $\mathbf{Q}(\omega)$ when $j\omega$ is replaced by s.

An alternate approach to the least-squares formulation of the generalized aerodynamic forces is the minimum state formulation, which was described and refined by Tiffany and Adams (1988) and originated by Karpel (1981). The minimum state formulation follows:d

$$\hat{\mathbf{Q}}(s) = \mathbf{A}_0 + \mathbf{A}_1\tau s + \mathbf{A}_2(\tau s)^2 + \tilde{\mathbf{D}}(\tau s\mathbf{I} - \mathbf{R})^{-1}\tilde{\mathbf{E}}\tau s \qquad (28)$$

where **R** is an $n_{\mathrm{lag}} \times n_{\mathrm{lag}}$ diagonal matrix and $\tilde{\mathbf{D}}$ and $\tilde{\mathbf{E}}$ are fully populated matrices of appropriate dimensions. For the minimum state approximation, the total number of aerodynamic states added is equal to n_{lag}, which is the dimension of **R**. A detailed comparison of the minimum state method with the least-squares and other RFA methods was performed by Tiffany and Adams (1988). Briefly, the advantage of the minimum state method is that the number of aerodynamic lag states required can easily be a 10th of that required by the least-squares method for similar accuracy. The disadvantage is that the solution for $\mathbf{D}$ and $\mathbf{E}$ requires a nonlinear optimization.

Initially, the minimum state method was chosen to form the 1989 aeroelastic models. As described in the section entitled "Aerodynamic Model," rigid and elastic effectiveness factors were derived empirically from the data of the 1986 and 1987 TDT tests for incorporation into the aeroelastic model. The fully populated nature of the $\mathbf{D}$ and $\mathbf{E}$ matrices made this inclusion impossible in some cases. The minimum state method could have been reformulated so that $\mathbf{D}$ and $\mathbf{E}$ were appropriately block diagonal, but this approach would have raised the number of states required and added another bookkeeping burden. The minimum state approach was then abandoned. A least-squares 1-lag formulation was ultimately used in the 1989 simulation model, and a least-squares 4-lag form was used for the 1991 simulation model.

Equation (26) (with $j\omega$ replaced by s) can be combined with equation (27) to produce the time domain aeroelastic equations used in the simulations and shown below in equations (29a) and (29b). The second-order *in vacuo* equations (top row of eq. (26)) are thereby augmented with unsteady aerodynamic lag states $\mathbf{x}^{f}_{a_m}$ arising from the denominator term summed in equation (27).

$$
\begin{aligned}
&\left(\mathbf{M}^{ff} + \bar{q}\tau^2\mathbf{A}^{ff}_2\right)\ddot{\vec{\eta}} + \left(\mathbf{G}^{ff} + \bar{q}\tau\mathbf{A}^{ff}_1\right)\dot{\vec{\eta}} + \left(\mathbf{K}^{ff} + \bar{q}\mathbf{A}^{ff}_0\right)\vec{\eta} \\
&\qquad - \bar{q}\tau\sum_{m=1}^{n_{\text{lag}}}\mathbf{x}^{f}_{a_m} = -\bar{q}\left[\tau\mathbf{A}^{fg}_1\left(\frac{\dot{\xi}_g}{V}\right) - \mathbf{A}^{fg}_0\left(\frac{\xi_g}{V}\right)\right] \\
&\qquad - \left(\mathbf{M}^{fc} + \bar{q}\tau^2\mathbf{A}^{fc}_2\right)\ddot{\vec{\delta}} - \left(\bar{q}\tau\mathbf{A}^{fc}_1\right)\dot{\vec{\delta}} - \left(\bar{q}\mathbf{A}^{fc}_0\right)\vec{\delta}
\end{aligned}
\tag{29a}
$$

$$
\begin{aligned}
&\dot{\mathbf{x}}^{f}_{a_m} + \left(\frac{\beta_m}{\tau}\right)\mathbf{x}^{f}_{a_m} + \left[\mathbf{A}^{ff}_{m+2} \;\; \mathbf{A}^{fc}_{m+2}\right]\begin{Bmatrix}\dot{\vec{\eta}} \\ \dot{\vec{\delta}}\end{Bmatrix} \\
&\qquad = -\mathbf{A}^{fg}_{m+2}\left(\frac{\dot{\xi}_g}{V}\right) \qquad (m = 1, 2, \ldots, n_{\text{lag}})
\end{aligned}
\tag{29b}
$$

where

$$
n_{\text{lag}} = \begin{cases} 1 & (\text{for 1989 test}) \\ 4 & (\text{for 1991 test}) \end{cases}
$$

Control surface positions, rates, and accelerations, as well as turbulence, are treated as external inputs. The vectors $\vec{\eta}$ and $\mathbf{x}^{f}_{a_m}$ are both $n_f \times 1$, where n_f is the number of retained elastic modes. Equation (29a) is used to solve for the vector of elastic mode accelerations $\ddot{\vec{\eta}}$, which can be integrated to find the rates $\dot{\vec{\eta}}$ and displacements $\vec{\eta}$. The derivative calculations indicated in equations (29a) and (29b) are performed for each symmetry in the simulations. The symmetric and antisymmetric components of the final accelerometer outputs were resolved into right and left components before output.

Equations (30a) and (30b) that follow are used to calculate actuator hinge moments. A positive hinge moment in this case resists positive actuator motion. The hinge moments are used in the calculation of rate limits for the actuators. Thus,

$$
\begin{aligned}
\mathbf{F}^{c}_{\text{HM}} = {} & \left[\mathbf{M}^{cf} + \bar{q}\tau^2\mathbf{A}^{cf}_2 \quad \bar{q}\tau^2\mathbf{A}^{cc}_2\right]\begin{Bmatrix}\ddot{\vec{\eta}} \\ \ddot{\vec{\delta}}\end{Bmatrix} \\
& + \bar{q}\tau\left[\mathbf{A}^{cf}_1 \quad \mathbf{A}^{cc}_1\right]\begin{Bmatrix}\dot{\vec{\eta}} \\ \dot{\vec{\delta}}\end{Bmatrix} \\
& + \bar{q}\left[\mathbf{A}^{cf}_0 \quad \mathbf{A}^{cc}_0\right]\begin{Bmatrix}\vec{\eta} \\ \vec{\delta}\end{Bmatrix} - \bar{q}\tau\sum_{m=1}^{n_{\text{lag}}}\mathbf{x}^{c}_{a_m} \\
& + \bar{q}\left[\mathbf{A}^{cg}_0 \quad \tau\mathbf{A}^{cg}_1\right]\begin{Bmatrix}\dfrac{\xi_g}{V} \\ \dfrac{\dot{\xi}_g}{V}\end{Bmatrix}
\end{aligned}
\tag{30a}
$$

$$
\begin{aligned}
&\dot{\mathbf{x}}^{c}_{a_m} + \left(\frac{\beta_m}{\tau}\right)\mathbf{x}^{c}_{a_m} + \left[\mathbf{A}^{cf}_{m+2} \quad \mathbf{A}^{cc}_{m+2}\right]\begin{Bmatrix}\dot{\vec{\eta}} \\ \dot{\vec{\delta}}\end{Bmatrix} \\
&\qquad = -\mathbf{A}^{cg}_{m+2}\left(\frac{\dot{\xi}_g}{V}\right) \qquad (m = 1, 2, \ldots, n_{\text{lag}})
\end{aligned}
\tag{30b}
$$

Analog Filters

For all the simulations, the dynamics of the analog antialiasing filters on the 40 primary outputs were simulated. Both single-pole filters with a break frequency of 25 Hz and fourth-order Butterworth filters with break frequencies of 100 Hz had been assembled and were available for use in the wind tunnel. Only the single-pole filters were used in both the 1989 and 1991 wind tunnel tests. The single-pole filters set at a quarter of the Nyquist frequency effectively blocked power above

100 Hz from reflecting back into the digital system in the flutter frequency range. The single-pole filters also provided roll-off above the 30-Hz bandwidth of the actuators. (See fig. 13.)

The single-pole antialiasing filters were implemented with the following equation:

$$\frac{y(s)}{u(s)} = \frac{1}{\frac{s}{\omega_{aa}} + 1} \tag{31}$$

where ω_{aa} is the break frequency (rad/sec). Analog notch filters were unique to each control law implementation; for the hot-bench tests, notch filter dynamics were included in controller dynamics and are not described herein. Controller implementation is described by Hoadley and McGraw (1992) and, to a lesser extent, by Adams et al. (1992).

Tabulation of Mathematical Model Equations

The equations that define the mathematical model to be discretized and implemented are summarized in table IV. Figure 8 indicates the general flow of information between the subsystem models. The section entitled "Simulation Structure and Implementation" discusses the implementation of the equations in table IV.

Flutter Predictions and Frequency Response

The predicted flutter characteristics with doublet-lattice aerodynamics for a Mach number of 0.5 in the 1989 and 1991 mathematical models are shown in table V along with measured characteristics. Again, the Mach number range for the 1989 and 1991 tests in the TDT was essentially low subsonic and is well approximated, at least in terms of compressibility effects, by calculations for a Mach number of 0.5. For these predictions, generalized aerodynamic force coefficients were in a frequency domain format, and the approximations indicated in equation (27) were not required. When these approximations were used for a time domain representation, the results were, generally, within 1 percent of the flutter dynamic pressures and frequencies shown in table V. As seen from the maximum static pressure (2200 psf) contour line in figure 3, the test range for the AFW model in the TDT was generally between Mach numbers of 0.1 and 0.5.

Figure 17 shows a comparison of the predicted (1991 simulation) and measured frequency response of the symmetric component of the wingtip accelerometer signal to the commanded TEO control surface. The wingtip accelerometer and TEO control surface combination was the principal sensor and actuator pair in all three of the flutter suppression control laws that used accelerometer feedback. (See Christhilf and Adams (1992), Mukhopadhyay (1992), and Waszak and Srinathkumar (1992).) The comparison is made at a dynamic pressure of 225 psf and at a Mach number of approximately 0.4 (fig. 3), which is below both the analytically predicted and experimentally determined symmetric flutter dynamic pressures. These results are for the free-to-roll condition for which the antisymmetric flutter boundary was beyond the range of the TDT. Figure 17 indicates those coupled aeroservoelastic modes at 225 psf that are dominated by and identified with the *in vacuo* vibration modes characterized as wing first bending and wing first torsion. As dynamic pressure is increased to near flutter, substantial aerodynamic coupling occurs. Recall that when dynamic pressure is made nonzero in an analysis, the mode labeled "Wing first torsion" has contributions from all the *in vacuo* elastic modes that form the generalized coordinates of the aeroservoelastic system.

The measured and predicted symmetric flutter frequencies from table V are also indicated in figure 17. The frequency shift between the predicted and measured wing first-bending peak responses is about 0.7 Hz and is seen clearly in the Bode plots of figure 17. The difference in predicted and measured frequencies of the wing first-torsion modes is similar to the difference in wing first-bending peaks but is obscured by the insensitivity of the wingtip accelerometer to the wing first-torsion mode. The wingtip accelerometer is near the node line of the wing first torsion *in vacuo* elastic mode. Eigenvalue analysis of the analytical model at a dynamic pressure near zero was used to determine the frequency of the wing first-torsion mode shown in figure 17, and the actual frequency of the wing first-torsion mode in the wind tunnel test was assumed to be similarly situated along the measured Bode plot.

Note that the frequency of experimentally determined flutter (which occurred at about 235 psf) is approximately halfway between the aerodynamically coupled modes identified as wing first bending and wing first torsion at a dynamic pressure of 225 psf. The classical bending and torsion flutter occurs when the bending mode stiffens and the torsion mode softens as dynamic pressure is increased, which allows the modes to coalesce. The frequency of the flutter observed in the wind tunnel is consistent with the stiffening and softening process that is approximately equal for both modes. The predicted flutter frequency (11.2 Hz at 248 psf) shows that almost no further softening of the wing first-torsion mode occurs in the analytical model as dynamic pressure increases from 225 psf to the analytical flutter frequency. As a result, predicted mode coalescence occurs at a higher frequency and dynamic pressure than if the predicted first-torsion mode softened in a manner more consistent with the measured result. Because the analytical *in vacuo* frequencies generally agreed with ground vibration test results, the discrepancies indicated in table V and figure 17 must arise in the prediction of the generalized aerodynamic forces and/or the mode shapes. The symmetric first-torsion mode, even after structural model refinement, proved the most difficult to identify and verify during ground vibration tests. Although the predicted first-torsion mode shape and/or the generalized aerodynamic forces associated with the first-torsion mode is likely to have been the source of the errors, a definitive answer has not been found.

Mathematical Model Summary

Essentially linear methods were applied that represent the state of the art for processes used routinely in development. The requirement for generating numerous design models for various boundary conditions (symmetric, antisymmetric free to roll, or antisymmetric fixed in roll combined with wingtip store coupled or wingtip store uncoupled) precluded extensive use of nonlinear computational fluid dynamics (CFD) codes. The methods generally predicted the dynamic pressure at which flutter would occur within 6 percent. (See table V.) A conservative prediction, rather than nonconservative, would have been more satisfactory. An argument for reducing the certification flutter margins cannot be made here. The percentage of error of the predicted flutter frequency (16 percent) is greater than the percentage of error of predicted dynamic pressure. The prediction of transfer function representations between specific input-output pairs is even more difficult. Before active flutter suppression can become an accepted design practice, the flutter phenomenon must have an improved model of input and output in the critical frequency range. Conversely, the control designer is challenged to ensure that control systems are robust to known or probable errors in plant characterization.

The prediction of flutter in the transonic regime, where it is normally critical (fig. 1), is more difficult than in the midsubsonic regime where the AFW flutter suppression work was done. Some work on applying a code based on the transonic small disturbance theory is reported by Silva and Bennett (1992).

A complete set of continuous time differential equations, suitable for both batch and real-time implementation, was presented. Theoretical justifications for the implementation equations used in the Dryden turbulence formulation were presented. The inclusion of fully nonlinear rigid-body degrees of freedom (with the exception of the roll degree of freedom, which was treated as an elastic mode) was not required for this application but is addressed in other references, notably Cutchins et al. (1983), Buttrill et al. (1987), Morino and Baillieul (1987), and Waszak and Schmidt (1988).

Simulation Structure and Implementation

The implementation method, wherein the hot-bench simulation is updated by data extracted from the batch simulation, is depicted schematically in figure 8. The mathematical model can be viewed (fig. 8) as three component models connected serially (except for the hinge moments). The first component model (labeled "Rate-limited actuator dynamics") consists of the first-order poles associated with eight empirically derived actuator transfer functions. The second component model (labeled "Aeroservoelastic dynamics") consists of the aeroelastic equations together with the remaining second-order terms of the actuator transfer functions. If dynamic pressure is held constant, the aeroservoelastic dynamic model is linear time invariant. The third component model consists of 40 linear first-order antialiasing filter equations applied to the simulated sensor outputs of the aeroservoelastic dynamic model.

The aeroservoelastic dynamics block in figure 8 consists of state equations (29) and (30) together with algebraic output equations to predict the required accelerometer, strain gage, and pressure transducer outputs from the states. Together with the 16 states associated with the second-order terms of 8 actuator transfer functions and n states from the aeroelastic model, a coupled linear system of $n + 16$ states, 10 inputs (8 actuator and 2 noise), and 40 outputs can be extracted from the linear portion of the batch simulation. As indicated in table , for the 1989 simulation model, $n = 57$ $(73 - 16)$; for the 1991 mathematical model, $n = 156$ $(172 - 16)$.

For the hot-bench implementation, we were compelled to keep the timescale as close to real time as possible. During the hot-bench tests before the 1991 mathematical model was developed, productivity dictated that a timescale of 1:5 (full Cyber) was the maximum reduction allowable for effective hot-bench tests; below this ratio, too few data acquisition runs could be performed in a 2- to 3-hr hot-bench test session. If the hot-bench simulation is restricted to a fixed wind tunnel operating point for a given run (i.e., density, Mach number, and airspeed are held fixed), then, after rate limiting is performed on the actuator transfer functions, the remaining dynamics in the simulation are linear. Utilization of a state transition method of discretization on these dynamics permitted the hot-bench integration step to be 0.0025 sec, which is consistent with the hot-bench update rate. If all the state derivatives defined in the model equations (table IV) were simply integrated numerically, the required integration step size would have been

0.0005 sec to ensure numerical stability of the highest frequency dynamics. (See Buttrill and Houck (1990).)

The nonlinear part involves only eight states, one from each actuator. Each state is integrated numerically with an integration step of 0.000625 sec. Four integration steps are made to predict the value of the input to the coupled linear system at time $(k+1)h$ where $h = 0.0025$ sec. Because input to the coupled linear system at time $(k+1)h$ is now available, a trapezoidal state transition scheme can be used. Let $\mathbf{u}_k$ denote the quantity $\mathbf{u}(kh)$. Given the linear dynamic system

$$\dot{\mathbf{x}} = \mathbf{A}\mathbf{x} + \mathbf{B}\mathbf{u} \tag{32}$$

if the ramp input signal

$$\mathbf{u}(t) = \mathbf{u}_k + (t - kh)\left(\frac{\mathbf{u}_{k+1} - \mathbf{u}_k}{h}\right) \tag{33}$$

is defined in the interval $kh \le t < (k+1)h$ then the following exact solution for $\mathbf{x}$ at time $t = (k+1)h$ exists:

$$\mathbf{x}_{k+1} = \mathbf{F}_k \mathbf{x}_k + \mathbf{G}_k^{\text{trap}} \mathbf{u}_k + \mathbf{G}_{k+1}^{\text{trap}} \mathbf{u}_{k+1} \tag{34}$$

where

$$\mathbf{F}_k = e^{\mathbf{A}h} \tag{35}$$

$$\mathbf{G}_k^{\text{trap}} = \left(-e^{\mathbf{A}h} + e^{\mathbf{A}h}\mathbf{A}^{-1}h^{-1} - \mathbf{A}^{-1}h^{-1}\right)\left(-\mathbf{A}^{-1}\mathbf{B}\right) \tag{36}$$

$$\mathbf{G}_{k+1}^{\text{trap}} = \left(\mathbf{I} - e^{\mathbf{A}h}\mathbf{A}^{-1}h^{-1} + \mathbf{A}^{-1}h^{-1}\right)\left(-\mathbf{A}^{-1}\mathbf{B}\right) \tag{37}$$

A derivation of equations (34)–(37) is given in appendix C.

Instead of a ramp signal, if $\mathbf{u}(t)$ is assumed to be constant in the interval $kh \le t < (k+1)h$ as would be the case in a sample and zero-order hold, a more familiar state transition formula is given by

$$\mathbf{x}_{k+1} = \mathbf{F}_k \mathbf{x}_k + \mathbf{G}_k^{\text{zero}} \mathbf{u}_k \tag{38}$$

where

$$\begin{aligned} \mathbf{G}_k^{\text{zero}} &= \mathbf{G}_k^{\text{trap}} + \mathbf{G}_{k+1}^{\text{trap}} \\ &= \left(\mathbf{I} - e^{\mathbf{A}h}\right)\left(-\mathbf{A}^{-1}\mathbf{B}\right) \end{aligned} \tag{39}$$

As an additional check, observe that for the following simple scalar transfer function,

$$\frac{y(s)}{u(s)} = \frac{1}{\tau s + 1} \tag{40}$$

we have

$$\left.\begin{aligned} \mathbf{A} &= -\left(\frac{1}{\tau}\right) \\ \mathbf{B} &= \frac{1}{\tau} \end{aligned}\right\} \tag{41}$$

and when implemented with a zero-order sample and hold, equations (34) and (38) simplify to

$$\left.\begin{aligned} \mathbf{F}_k &= e^{\mathbf{A}h} = e^{-(1/\tau)h} \\ \mathbf{G}_k^{\text{zero}} &= \left(\mathbf{I} - e^{\mathbf{A}h}\right)\left(-\mathbf{A}^{-1}\mathbf{B}\right) = 1 - e^{-(1/\tau)h} \end{aligned}\right\} \tag{42}$$

so that $\mathbf{F}_k + \mathbf{G}_k^{\text{zero}} = \mathbf{I} = 1$, as expected.

Clearly, the direct evaluation of $\mathbf{G}_k^{\text{trap}}$ and $\mathbf{G}_{k+1}^{\text{trap}}$ by the use of equations (36) and (37) will not work if $\mathbf{A}$ is singular, as would occur if $\mathbf{A}$ included rigid-body modes with zero eigenvalues. However, with application of the Taylor series expansion

$$e^{\mathbf{A}h} = \mathbf{I} + \mathbf{A}h + \frac{1}{2}(\mathbf{A}h)^2 + \ldots = \sum_{p=0}^{\infty} \frac{1}{p!}(\mathbf{A}h)^p$$

and recognition that

$$\mathbf{A}e^{\mathbf{A}} = e^{\mathbf{A}}\mathbf{A}$$

the equations for $\mathbf{G}_k^{\text{trap}}$ and $\mathbf{G}_{k+1}^{\text{trap}}$ are developed into a form that can be calculated if $\mathbf{A}$ has zero eigenvalues. Thus,

$$\mathbf{G}_k^{\text{trap}} = h\left[\sum_{p=2}^{\infty} \frac{1}{p!}(-1)^p(\mathbf{A}h)^{p-2}\right] e^{\mathbf{A}h}\mathbf{B} \tag{43}$$

$$\mathbf{G}_{k+1}^{\text{trap}} = h\left[\sum_{p=2}^{\infty} \frac{1}{p!}(\mathbf{A}h)^{p-2}\right]\mathbf{B} \tag{44}$$

The matrices $\mathbf{G}_k^{\text{trap}}$ and $\mathbf{G}_{k+1}^{\text{trap}}$ can be calculated by summation of the aforementioned Taylor series until the next term is under some required tolerance. When applied to the 1989 model, procedures to sum the series defined by equations (42) and (43) converged without difficulty.

The antialiasing filters are applied individually to each output signal, which results in a diagonal system. Therefore, these filters are not lumped with the coupled linear system to avoid full matrix operations. The antialiasing filter dynamics are digitized in a sequential manner that uses a scalar form of the trapezoidal state transition method described earlier. For single-pole anti-aliasing filters given by

$$\frac{y(s)}{u(s)} = \frac{1}{\frac{s}{\omega_{aa}} + 1} \tag{45}$$

the state transition equations are

$$\begin{aligned} y(t+h) &= e^{-(\omega_{aa}h)} y(t) + g_k^{\text{trap}} u(t) \\ &\quad + g_{k+1}^{\text{trap}} u(t+h) \end{aligned} \tag{46}$$

where

$$g_k^{\text{trap}} = e^{-(\omega_{aa}h)} (\omega_{aa}h)^{-1} + (\omega_{aa}h)^{-1} - e^{-(\omega_{aa}h)} \tag{47}$$

$$g_{k+1}^{\text{trap}} = 1 + e^{-(\omega_{aa}h)} (\omega_{aa}h)^{-1} - (\omega_{aa}h)^{-1} \tag{48}$$

Note that the term $(-\mathbf{A}^{-1}\mathbf{B})$ in equations (36) and (37) becomes unity in equations (47) and (48).

Model Reduction Method

Rationale for Model Reduction

In preparation for the 1991 test, the mathematical model of 1989 was updated to improve the ability to predict flutter frequency and the dynamic pressure. (See Buttrill and Houck (1990).) As discussed in the section entitled “Simulation Structure and Implementation,” the aeroservoelastic part of the mathematical model grew from 73 states in the 1989 mathematical model to 172 states in the 1991 mathematical model. (See table .)

The 1989 mathematical model was implemented with the state transition method and no model reduction was required on the model extracted (fig. 8) for hot-bench simulation (i.e., the simulation calculations could be completed in a real-time clock frame of 0.0125 sec, which results in a timescale of 1:5). Maintenance of a timescale of 1:5, while the 1991 mathematical model was implemented, required that model reduction techniques be applied to the extracted model. After the model was reduced, the state transition model was calculated on the basis of an integration step of 0.0025 sec.

Description

The model reduction method described herein is based on transformation of a stable subspace of the full-order dynamic model to internally balanced coordinates. The following method builds on work described by Enns (1985). The major difference between the method presented herein and derivations of Enns is the calculation of the transformation matrix **T** discussed in Step 6 of this section. For more complete treatments of the properties of the singular-value decomposition, controllability, observability Gramians, and Hankel singular values, refer to Glover (1984), Enns (1985), and Bacon (1991). The following discussion outlines the steps required to implement the method with comments on the method advantages and disadvantages.

Consider the linear, time-invariant, possibly unstable systems defined by

$$\begin{Bmatrix} \dot{\mathbf{x}} \\ \mathbf{y} \end{Bmatrix} = \begin{bmatrix} \mathbf{A} & \mathbf{B} \\ \mathbf{C} & \mathbf{D} \end{bmatrix} \begin{Bmatrix} \mathbf{x} \\ \mathbf{u} \end{Bmatrix} \tag{49}$$

and referred to throughout this section by the partitioned real system matrix

$$\begin{bmatrix} \mathbf{A} & \mathbf{B} \\ \mathbf{C} & \mathbf{D} \end{bmatrix}$$

Step 1: Scale the system inputs and outputs to units of similar significance. (This step is discussed in more detail in the section entitled “Application.”)

Step 2: Transform the system of matrices in equation (49) into coordinates that decouple the stable and unstable parts of the model as follows:

$$\begin{Bmatrix} \dot{\mathbf{x}}_u \\ \dot{\mathbf{x}}_s \\ \mathbf{y} \end{Bmatrix} = \begin{bmatrix} \mathbf{A}_u & \mathbf{0} & \mathbf{B}_u \\ \mathbf{0} & \mathbf{A}_s & \mathbf{B}_s \\ \mathbf{C}_u & \mathbf{C}_s & \mathbf{D} \end{bmatrix} \begin{Bmatrix} \mathbf{x}_u \\ \mathbf{x}_s \\ \mathbf{u} \end{Bmatrix} \tag{50}$$

where the eigenvalues of $\mathbf{A}_s$ are strictly stable. The remainder of this procedure (step 6 in particular) relies on the assumption that $(\mathbf{A}_s, \mathbf{B}_s)$ is a completely controllable pair. The key issue is that the part of the model to be reduced must be controllable. If $(\mathbf{A}_s, \mathbf{B}_s)$ had uncontrollable states, they could be moved to that part of the model containing the unstable states.

Step 3: Calculate the controllability Gramian **X** and the observability Gramian **Y** of the stable subsystem by solution of the associated Lyapunov equations

$$\left.\begin{aligned} \mathbf{A}_s\mathbf{X} + \mathbf{X}\mathbf{A}_s^T + \mathbf{B}_s\mathbf{B}_s^T &= \mathbf{0} \\ \mathbf{A}_s^T\mathbf{Y} + \mathbf{Y}\mathbf{A}_s + \mathbf{C}_s^T\mathbf{C}_s &= \mathbf{0} \end{aligned}\right\} \tag{51}$$

Step 4: Perform a singular-value decomposition on the controllability Gramian

$$\mathbf{U}_x\Sigma_x\mathbf{V}_x^T = \mathbf{X} \tag{52}$$

where Σ_x is a diagonal matrix of positive real numbers and $\mathbf{U}_x$ and $\mathbf{V}_x$ are real, square, orthonormal $(\mathbf{U}_x\mathbf{U}_x^T = \mathbf{V}_x\mathbf{V}_x^T = \mathbf{I})$ matrices. Because $\mathbf{X}$ is both symmetric and positive-definite (by the controllability assumption), $\mathbf{U}_x = \mathbf{V}_x$ and decomposition equation (52) can be written as

$$\mathbf{U}_x\Sigma_x\mathbf{U}_x^T = \mathbf{X} \tag{53}$$

Because Σ_x is diagonal, $\Sigma_x^{1/2}$ refers to a diagonal matrix with diagonal elements that are the square roots of the diagonal elements of Σ_x.

Step 5: Perform a singular-value decomposition on the real symmetric, positive-semidefinite product $\mathbf{U}_x\Sigma_x^{1/2}\mathbf{U}_x^T\mathbf{Y}\mathbf{U}_x\Sigma_x^{1/2}\mathbf{U}_x^T$ to give

$$\mathbf{U}_w\Sigma_w\mathbf{U}_w^T = \mathbf{U}_x\Sigma_x^{1/2}\mathbf{U}_x^T\mathbf{Y}\mathbf{U}_x\Sigma_x^{1/2}\mathbf{U}_x^T \tag{54}$$

where Σ_w is a diagonal matrix of nonnegative real numbers ordered in decreasing magnitude.

Step 6: A transformation matrix is then formed as follows:

$$\mathbf{T} = \mathbf{U}_x\Sigma_x^{1/2}\mathbf{U}_x^T\mathbf{U}_w \tag{55}$$

If n_s is the order of the square matrix $\mathbf{A}_s$ and n_{sr} is the order of the desired reduced-order model, then the following partitioning of $\mathbf{T}$ and its inverse $\mathbf{T}^{-1}$ can be defined as

$$\left.\begin{array}{l} \begin{bmatrix}\mathbf{T}_1 & \mathbf{T}_2\end{bmatrix} = \mathbf{T} \\[1em] \begin{bmatrix}\mathbf{U}_1^T \\ \mathbf{U}_2^T\end{bmatrix} = \mathbf{T}^{-1}\end{array}\right\} \tag{56}$$

where $\mathbf{T}_1$ is $n_s \times n_{sr}$ and $\mathbf{U}_1$ is $n_s \times n_{sr}$.

Note that the transformation $\mathbf{T}$ is equivalent to the transformation formed by Enns (1985). If equation (54) is multiplied on the left by $\mathbf{U}_x\Sigma_x^{1/2}\mathbf{U}_x^T$ and on the right by $\mathbf{U}_x\Sigma_x^{1/2}\mathbf{U}_x^T$, the following result is obtained:

$$\mathbf{T}\Sigma_w\mathbf{T}^{-1} = \mathbf{XY} \tag{57}$$

Thus, the transformation that is achieved in equation (55) by singular-value decomposition is the same $\mathbf{T}$ that is achieved by an eigenvalue decomposition of the product $\mathbf{XY}$, as shown in equation (57) and as discussed by Enns (1985).

Unless $(\mathbf{A}_s, \mathbf{B}_s)$ is a completely controllable pair, the diagonal matrix $\Sigma_x^{1/2}$ will contain one or more zeros on the diagonal, which will render $\mathbf{T}$ singular. If $\mathbf{T}$ is singular, $\mathbf{T}^{-1}$ will not exist and $\mathbf{T}$ will not be a transformation matrix. Therefore, steps 4–6 require that $(\mathbf{A}_s, \mathbf{B}_s)$ be a completely controllable pair or, equivalently, that $\mathbf{X}$ be positive-definite ($\mathbf{X} > 0$), not merely positive-semidefinite.

Step 7: When the stable subsystem is transformed according to the matrix $\mathbf{T}$, the new internally balanced states are ordered in importance to the frequency response over all input and output pairs. A reduced-order model of the stable subsystem can now be formed by the following equation

$$\begin{bmatrix}\mathbf{A}_{sr} & \mathbf{B}_{sr} \\ \mathbf{C}_{sr} & \mathbf{D}_{sr}\end{bmatrix} = \begin{bmatrix}\mathbf{U}_1^T\mathbf{A}_s\mathbf{T}_1 & \mathbf{U}_1^T\mathbf{B}_s \\ \mathbf{C}_s\mathbf{T}_1 & \mathbf{D}\end{bmatrix} \tag{58}$$

Step 8: The matrix $\mathbf{A}_{sr}$ will generally be fully populated. Transformation of the reduced-order stable subsystem $\begin{bmatrix}\mathbf{A}_{sr} & \mathbf{B}_{sr} \\ \mathbf{C}_{sr} & \mathbf{D}_{sr}\end{bmatrix}$ to a real Jordan form minimizes computations required to implement the discretized form of the reduced system. The real Jordan form is diagonal up to 2×2 blocks for independent eigenvectors. The near-diagonal reduced-order stable subsystem can then be recombined with the unstable subsystem of the original dynamic system to form a reduced-order form of the original, possibly unstable, dynamic system:

$$\begin{bmatrix}\mathbf{A}_r & \mathbf{B}_r \\ \mathbf{C}_r & \mathbf{D}_r\end{bmatrix} = \begin{bmatrix}\mathbf{A}_u & \mathbf{0} & \mathbf{B}_u \\ \mathbf{0} & \mathbf{A}_{sr} & \mathbf{B}_{sr} \\ \mathbf{C}_u & \mathbf{C}_{sr} & \mathbf{D}\end{bmatrix} \tag{59}$$

Step 9: Scale the reduced system back to original units.

Numerical Robustness

Before the procedures (which have been described in the previous section) were implemented, a commercial package was invoked to provide the internally balanced representation of a stable system achieved by the transformation $\mathbf{T}$ in step 6. In the commercial package, the method to achieve an internally balanced representation was not known, but the command consistently failed and reported a problem during a Cholesky decomposition. However, this same commercial package worked well with smaller systems. The use of singular-value decompositions, well-known for their numerical stability, make the approach outlined in steps 1–9 attractive.

Error Properties

After a reduced-order model is formed, the model is evaluated to see how well it approximates the full-order model. First, a frequency response error matrix $\mathbf{E}_{sr}$ is formed with the difference between the full- and reduced-order system

$$\mathbf{E}_{sr}(j\omega) = \mathbf{C}_s(j\omega\mathbf{I} - \mathbf{A}_s)^{-1}\mathbf{B}_s - \mathbf{C}_{sr}(j\omega\mathbf{I} - \mathbf{A}_{sr})^{-1}\mathbf{B}_{sr} \tag{60}$$

Let the n_s diagonal elements of $\Sigma_w^{1/2}$ defined in equation (54) be denoted by $\sigma_h(i)$ (the Hankel singular values). (See Glover (1984).) A magnitude bound (Enns (1985) and Glover (1984)) on $\mathbf{E}_{sr}$ is given by

$$\sup\{\bar{\sigma}[\mathbf{E}_{sr}(j\omega)], \forall\ \omega\} \le \varepsilon_B = 2\sum_{i = n_{sr}+1}^{n_s} \sigma_h(i) \tag{61}$$

so that the maximum singular value of the error matrix for all frequencies is less than or equal to twice the sum of the Hankel singular values associated with the removed $n_s - n_{sr}$ states. The maximum singular value of a matrix can be interpreted as

$$\bar{\sigma}[\mathbf{E}_{sr}] = \sup\{\mathbf{E}_{sr}\mathbf{u}, \|\mathbf{u}\| = 1\}$$

Thus, the maximum magnitude response of $\mathbf{E}_{sr}$ in any direction for a harmonic input of unit size is bounded by ε_B. In particular, the magnitude of the largest element of $\mathbf{E}_{sr}(j\omega)$ is bounded by ε_B. The significance of this well-known result for internally balanced realizations cannot be overstated. After steps 1–5 are performed, the quality of the reduced-order model to be generated for any selection of n_{sr} can be determined before performing steps 6–9. Furthermore, because the stable and unstable parts have been decoupled in step 2, the result of equation (61) holds for the error matrix associated with the complete system. Thus,

$$\mathbf{E}_r(j\omega) = \mathbf{C}(j\omega\mathbf{I} - \mathbf{A})^{-1}\mathbf{B} - \mathbf{C}_r(j\omega\mathbf{I} - \mathbf{A}_r)^{-1}\mathbf{B}_r$$

Application

In the 1991 mathematical model, the 172-state aeroservoelastic component model constitutes the bulk of the required computations in the equations of motion. When the aeroservoelastic component model is written in matrix form as in equation (49), the **A**, **B**, and **C** matrices are highly populated. Even if the system were transformed to coordinates wherein matrix **A** was diagonal, full matrix multiplication operations would still be required for matrices **B** (172×10) and **C** (56×172). However, a discretized form of equation (49) for the third component model, which includes the set of 40 uncoupled equations for the antialiasing filters, takes significantly less computational time than the aeroservoelastic component model. When written in matrix form, the **A**, **B**, and **C** matrices are square and diagonal, and matrix **D** is zero. Therefore, the aeroservoelastic component model was chosen for application of the model reduction method.

To maintain the timescale of 1:5, the aeroservoelastic component model with 172 states, 10 inputs, and 56 outputs had to be reduced to a system with approximately 80 states that would accurately replicate the full-order input and output results for all 560 combinations. As depicted in figure 8, the hot-bench simulation is derived by extracting linear aeroservoelastic component models from the batch simulation that are valid for a particular dynamic pressure. To provide sufficient continuity for the hot-bench tests, linear aeroservoelastic component models were extracted and reduced for nine different dynamic pressures that ranged from 150 to 350 psf in increments of 25 psf. This process was repeated for two wind tunnel model test configurations (and by extension, for the batch simulation): the fixed-to-roll (roll brake engaged) model and the free-to-roll model.

A requirement of any reduction process is that the inputs and outputs be scaled to units of similar significance. The first 8 inputs (actuator commands) and the first 40 outputs (sensors) of the simulation correspond to analog lines on the wind tunnel model. For these inputs and outputs, a natural selection for units was volts (V). (See table I.) The two turbulence inputs were scaled so that an intensity of one standard deviation was weighted the same as 1 V. The 16 outputs representing elastic mode deflection were left unchanged.

The analog-to-digital (A/D) converters in the digital controller yield 12 bits of resolution for inputs with a range of ±10 V. If an error bound of $\varepsilon_B = 20/2^{12}$ had been satisfied, then for a harmonic signal into any input, the difference between the full-order mathematical model and the reduced mathematical model at any output would have been less than the resolution of the converters. For the timescale described earlier, error bounds tighter than $20/2^{10}$ produced models too large for the hot-bench time interval. Because the error bound represents a worst case error and differences in the last two bits of a converted signal would be small compared with electrical noise in the wind tunnel and inaccuracies in the mathematical model, an error bound of $\varepsilon_B = 20/2^{10}$ was used. This choice of an error bound was validated by time history comparisons between the batch and the resulting hot-bench simulation. When an error bound was determined, the order of the trial reduced model n_{sr} was varied until the required accuracy was achieved according to the definition of equation (61). This approach ensured that the reduced-order aeroservoelastic component model would retain 10 of the 12 bits of precision available through the A/D converters. For each reduced-order model formed at 9 dynamic pressures, no more than 82 states were required. The 82-state model was required at the highest dynamic pressure of 350 psf, where the unstable part of the total dynamic system described in equation (49) was larger than for the lower dynamic pressures because of the formation of a second flutter mode.

Step 2 was implemented by transformation of equation (49) to real-Jordan form. For the dynamic systems considered, the eigenvectors were independent and resulted in real-Jordan forms wherein all nonzero elements of the transformed **A** matrix are either real 1×1 ($[\sigma]$) or real 2×2 $\begin{bmatrix} \sigma & \omega \\ -\omega & \sigma \end{bmatrix}$ blocks on the diagonal. The 2×2 blocks correspond to system eigenvalues that are complex conjugate pairs with σ the real part and ω the imaginary part. Corresponding rows and columns of the resulting system matrix can then be permuted if care is taken to preserve the integrity of the complex conjugate pairs until all the blocks that correspond to unstable eigenvalues ($\sigma \geq 0$) are in the upper left corner of the system matrix. The result is a system of the form wherein the eigenvalues of $\mathbf{A}_s$ are strictly stable (i.e., $\sigma < 0$).

Results of Reduction

The state dimension of the aeroservoelastic component model of the 1991 full-order mathematical simulation model was reduced from 172 states to 82 states or less at each of the 9 dynamic pressure operating points while accuracy was preserved for all combinations of 10 inputs and 56 outputs. Frequency response comparisons between the full-order (172-state) linear aeroservoelastic component model and a reduced-order form for selected input and output combinations are shown in figures 18–20. Figure 21 is a time response comparison. The responses for figures 18–21 are for the free-to-roll-simulated wind tunnel model at a dynamic pressure of 300 psf. Whereas 82 states were required to meet an error bound goal of $\varepsilon_B \leq 20/2^{10}$ at 350 psf, 79 states were sufficient for 300 psf shown in figures 18–21. This dynamic pressure is well past the predicted instability and ensures that the part of the reduction method that preserves the unstable dynamics is demonstrated.

Figure 18 shows comparisons of full- and reduced-order models for the transfer function consisting of the right wingtip accelerometer response to the right trailing-edge actuator command. The response of the 79-state model ($\varepsilon_B = 20/2^{10}$) is indistinguishable from the full-order model response for the frequency range shown. Responses for the 57-state ($\varepsilon_B = 20/2^3$) and 55-state ($\varepsilon_B = 20/2^2$) models are also shown. For the input-output pair shown in figure 18, the reduction process must be applied fairly aggressively before the reduced-model response departs from the full-order model. The property of a reduction method based on internally balanced decomposition to match peak frequency response is clearly demonstrated.

Figure 19 shows the response of the same right wingtip accelerometer to a symmetric turbulence input. At first glance, the response shown in figure 18 appears to be better fitted by the 79-state model than by the response shown in figure 19 because the peak response in figure 18 is 20 dB higher than the peak response in figure 19. The 79-state model response is indistinguishable from that of the full-order model to −40 dB in both figures 18 and 19.

Figure 20 shows the frequency response and figure 21 shows the time responses of the LLEO control position after a unit impulse command at the RTEO actuator. The magnitude response of the full-order (172-state) linear aeroservoelastic component model is shown by the heavy solid line in figure 20 and should be interpreted as zero. Actuator interaction for separate control surfaces is modeled only to the extent that calculated hinge moments affect applied rate limits. Thus, in the linear aeroservoelastic component model, no crossfeed occurs between actuators; activity of one actuator does not induce activity of another actuator. The plotting software used to create figure 20 arbitrarily plots a zero-frequency response as −100 dB magnitude and 0° phase. The true zero response is seen more clearly in the time response in figure 21. The model reduction process allows responses that are identically zero in the full-order 172-state model to become nonzero in the reduced models.

Figure 22 is a plot of the error bound ε_B of equation (61) versus number of states retained n_{sr} of equation (56). The error goes to zero when $n_{sr} = 170$ states, which is the size of the stable component of the aeroservoelastic component model at a dynamic pressure of 300 psf.

Also of interest is the end-to-end time response comparison between the complete batch simulation and the complete hot-bench simulation model after a commanded control deflection in volts. The end-to-end comparison includes the effects of the antialiasing filter dynamics and nonlinear actuator dynamics that were not reduced. Responses of both batch and hot-bench simulations were calculated for a step command of 1 V (2.67°)

to the RTEO actuator for the free-to-roll condition at a dynamic pressure of 225 psf. The time response agreement was uniformly excellent for all outputs. The right and left wingtip accelerometer responses, which are typical cases, are shown in figure 23. In each case, batch (full-order mathematical model) and hot-bench simulation responses for the 1991 mathematical model are plotted versus the left vertical axis and cannot be distinguished. The difference between the batch and hot-bench result is plotted versus the right vertical axis. The scale on the right axis is 0.01 of the scale on the left axis. In each case, the differences are in millivolts and generally peak where the batch response changes rapidly.

More advanced model reduction techniques use frequency-weighting filters to discount selected frequency regions of the full-order model. (See Enns (1985) and Bacon (1991).) In a frequency-weighting approach, weighting filters would be applied either to all the input signals or to all the output signals. Whereas lower order final models can be achieved by bounding the frequency range of interest, the application of frequency weighting raises three concerns. Foremost is the absence of a guaranteed bound of the form of equation (61). The presence of this bound for the internally balanced method obviates the need for extensive checks on all possible input and output combinations in the reduced models. However, work on the formulation of such a bound in conjunction with frequency weighting has been reported by Newman and Schmidt (1991). A second concern is that the addition of weighting filters imposes a burden on computational and numerical robustness by effectively raising the order of the full-order plant to be reduced. Solution of the Lyapunov equation (51) for a symmetric controllability Gramian $\mathbf{X}$ of dimension 100×100 is analogous to the solution of a linear system of equations for $5050 = (101)(100)/2$ unknowns. An increase in the order of $\mathbf{X}$ by 10 raises the order of the associated Lyapunov solution from 5050 to 6105. The third issue concerns time responses. Because the internally balanced approach ensures a good match in peak frequency response for the entire frequency range, equivalent responses in both the frequency and time domains between the full- and reduced-order models are ensured for arbitrary input. If a reduced-order plant is produced by deemphasizing selected frequency components, a step input, which has broadband frequency content, would produce a different time response from that of the full-order model. Band-limited inputs are required to produce matching time histories. This property should not be a concern as long as it is anticipated and understood.

The classical internally balanced approach in combination with the numerically robust method of calculation presented herein and the system scaling chosen were well suited to the problem of reducing an aeroservoelastic simulation model. The simulation model had to give results indistinguishable from the batch simulation to support digital controller validation. The great number of states, inputs, and outputs would have made the application of frequency-weighted methods difficult and, for the required target model size, unnecessary.

Concluding Remarks

A method has been developed for simulation of aeroservoelastic systems that is amenable to both batch and real-time applications. A complete set of equations was presented as were theoretical justifications for the implementation equations used in the Dryden turbulence formulation and for the state transition mechanization. The state transition mechanization was based on a trapezoidal data reconstruction scheme. The inclusion of fully nonlinear rigid-body degrees of freedom (with the exception of the roll degree of freedom, which was treated as an elastic mode) was not required for this application but is addressed in other references, notably Cutchins et al. (1983), Buttrill et al. (1987), Morino and Baillieul (1987), and Waszak and Schmidt (1988).

Methods were described for constructing the active flexible wing aeroservoelastic models from finite-element structural models, linear unsteady aerodynamic theory, and actuator transfer function characterization. Consistent with current industrial practice, linear methods were used to develop the unsteady aerodynamic mathematical models. The requirement that a great number of design mathematical models be developed for various boundary conditions precluded extensive use of nonlinear computational fluid dynamic codes.

The dynamic pressure at which flutter would occur was generally predicted to within 6 percent by these methods. However, all predicted dynamic pressures were higher than the measured values which made the resulting errors nonconservative from the perspective of locating the flutter stability boundary in the flight envelope. Conservative errors would have been preferred. In addition, the error in the predicted flutter frequency is higher than the dynamic pressure error—13 percent for antisymmetric flutter and 16 percent for symmetric flutter. The prediction of transfer function representations between specific input-output pairs relies on accurate characterization of elastic mode shapes and is more difficult than predictions of such global flutter parameters as dynamic pressure and frequency. Before active flutter suppression can become an accepted design practice, the ability, from an input-output perspective, to model flutter needs improvement in the critical frequency range. Conversely, the control designer is challenged to ensure that control laws are robust to known or probable errors in plant characterization.

Modern model reduction techniques substantially reduced the computing time required to simulate the aeroservoelastic system. The model reduction method was based on transformation of a stable subsystem to internally balanced coordinates, an approach that was particularly effective at removing the aerodynamic lag states that are often part of linear aeroservoelastic systems.

Because the internally balanced approach produces a good match for the entire frequency range, equivalent responses in both frequency and time domains are ensured for the full- and reduced-order models. The equivalent time and frequency responses significantly simplified the hot-bench validation process. Because simulation practitioners are most often concerned with time responses, agreement in the time domain is essential for widespread simulation application.

Finally, the error bound properties of the internally balanced decomposition greatly enhance its usefulness in model reduction. A particular advantage is that extensive checks of all possible input and output combinations in the reduced models are not required. However, numerical conditioning can become an issue when internally balanced decompositions of large aeroservoelastic systems are performed, and caution is recommended.

NASA Langley Research Center
Hampton, VA 23681-0001
August 18, 1995

Appendix A

Derivation of Turbulence-Modeling Identities

The identity of

$$\sigma^2 = \int_0^\infty \Phi(\Omega)\, d\Omega \qquad \text{(A1)}$$

is demonstrated for both Φ_u and Φ_w. The longitudinal power spectral density (psd) is given by

$$\Phi_u(\Omega) = \sigma^2 \frac{2L}{\pi} \frac{1}{(1 + L^2\Omega^2)} \qquad \text{(A2)}$$

If the following change of variables is applied to equation (A2) while the identity is preserved in equation (A1), then

$$\left.\begin{aligned} x &= L\Omega \\ d\Omega &= L^{-1} dx \end{aligned}\right\} \qquad \text{(A3)}$$

and a new gust psd in x is obtained that satisfies equation (A1), if and only if equation (A2) satisfies equation (A1), such that

$$\hat{\Phi}_u(x) = \sigma^2 \frac{2}{\pi} \frac{1}{(1 + x^2)} \qquad \text{(A4)}$$

The use of standard antiderivative tables provides the desired result. That is,

$$\begin{aligned} \int_0^\infty \hat{\Phi}_u(x)\, dx &= \sigma^2 \frac{2}{\pi} \int_0^\infty \frac{dx}{(1 + x^2)} = \sigma^2 \frac{2}{\pi} \arctan x \Big|_0^\infty \\ &= \sigma^2 \frac{2}{\pi} \left(\frac{\pi}{2} - 0 \right) = \sigma^2 \end{aligned} \qquad \text{(A5)}$$

The one-sided Dryden vertical (and lateral) gust velocity psd Φ_w is given by

$$\Phi_w(\Omega) = \frac{\sigma^2 L}{\pi} \frac{(1 + 3L^2\Omega^2)}{(1 + L^2\Omega^2)^2} \qquad \text{(A6)}$$

Application of the same change of variables as indicated in equation (A3) gives

$$\hat{\Phi}_w(x) = \frac{\sigma^2}{\pi} \frac{(1 + 3x^2)}{(1 + x^2)^2} \qquad \text{(A7)}$$

The combination of equations (A1) and (A7) with the results in standard antiderivative tables yields

$$\begin{aligned} \int_0^\infty \hat{\Phi}_w(x)\, dx &= \sigma^2 \frac{1}{\pi} \int_0^\infty \frac{(1 + 3x^2)}{(1 + x^2)^2}\, dx \\ &= \sigma^2 \frac{1}{\pi} \frac{-x}{(1 + x^2)} \Bigg|_0^\infty + 2\int_0^\infty \frac{dx}{(1 + x^2)} \end{aligned} \qquad \text{(A8)}$$

From the result shown previously in equation (A5),

$$\begin{aligned} \int_0^\infty \hat{\Phi}_w(x)\, dx &= \sigma^2 \frac{1}{\pi} \left(0 + 2\int_0^\infty \frac{dx}{(1 + x^2)} \right) \\ &= \sigma^2 \frac{2}{\pi} \int_0^\infty \frac{dx}{(1 + x^2)} = \sigma^2 \end{aligned} \qquad \text{(A9)}$$

Appendix B

Explanation of Constant Power Assumption

Tatom and Smith (1982) assert that digital simulation commonly requires that S_υ have unit power when integrated in the Nyquist frequency interval $(-\pi/T_\upsilon, \pi/T_\upsilon)$. This property can be assured by assuming that ideally υ will have zero power outside the Nyquist frequency interval and within the Nyquist interval $S_\upsilon = T_\upsilon/2\pi$. As indicated by Tatom and Smith (1982), the actual power spectrum of a Gaussian random number when sampled and held does not have the ideal boxcar shape but rather is given by

$$S_\upsilon = \frac{1}{\omega_s}\sin^2\frac{(\omega\pi/\omega_s)}{(\omega\pi/\omega_s)^2}$$

where ω_s is the sampling frequency. A comparison of the actual spectrum and ideal spectrum is shown in figure B1. The actual spectrum reveals reduction of power as the sampling frequency is approached due to the actions of sampling and holding. Tatom and Smith (1982, pp. 2–14) go on to show the following:

> Thus for white noise, *the aliasing due to discrete sampling exactly offsets the tapering due to discrete generation when the sampling frequency equals the generation frequency*. On the basis of this fundamental point, the simulation of white noise clearly shows no tapering of the spectrum as long as the sampling rate equals the generation rate. Under most conditions this equality is automatically satisfied.

Heuristically, the areas under the curves in figure B1 are approximately equal. Although a more complete explanation would be intellectually satisfying, that explanation is beyond the scope of this report. The implementation formulation developed for and used in the AFW simulation was, in the final analysis, one that gave the desired rms results.

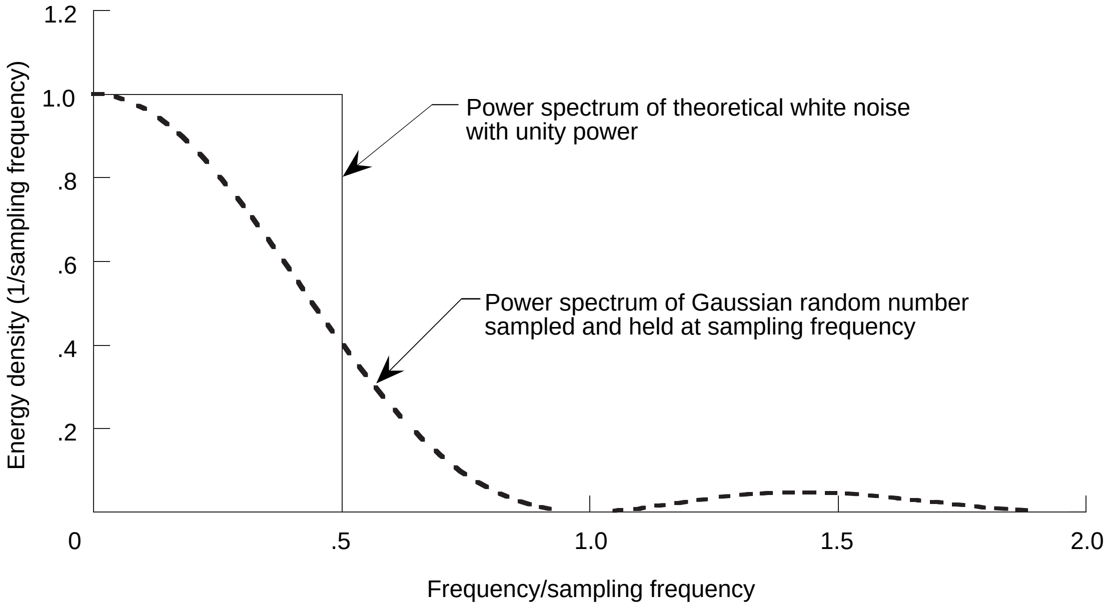

Figure B1. Two-sided power spectrum for theoretical white noise (with zero power outside Nyquist frequency) compared with Gaussian random number that is sampled and held. (Adapted from fig. 2-2 of Tatom and Smith (1982).)

Appendix C

Derivation of State Transition Equations

For convenience, we repeat equations (32)–(37) as part of this appendix to derive state transition equations (34)–(37). Given the linear matrix differential equation (32) from the text

$$\dot{\mathbf{x}} = \mathbf{A}\mathbf{x} + \mathbf{B}\mathbf{u} \tag{C1}$$

which involves appropriately dimensioned vectors **u** and **x**, and if the ramp input signal (from eq. (33))

$$\mathbf{u}(t) = \mathbf{u}_k + \frac{(t-kh)\,(\mathbf{u}_{k+1}-\mathbf{u}_k)}{h} \tag{C2}$$

is defined in the interval $kh \le t < (k+1)h$, then the following exact solution for **x** at time $t = (k+1)h$ exists:

$$\mathbf{x}_{k+1} = \mathbf{F}_k\mathbf{x}_k + \mathbf{G}_k^{\text{trap}}\mathbf{u}_k + \mathbf{G}_{k+1}^{\text{trap}}\mathbf{u}_{k+1} \tag{C3}$$

where from equations (35)–(37)

$$\mathbf{F}_k = e^{\mathbf{A}h} \tag{C4}$$

$$\mathbf{G}_k^{\text{trap}} = \left(-e^{\mathbf{A}h} + e^{\mathbf{A}h}\mathbf{A}^{-1}h^{-1} - \mathbf{A}^{-1}h^{-1}\right)\left(-\mathbf{A}^{-1}\mathbf{B}\right) \tag{C5}$$

$$\mathbf{G}_{k+1}^{\text{trap}} = \left(\mathbf{I} - e^{\mathbf{A}h}\mathbf{A}^{-1}h^{-1} + \mathbf{A}^{-1}h^{-1}\right)\left(-\mathbf{A}^{-1}\mathbf{B}\right) \tag{C6}$$

Proof: Observe that in the interval

$$\mathbf{u}(t) = \mathbf{u}_k + (t-kh)\,\dot{\mathbf{u}}_k \tag{C7}$$

where

$$\dot{\mathbf{u}}_k = \frac{\mathbf{u}_{k+1}-\mathbf{u}_k}{h} \tag{C8}$$

The general solution to the first-order differential equation (32) is as follows:

$$\dot{\mathbf{x}} = \mathbf{A}\mathbf{x} + \mathbf{B}\mathbf{u} \tag{C9}$$

in the time interval $kh \le t \le (k+1)h$ can be found with an integrating factor. First, move all **x** terms to the left and left multiply the equation by the integrating factor $e^{-\mathbf{A}t}$ to obtain

$$e^{-\mathbf{A}t}(\dot{\mathbf{x}} - \mathbf{A}\mathbf{x}) = e^{-\mathbf{A}t}\mathbf{B}\mathbf{u} \tag{C10}$$

The observation that

$$\frac{d}{dt}\left(e^{-\mathbf{A}t}\mathbf{x}\right) = e^{-\mathbf{A}t}(\dot{\mathbf{x}} - \mathbf{A}\mathbf{x})$$

and with integration of both sides of equation (C10) in the time interval $kh \le t \le (k+1)h$

$$\left[e^{-\mathbf{A}t}\mathbf{x}(t)\right]\Big|_{kh}^{(k+1)h} = \int_{kh}^{(k+1)h} e^{-\mathbf{A}t}\mathbf{B}\mathbf{u}(t)\,dt \tag{C11}$$

$$\begin{aligned} e^{-\mathbf{A}(k+1)h}\mathbf{x}_{k+1} - e^{-\mathbf{A}(k)h}\mathbf{x}_k = \int_{kh}^{(k+1)h} e^{-\mathbf{A}t} \\ \times\mathbf{B}\left[\mathbf{u}_k + (t-kh)\,\dot{\mathbf{u}}_k\right]dt \end{aligned} \tag{C12}$$

$$\begin{aligned} e^{-\mathbf{A}kh}\left(e^{-\mathbf{A}h}\mathbf{x}_{k+1} - \mathbf{x}_k\right) = \int_{kh}^{(k+1)h} e^{-\mathbf{A}t} \\ \times\mathbf{B}\left[\mathbf{u}_k + (t-kh)\,\dot{\mathbf{u}}_k\right]dt \end{aligned} \tag{C13}$$

The following variable change is used to rewrite the integral in equation (C13):

$$\left.\begin{aligned} \tau &= t - kh \\ t &= \tau + kh \end{aligned}\right\} \tag{C14}$$

which gives

$$\begin{aligned} e^{-\mathbf{A}kh}\left(e^{-\mathbf{A}h}\mathbf{x}_{k+1} - \mathbf{x}_k\right) = \int_0^h e^{-\mathbf{A}(\tau+kh)} \\ \times\mathbf{B}\left(\mathbf{u}_k + (\tau)\,\dot{\mathbf{u}}_k\right)d\tau \end{aligned} \tag{C15}$$

and is equivalent to

$$\begin{aligned} e^{-\mathbf{A}kh}\left(e^{-\mathbf{A}h}\mathbf{x}_{k+1} - \mathbf{x}_k\right) = e^{-\mathbf{A}kh}\left(\int_0^h e^{-\mathbf{A}\tau}d\tau\right)\mathbf{B}\mathbf{u}_k \\ + e^{-\mathbf{A}kh}\left(\int_0^h e^{-\mathbf{A}\tau}\tau\,d\tau\right)\mathbf{B}\dot{\mathbf{u}}_k \end{aligned} \tag{C16}$$

Removal of the common factor of $e^{-\mathbf{A}kh}$ from equation (C16) yields

$$\begin{aligned} e^{-\mathbf{A}h}\mathbf{x}_{k+1} - \mathbf{x}_k = \left(\int_0^h e^{-\mathbf{A}\tau}d\tau\right)\mathbf{B}\mathbf{u}_k \\ + \left(\int_0^h e^{-\mathbf{A}\tau}\tau\,d\tau\right)\mathbf{B}\dot{\mathbf{u}}_k \end{aligned} \tag{C17}$$

The integral expressions in equation (C17) can be expanded as

$$\begin{aligned}\int_0^h e^{-\mathbf{A}\tau} d\tau &= \left(-e^{-\mathbf{A}\tau}\mathbf{A}^{-1}\right)\Big|_0^h \\ &= \left(-e^{-\mathbf{A}h} + e^{-\mathbf{A}0}\right)\mathbf{A}^{-1} \\ &= \left(\mathbf{I} - e^{-\mathbf{A}h}\right)\mathbf{A}^{-1} \end{aligned} \qquad \text{(C18)}$$

and

$$\begin{aligned}\int_0^h \left(e^{-\mathbf{A}\tau}\tau\right) d\tau &= \left(-\tau e^{-\mathbf{A}\tau}\mathbf{A}^{-1}\right)\Big|_0^h - \int_0^h -e^{-\mathbf{A}\tau}\mathbf{A}^{-1} d\tau \\ &= \left(-he^{-\mathbf{A}h} + 0\right)\mathbf{A}^{-1} + \left(\int_0^h e^{-\mathbf{A}\tau} d\tau\right)\mathbf{A}^{-1} \\ &= -he^{-\mathbf{A}h}\mathbf{A}^{-1} + \left(\mathbf{I} - e^{-\mathbf{A}h}\right)\mathbf{A}^{-2} \end{aligned} \qquad \text{(C19)}$$

The combination of equations (C17)–(C19) gives

$$\begin{aligned} e^{-\mathbf{A}h}\mathbf{x}_{k+1} - \mathbf{x}_k &= \left(\mathbf{I} - e^{-\mathbf{A}h}\right)\mathbf{A}^{-1}\mathbf{B}\mathbf{u}_k \\ &\quad + \left[-he^{-\mathbf{A}h}\mathbf{A}^{-1} + \left(\mathbf{I} - e^{-\mathbf{A}h}\right)\mathbf{A}^{-2}\right]\mathbf{B}\dot{\mathbf{u}}_k \end{aligned} \qquad \text{(C20)}$$

The combination of equations (C8) and (C20) gives

$$\begin{aligned} e^{-\mathbf{A}h}\mathbf{x}_{k+1} - \mathbf{x}_k &= \left(\mathbf{I} - e^{-\mathbf{A}h}\right)\mathbf{A}^{-1}\mathbf{B}\mathbf{u}_k \\ &\quad + \left[-he^{-\mathbf{A}h}\mathbf{A}^{-1} + \left(\mathbf{I} - e^{-\mathbf{A}h}\right)\mathbf{A}^{-2}\right] \\ &\quad \times \mathbf{B}\,(\mathbf{u}_{k+1} - \mathbf{u}_k)\, h^{-1} \\ &= \left(\mathbf{I} - e^{-\mathbf{A}h}\right)\mathbf{A}^{-1}\mathbf{B}\mathbf{u}_k \\ &\quad + \left(-e^{-\mathbf{A}h} + h^{-1}\mathbf{A}^{-1} - e^{-\mathbf{A}h}h^{-1}\mathbf{A}^{-1}\right) \\ &\quad \times \mathbf{A}^{-1}\mathbf{B}\,(\mathbf{u}_{k+1} - \mathbf{u}_k) \\ &= \left(\mathbf{I} - e^{-\mathbf{A}h} + e^{-\mathbf{A}h} - h^{-1}\mathbf{A}^{-1} + e^{-\mathbf{A}h}h^{-1}\mathbf{A}^{-1}\right) \\ &\quad \times \mathbf{A}^{-1}\mathbf{B}\mathbf{u}_k + \left(-e^{-\mathbf{A}h} + h^{-1}\mathbf{A}^{-1} - e^{-\mathbf{A}h}h^{-1}\mathbf{A}^{-1}\right) \\ &\quad \times \mathbf{A}^{-1}\mathbf{B}\mathbf{u}_{k+1} \\ &= \left(\mathbf{I} - \mathbf{A}^{-1}h^{-1} + e^{-\mathbf{A}h}\mathbf{A}^{-1}h^{-1}\right) \\ &\quad \times \mathbf{A}^{-1}\mathbf{B}\mathbf{u}_k + \left(-e^{-\mathbf{A}h} + \mathbf{A}^{-1}h^{-1} - e^{-\mathbf{A}h}\mathbf{A}^{-1}h^{-1}\right) \\ &\quad \times \mathbf{A}^{-1}\mathbf{B}\mathbf{u}_{k+1} \end{aligned} \qquad \text{(C21)}$$

Multiplication of equation (C14) by $e^{\mathbf{A}h}\mathbf{x}$ gives

$$\begin{aligned} \mathbf{x}_{k+1} &= e^{\mathbf{A}h}\mathbf{x}_k + \left(-e^{\mathbf{A}h} + e^{\mathbf{A}h}\mathbf{A}^{-1}h^{-1} - \mathbf{A}^{-1}h^{-1}\right)\left(-\mathbf{A}^{-1}\mathbf{B}\right)\mathbf{u}_k \\ &\quad + \left(\mathbf{I} - e^{\mathbf{A}h}\mathbf{A}^{-1}h^{-1} + \mathbf{A}^{-1}h^{-1}\right)\left(-\mathbf{A}^{-1}\mathbf{B}\right)\mathbf{u}_{k+1} \end{aligned}$$

References

Adams, William M., Jr.; Christhilf, David M.; Waszak, Martin R.; Mukhopadhyay, Vivek; and Srinathkumar, S. 1992: *Design, Test, and Evaluation of Three Active Flutter Suppression Controllers*. NASA TM-4338.

Adams, William M., Jr.; and Hoadley, Sherwood Tiffany 1993: *ISAC: A Tool for Aeroservoelastic Modeling and Analysis*. NASA TM-109031.

Airworthiness Standards 1992: Transport Category Airplanes. FAR Pt. 25, FAA.

Arbuckle, P. Douglas; Buttrill, Carey S.; and Zeiler, Thomas A. 1989: Simulation Model-Building Procedure for Dynamic Systems Integration. *J. Guid., Control, & Dyn.*, vol. 12, pp. 894–900.

Bacon, Barton Jon 1991: Order Reduction for Closed-Loop Systems. Ph.D Thesis, Univer. of Purdue.

Buttrill, Carey S.; Arbuckle, P. Douglas; Zeiler, Thomas A. 1987: Nonlinear Simulation of Flexible Aircraft in Maneuvering Flight. *Technical Papers—AIAA Flight Simulation Technologies Conference*, AIAA, pp. 122–133. (Available as AIAA-87-2501.)

Buttrill, Carey S.; and Bacon, Barton J. 1991: Model Order Reduction Applied to a Hot-Bench Simulation of an Aeroelastic Wind-Tunnel Model. *Technical Papers—AIAA Flight Simulation Technologies Conference*, AIAA, pp. 185–195. (Available as AIAA-91-2935.)

Buttrill, Carey; Bacon, Barton; Heeg, Jennifer; Houck, Jacob; and Wood, David 1992: Simulation and Model Reduction for the AFW Program. *Technical Papers—AIAA Dynamics Specialist Conference*, pp. 11–19. (Available as AIAA-92-2081.)

Buttrill, Carey S.; and Houck, Jacob A. 1990: Hot-Bench Simulation of the Active Flexible Wing Wind-Tunnel Model. *Technical Papers—AIAA Flight Simulation Technologies Conference and Exhibit*, pp. 11–21. (Available as AIAA-90-3121.)

Christhilf, David M.; and Adams, William M., Jr. 1992: Multifunction Tests of a Frequency Domain Based Flutter Suppression System. *Technical Papers—AIAA Dynamics Specialist Conference*, pp. 146–155. (Available as AIAA-92-2096.)

Crawford, D. J.; and Cleveland, J. I., II 1986: The New Langley Research Center Advanced Real-Time Simulation (ARTS) System. AIAA-86-2680.

Cutchins, M. A.; Purvis, J. W.; and Bunton, R. W. 1983: Aerosevoelasticity in the Time Domain—For YF-16 Aircraft. *J. Aircr.*, vol. 20, pp. 753–761.

Douglas Aircraft Co. 1975: *Technology Application Studies for Supersonic Cruise Aircraft—Volume I*. NASA CR-144925.

Enns, D. F. 1985: Model Reduction for Control System Design. NASA CR-170417.

Garrick, I. E.; and Reed, Wilmer H., III 1981: Historical Development of Aircraft Flutter. *J. Aircr.*, vol. 18, no. 11, pp. 897–912.

Giesing, J. P.; Kalman, T. P.; and Rodden, W. P. 1971: *Subsonic Unsteady Aerodynamics for General Configurations. Part I, Volume I—Direct Application of the Nonplanar Doublet-Lattice Method*. AFFDL-TR-71-5, Pt. I, Vol. I, U.S. Air Force. (Available from DTIC as AD 891 403L.)

Glover, Keith 1984: All Optimal Hankel-Norm Approximations of Linear Multivariable Systems and Their L_∞-Error Bounds. *Int. J. Control*, vol. 39, no. 6, pp. 1115–1193.

Hardin, Jay C. 1986: *Introduction to Time Series Analysis*. NASA RP-1145.

Hoadley, Sherwood T.; and McGraw, Sandra M. 1992: The Multiple-Function Multi-Input/Multi-Output Digital Controller System for the AFW Wind Tunnel Model. *Technical Papers—AIAA Dynamics Specialist Conference*, pp. 30–38. (Available as AIAA-92-2083.)

Hoblit, Frederic M. 1988: *Gust Loads on Aircraft: Concepts and Applications*. AIAA.

Karpel, Mordechay 1981: *Design for Active and Passive Flutter Suppression and Gust Alleviation*. NASA CR-3482.

Klepl, M. J. 1992: A Flutter Suppression System Using Strain Gages Applied to Active Flexible Wing Technology: Design and Test. *Technical Papers—AIAA Dynamics Specialist Conference*, pp. 162–171. (Available as AIAA-92-2098.)

Miller, Gerald D. 1988: *Active Flexible Wing (AFW) Technology*. AFWAL-TR-87-3096, U.S. Air Force. (Available from DTIC as AD B131 204.)

Military Specification—Airplane Strength and Rigidity Vibration, Flutter, and Divergence. MIL-A-8870B(AS), May 20, 1987.

Military Standard—Flying Qualities of Piloted Aircraft. MIL-STD-1797A, Jan. 30, 1990. (Supersedes MIL-STD-1797(USAF).)

Moore, Bruce C. 1981: Principal Component Analysis in Linear Systems: Controllability, Observability, and Model Reduction. *IEEE Trans. Autom. Control*, vol. AC-26, no. 1, pp. 17–32.

Moore, Doug 1992: Maneuver Load Control Using Optimized Feedforward Commands. *Technical Papers—AIAA Dynamics Specialist Conference*, pp. 181–187. (Available as AIAA-92-2100.)

Morino, L.; and Baillieul, J. 1987: A Geometrically-Exact Non-Linear Lagrangian Formulation for the Dynamic Analysis of a Flexible Maneuvering Airplane. CCAD-TR-87-02, U.S. Air Force.

Mukhopadhyay, Vivek 1992: Flutter Suppression Digital Control Law Design and Testing for the AFW Wind-Tunnel Model. *Technical Papers—AIAA Dynamics Specialist Conference*, pp. 156–161. (Available as AIAA-92-2095.)

Newman, B.; and Schmidt, D. 1991: New Plant and Controller Order Reduction Results With Weighted Balancing. *Technical Papers—AIAA Guidance, Navigation, and Control Conference*, pp. 1717–1727. (Available as AIAA-91-2805.)

Noll, Thomas E.; Perry, Boyd, III; Tiffany, Sherwood H.; Cole, Stanley R.; Buttrill, Carey S.; Adams, William M., Jr.; Houck, Jacob A.; Srinathkumar, S.; Mukhopadhyay, Vivek; Pototzky, Anthony S.; Heeg, Jennifer; McGraw, Sandra M.; Miller, Gerald; Ryan, Rosemary; Brosnan, Michael; Haverty, James; and Klepl, Martin 1989: *Aeroservoelastic Wind-Tunnel Investigations Using the Active Flexible Wing Model—Status and Recent Accomplishments*. NASA TM-101570.

Peele, Ellwood L.; and Adams, William M., Jr. 1979: *A Digital Program for Calculating the Interaction Between Flexible Structures, Unsteady Aerodynamics and Active Controls*. NASA TM-80040.

Perry, Boyd, III; Cole, Stanley R.; and Miller, Gerald D. 1992: A Summary of the Active Flexible Wing Program. *Technical Papers—AIAA Dynamics Specialist Conference,* pp. 1–10. (Available as AIAA-92-2080.)

Perry, Boyd, III; Mukhopadhyay, Vivek; Hoadley, Sherwood Tiffany; Cole, Stanley R.; and Buttrill, Carey S. 1990: Digital-Flutter-Suppression-System Investigations for the Active Flexible Wing Wind-Tunnel Model. *Technical Papers—AIAA/ASME/ASCE/AHIS/ASC 31st Structures, Structural Dynamics and Materials Conference,* Part 3, pp. 1571–1581. (Available as AIAA-90-1074.)

Pototzky, Anthony S.; Wieseman, Carol; Hoadley, Sherwood Tiffany; and Mukhopadhyay, Vivek 1990: Development and Testing of Methodology for Evaluating the Performance of Multi-Input/Multi-Output Digital Control Systems. *Technical Papers—AIAA Guidance, Navigation, and Control Conference*, Part 2, pp. 1673–1782. (Available as AIAA-90-3501.)

Ray, J. K.; Carlin, C. M.; and Lambregts, A. A. 1992: *High-Speed Civil Transport Flight- and Propulsion-Control Technological Issues*. NASA CR-186015.

Roskam, Jan 1979: *Airplane Flight Dynamics and Automatic Flight Controls.* Roskam Aviation and Engineering Corp. Part I: Chapters 1 Through 6—Rigid Airplane Flight Dynamics (Open-Loop). Part II: Rigid and Elastic Airplane Flight Dynamics and Automatic Flight Controls.

Silva, Walter A.; and Bennett, Robert M. 1992: Further Investigations of the Aeroelastic Behavior of the AFW Wind-Tunnel Model Using Transonic Small Disturbance Theory. *Technical Papers—AIAA Dynamics Specialist Conference*, pp. 20–29. (Available as AIAA-92-2082.)

Stevens, Brian L.; and Lewis, Frank L. 1992: *Aircraft Control and Simulation*. John Wiley & Sons.

Tatom, Frank B.; and Smith, S. Ray 1982: *Advanced Space Shuttle Simulation Model*. NASA CR-3541.

Taylor, Lawrence W., Jr., compiler 1991: *4th NASA Workshop on Computational Control of Flexible Aerospace Systems*. NASA CP-10065.

Thompson, Glenn O.; and Kass, Gerald J. 1972: Active Flutter Suppression—An Emerging Technology. *J. Aircr*., vol. 9, no. 3, pp. 230–235.

Tiffany, Sherwood H.; and Adams, William M., Jr. 1988: *Nonlinear Programming Extensions to Rational Function Approximation Methods for Unsteady Aerodynamic Forces*. NASA TP-2776.

Tiffany, Sherwood H.; and Karpel, Mordechay 1989: *Aeroservoelastic Modeling and Applications Using Minimum-State Approximations of the Unsteady Aerodynamics*. NASA TM-101574.

Waszak, Martin R.; Davidson, John B.; and Schmidt, David K. 1987: *A Simulation Study of the Flight Dynamics of Elastic Aircraft.* NASA CR-4102.

Volume One—Experiment, Results and Analysis.

Volume Two—Data.

Waszak, Martin R.; and Schmidt, David K. 1988: Flight Dynamics of Aeroelastic Vehicles. *J. Aircr*., vol. 25, pp. 563–571.

Waszak, M. R.; and Srinathkumar, S. 1992: Flutter Suppression for the Active Flexible Wing: Control System Design and Experimental Validation. *Technical Papers—AIAA Dynamics Specialist Conference*, pp. 138–145. (Available as AIAA-92-2097.)

Wieseman, Carol D.; Hoadley, Sherwood T.; and McGraw, Sandra M. 1992: On-Line Analysis Capabilities Developed To Support the AFW Wind-Tunnel Tests. *Technical Papers—AIAA Dynamics Specialist Conference*, pp. 39–47. (Available as AIAA-92-2084.)

Woods-Vedeler, Jessica A.; and Pototzky, Anthony S. 1992: Rolling Maneuver Load Alleviation Using Active Controls. *Technical Papers—AIAA Dynamics Specialist Conference*, pp. 172–180. (Available as AIAA-92-2099.)

Table I. Model Signal Description and Scale Selection

No.	Signal	Positive direction	Engineering unit	Scale, V/EU
Input signals				
1	LLEO actuator command	LE down	deg streamwise	0.375
2	LLEI actuator command	↓	↓	↓
3	RLEI actuator command	↓	↓	↓
4	RLEO actuator command	↓	↓	↓
5	LTEO actuator command	TE down	↓	↓
6	LTEI actuator command	↓	↓	↓
7	RTEI actuator command	↓	↓	↓
8	RTEO actuator command	↓	↓	↓
Output signals				
1	LLEO actuator position, RVDT	LE down	deg streamwise	0.375
2	LLEI actuator position, RVDT	↓	↓	↓
3	RLEI actuator position, RVDT	↓	↓	↓
4	RLEO actuator position, RVDT	↓	↓	↓
5	LTEO actuator position, RVDT	TE down	↓	↓
6	LTEI actuator position, RVDT	↓	↓	↓
7	RTEI actuator position, RVDT	↓	↓	↓
8	RTEO actuator position, RVDT	↓	↓	↓
9	Model pitch actuator position, RVDT	Nose up	deg	↓
10	Model roll position	Right wing down	deg	0.0555
11	LLEO collocated accelerometer	Up	g	0.5
12	RLEO collocated accelerometer	↓	↓	↓
13	LTEO collocated accelerometer	↓	↓	↓
14	LTEI collocated accelerometer	↓	↓	↓
15	RTEI collocated accelerometer	↓	↓	↓
16	RTEO collocated accelerometer	↓	↓	↓
17	Left wingtip accelerometer	↓	↓	↓
18	Right wingtip accelerometer	↓	↓	↓
19	Left store-mounted accelerometer	↓	↓	↓
20	Right store-mounted accelerometer	↓	↓	↓
21	Fuselage accelerometer 1	↓	↓	1.0
22	Fuselage accelerometer 2	↓	↓	1.0
23	Fuselage accelerometer 3	↓	↓	1.0
24	Roll rate	Right wing down	deg/sec	0.0224
25	Left outboard bending moment	Tip up	in-lb	.00244
26	Left inboard bending moment	↓	↓	.000477
27	Right inboard bending moment	↓	↓	.000553
28	Right outboard bending moment	↓	↓	.002820
29	Left outboard torsion moment	LE up	↓	.00611
30	Left inboard torsion moment	↓	↓	.000112
31	Right inboard torsion moment	↓	↓	.000106
32	Right outboard torsion moment	↓	↓	.00702
33	LLEO actuator hinge moment	↓	↓	.014760
34	LLEI actuator hinge moment	↓	↓	.014144
35	RLEI actuator hinge moment	↓	↓	.014155
36	RLEO actuator hinge moment	↓	↓	.020503
37	LTEO actuator hinge moment	TE up	↓	.026917
38	LTEI actuator hinge moment	↓	↓	.014592
39	RTEI actuator hinge moment	↓	↓	.013616
40	RTEO actuator hinge moment	↓	↓	.028341
41	Wind tunnel Mach number	Not applicable	Mach number	10.0
42	Wind tunnel dynamic pressure	Not applicable	psi	0.006945

Table II. Structural Model Variations

	Symmetric about X-Z plane	Antisymmetric—	
		Fixed in roll	Free to roll
Wingtip store coupled	Yes	Yes	Yes
Wingtip store uncoupled	Yes	Yes	Yes

Table III. Structural Mode Frequencies in Simulation With Wingtip Store Coupled

Structured model variation			Frequencies, Hz, for—										
			Roll mode	Elastic mode—									
			R1	E1	E2	E3	E4	E5	E6	E7	E8	E9	E10
Symmetric	1989	Predicted		5.646	6.213	12.01	12.85	22.34	26.73	35.74	39.53	41.13	51.19
	1989	Measured		5.77	7.22	13.13	14.65		32.2	39.9	42.7	49.1	
	1989	Used		5.77	7.22	13.13	14.65		32.22	39.9	42.7	49.1	
	1991	Predicted		5.35	7.31	12.85	14.79	28.57	32.08	39.93	43.85	47.57	53.38
	1991	Used		5.31	7.17	11.65	13.5	28.57	32.22	39.9	38.62	46.98	53.38
Antisymmetric, fixed in roll	1989	Predicted		5.81	7.07	11.52	15.41	17.46	28.00	38.30	39.70	41.37	49.90
	1989	Measured		6.36	5.51	13.61		18.3	34.4	44.5			
	1989	Used		6.36	5.51	13.61		18.3	34.4	44.5		48.07	
	1991	Predicted		6.24	6.81	13.02	13.70	17.88	31.84	34.73	40.00	45.58	47.66
	1991	Used		5.84	6.36	12.6	13.24	19.46	34.4	34.73	40.00	44.65	
Antisymmetric, free to roll	1991	Used	0.3503	5.933	8.445	13.15	15.14	34.64	36.57	39.94	45.58	46.65	

Table IV. Summary of Defining Equations

Subsystem	Defining equation numbers
Turbulence models	(14), (15), (17)
Actuator models	(18), (19), (20), (21), (22), (23)
Aeroservoelastic models	(29), (30)
Antialiasing filters	(31)

Table V. Predicted Versus Measured Flutter Characteristics

[AFW model; Mach = 0.5; in air; wingtip store coupled]

Model variation	1989 predicted—		1991 predicted—		1991 measured—		1991 error, percent—	
	Frequency, Hz	Dynamic pressure, psf	Frequency, Hz	Dynamic pressure, psf	Frequency, Hz	Dynamic pressure, psf	Frequency, Hz	Dynamic pressure, psf
Symmetric	11.2	239.3	11.2	248	9.6	235	16	6
Antisymmetric, fixed in roll	11.6	256.5	10.9	233	9.1	219	13	6
Antisymmetric, free to roll			12.7	432				

Table VI. 1989 and 1991 Simulation Mathematical Models

(a) Simulation characteristics

Simulation characteristics	1989 test year	1991 test year
RFA methodology for unsteady aerodynamic models	Least-squares with 1-lag state per mode	Least-squares with 4-lag states per mode
Dryden-like turbulence models with break frequencies at 17.23 Hz:		
Symmetric intensity, in/sec	10.2	$0.4 + 1.0\left(\frac{\bar{q}}{100}\right)$
Antisymmetric intensity, in/sec	1.8	$1.6 + 2.4\left(\frac{\bar{q}}{100}\right)$

(b) Simulation states

Simulation states	Number of states for—	
	1989 test year	1991 test year
Symmetric elastic mode states (positions and velocities)	16	20
Symmetric aerodynamic lag states associated with elastic modes	8	40
Symmetric aerodynamic lag states associated with control modes	4	16
Symmetric turbulence states	2	2
Antisymmetric rigid and elastic mode states (positions and velocities)	14	20
Antisymmetric aerodynamic lag states associated with flexible modes	7	40
Antisymmetric aerodynamic lag states associated with control modes	4	16
Antisymmetric turbulence states	2	2
Linear actuator states, 2 per actuator, 8 actuators	16	16
Subtotal of coupled linear aeroservoelastic component model	73	172
Nonlinear actuator states, 1 per actuator, 8 actuators	8	8
Antialiasing filters on 40 channels	40	40
Total of simulation states	121	220

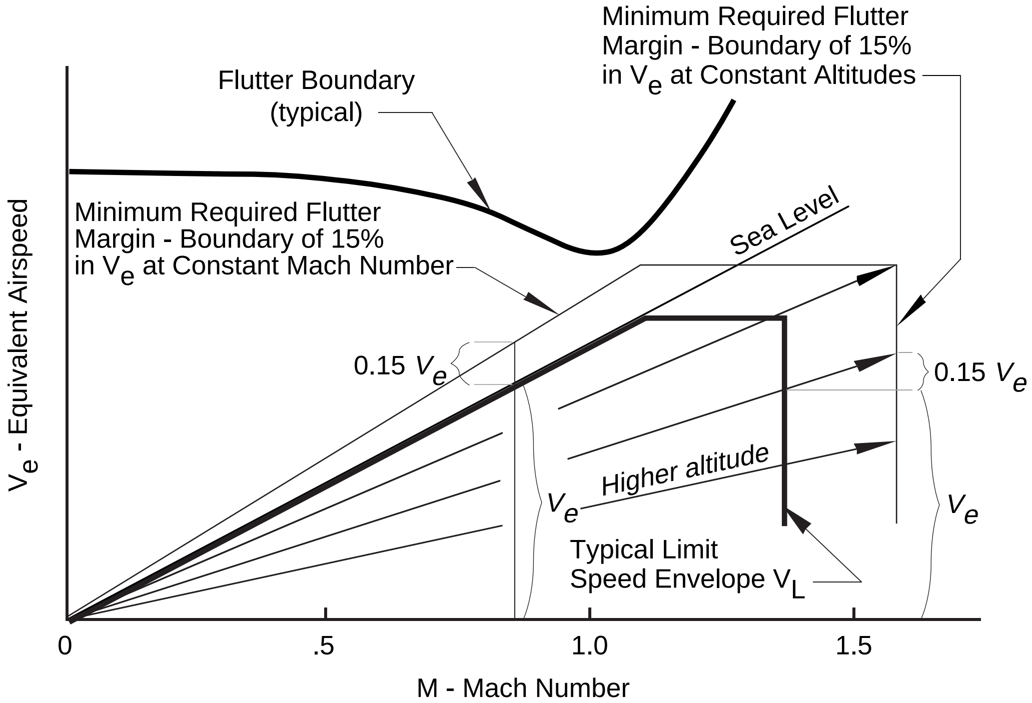

Figure 1. Graphical representation of minimum flutter margin as required by MIL-A-8870B (taken from MIL-A-8870B). Notations in italics added by authors.

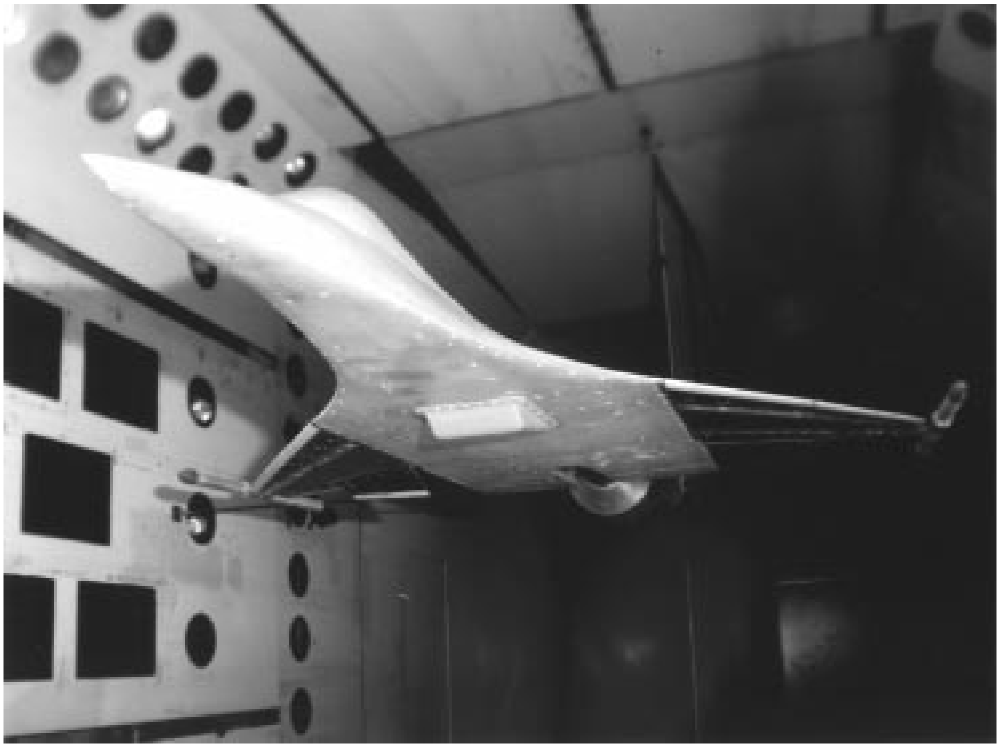

L-89-12445

Figure 2. AFW wind tunnel model mounted in TDT.

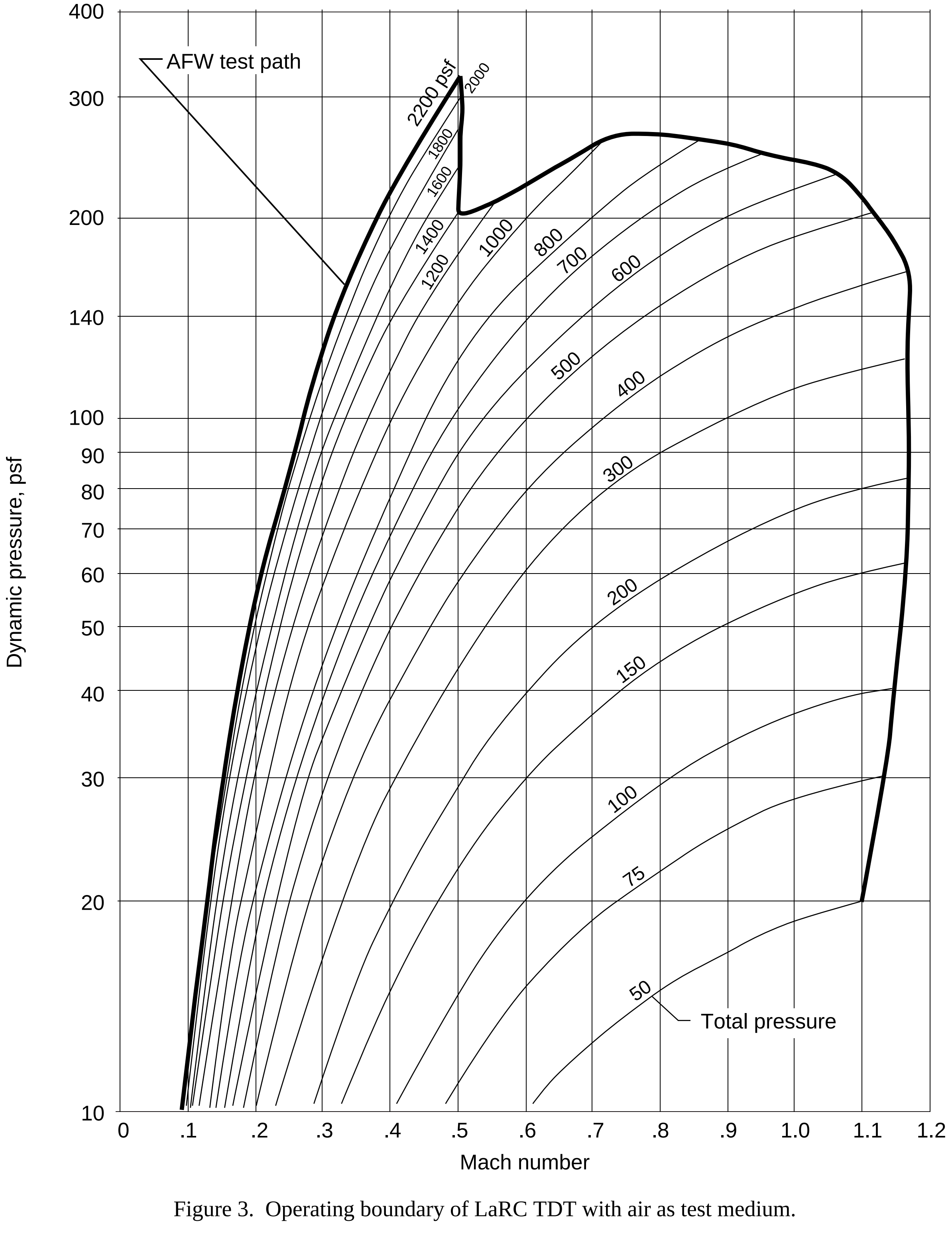

Figure 3. Operating boundary of LaRC TDT with air as test medium.

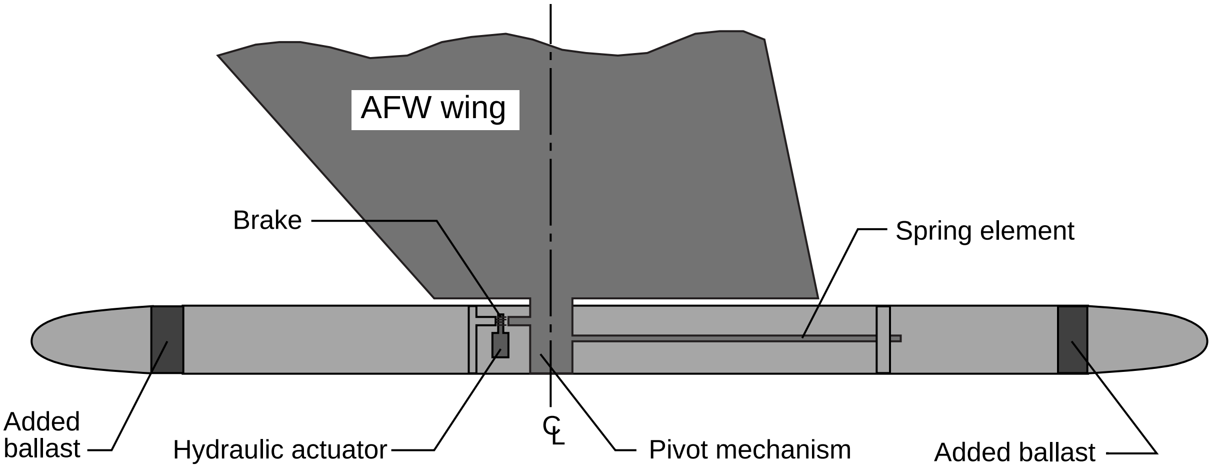
AFW wing
Brake
Spring element
Added ballast
Hydraulic actuator
C
L
Pivot mechanism
Added ballast

Figure 4. Wingtip ballast store (from Perry, Cole, and Miller (1992)).

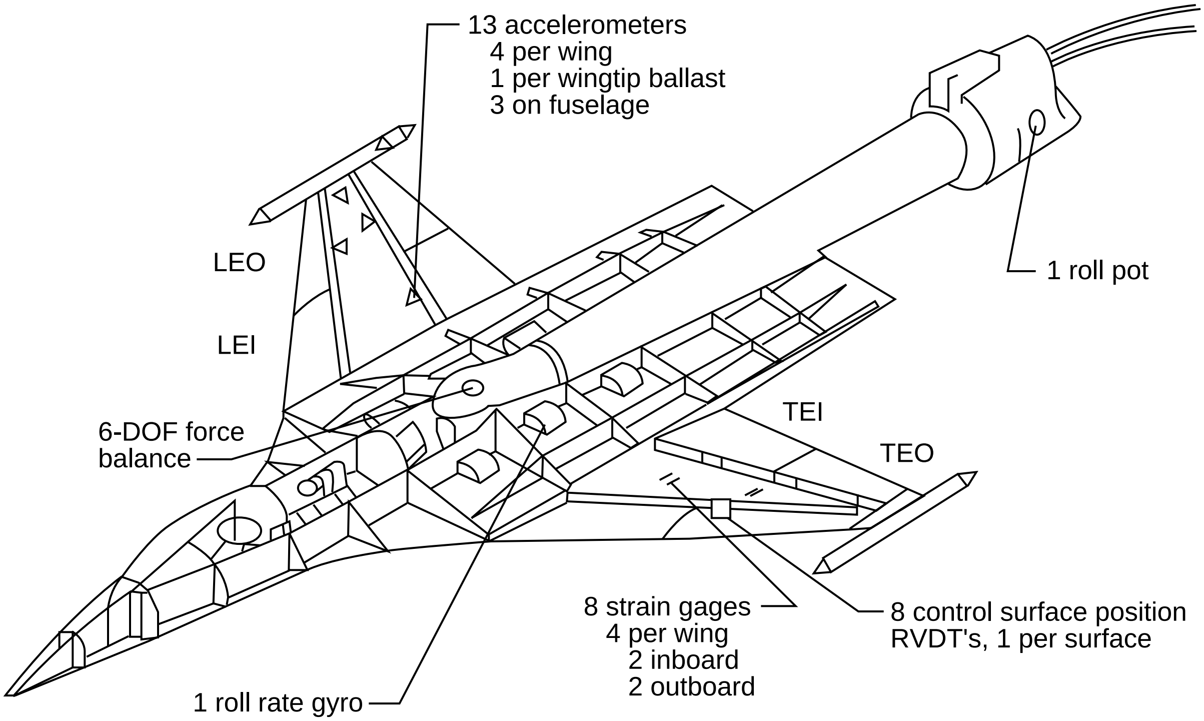
13 accelerometers
4 per wing
1 per wingtip ballast
3 on fuselage
LEO
LEI
1 roll pot
6-DOF force balance
TEI
TEO
8 strain gages
4 per wing
2 inboard
2 outboard
8 control surface position RVDT's, 1 per surface
1 roll rate gyro

Figure 5. Instrumentation of AFW wind tunnel model.

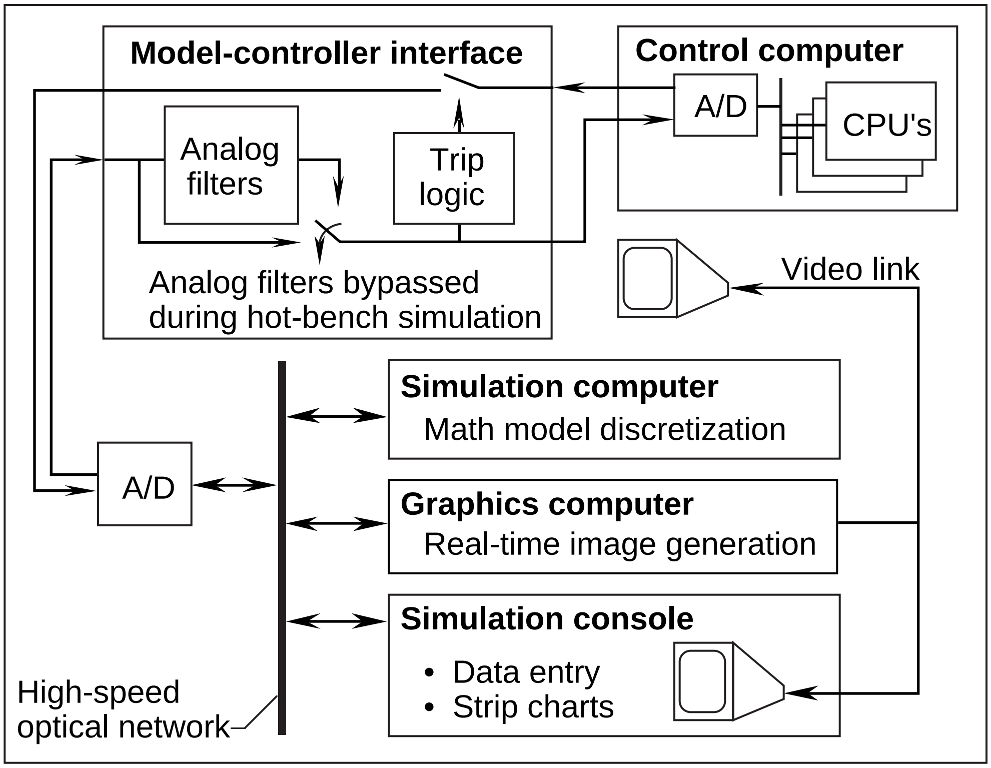
Model-controller interface
Control computer
A/D
CPU's
Analog filters
Trip logic
Analog filters bypassed during hot-bench simulation
Video link
Simulation computer
Math model discretization
A/D
Graphics computer
Real-time image generation
Simulation console
• Data entry
• Strip charts
High-speed optical network

Figure 6. Schematic of AFW hot-bench simulation laboratory.

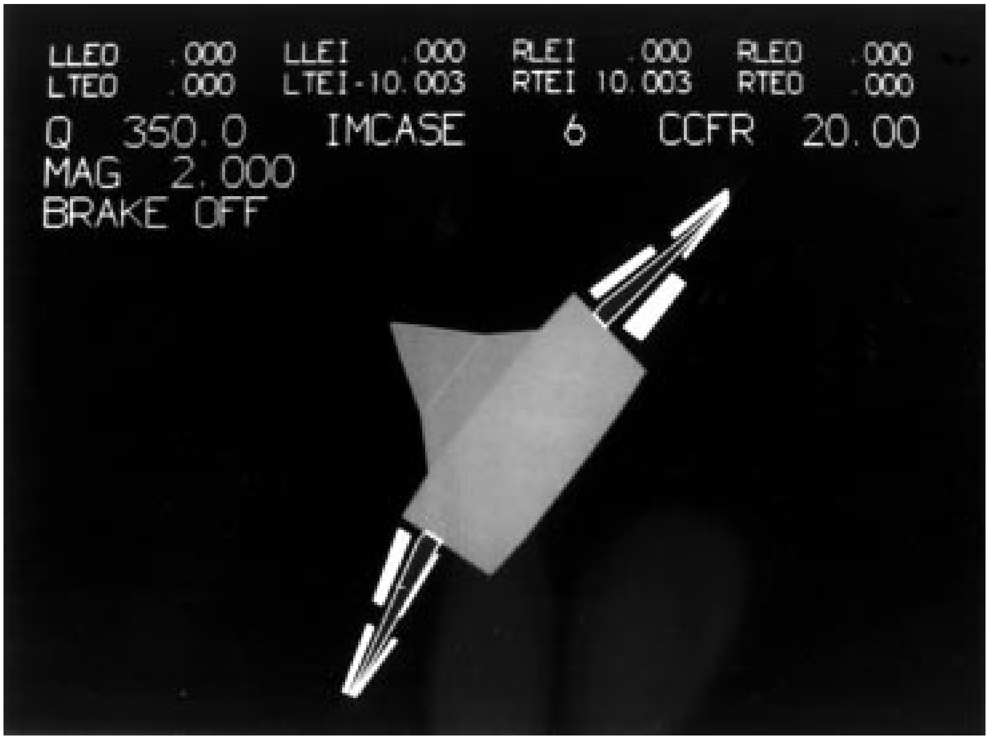
LLEO .000 LLEI .000 RLEI .000 RLEO .000
LTEO .000 LTEI -10.003 RTEI 10.003 RTEO .000
Q 350.0 IMCASE 6 CCFR 20.00
MAG 2.000
BRAKE OFF

L-91-03116

Figure 7. Hot-bench real-time display.

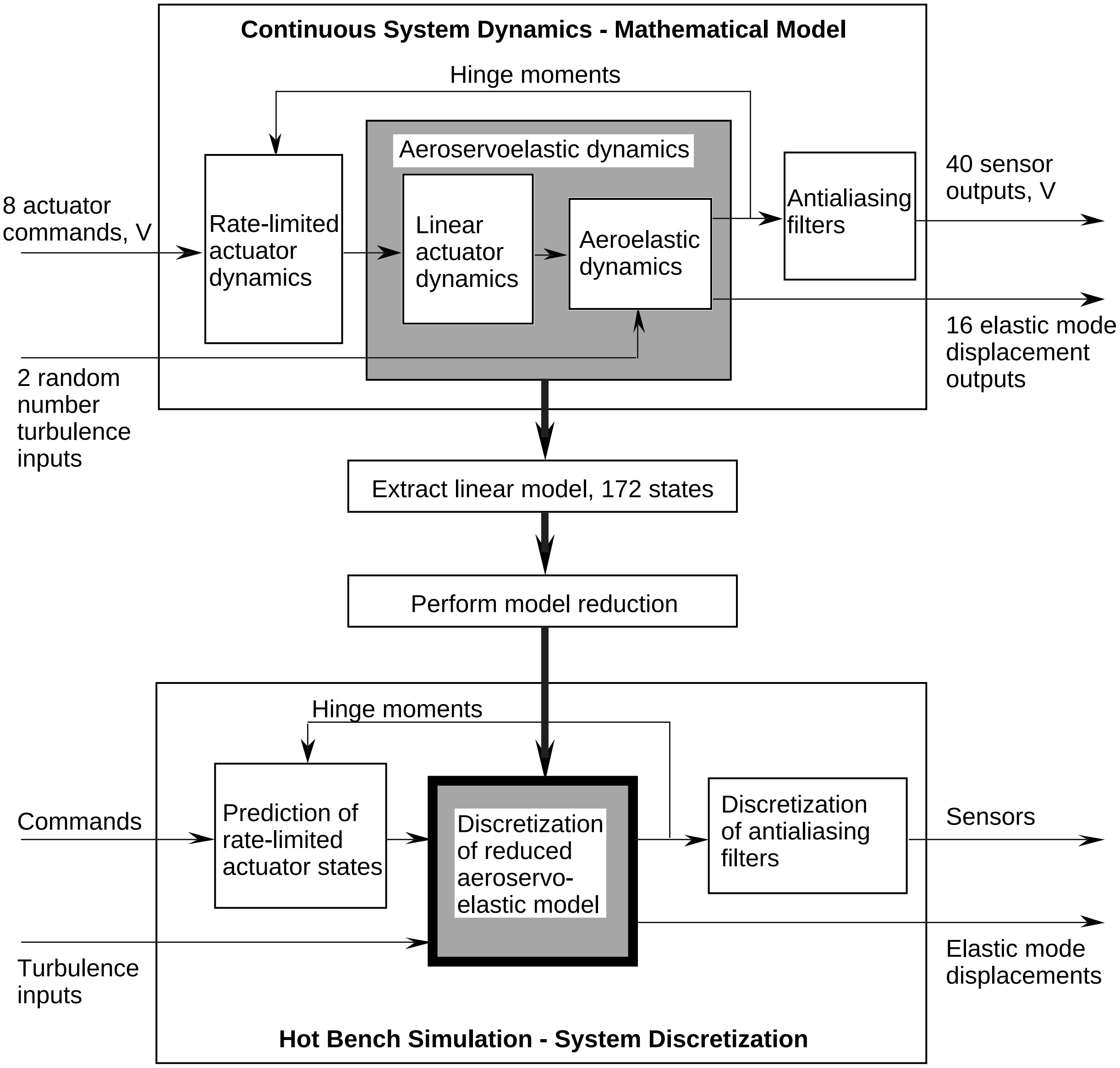
Continuous System Dynamics - Mathematical Model
Hinge moments
Aeroservoelastic dynamics
8 actuator commands, V
Rate-limited actuator dynamics
Linear actuator dynamics
Aeroelastic dynamics
Antialiasing filters
40 sensor outputs, V
16 elastic mode displacement outputs
2 random number turbulence inputs
Extract linear model, 172 states
Perform model reduction
Hinge moments
Commands
Prediction of rate-limited actuator states
Discretization of reduced aeroservo-elastic model
Discretization of antialiasing filters
Sensors
Elastic mode displacements
Turbulence inputs
Hot Bench Simulation - System Discretization

Figure 8. Data flow from batch to hot-bench simulation.

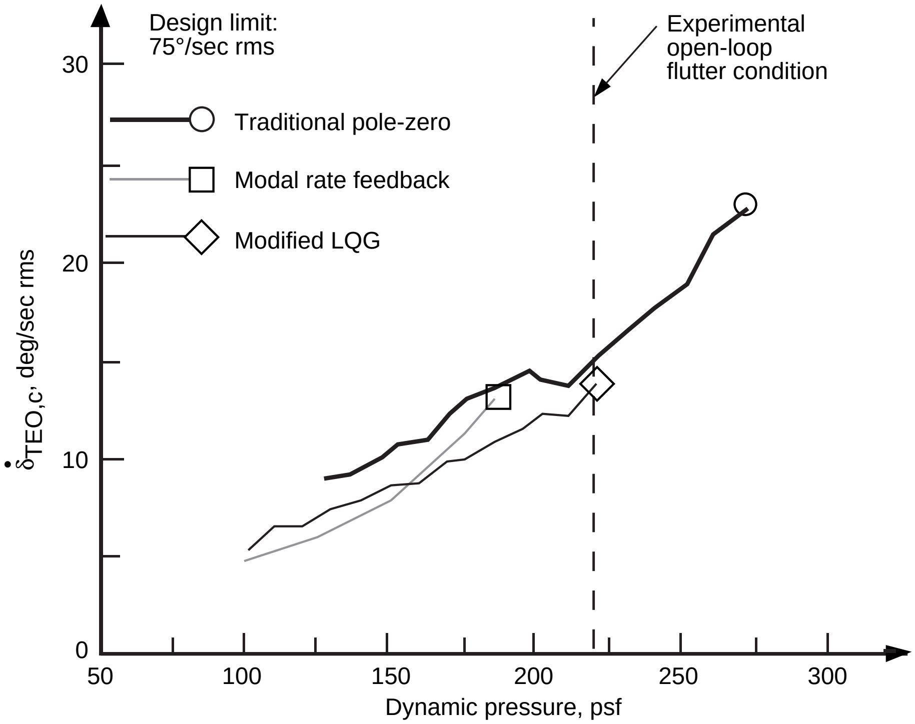

Figure 9. Experimentally determined rms control rates. (From fig. 19 of Adams et al. (1992).)

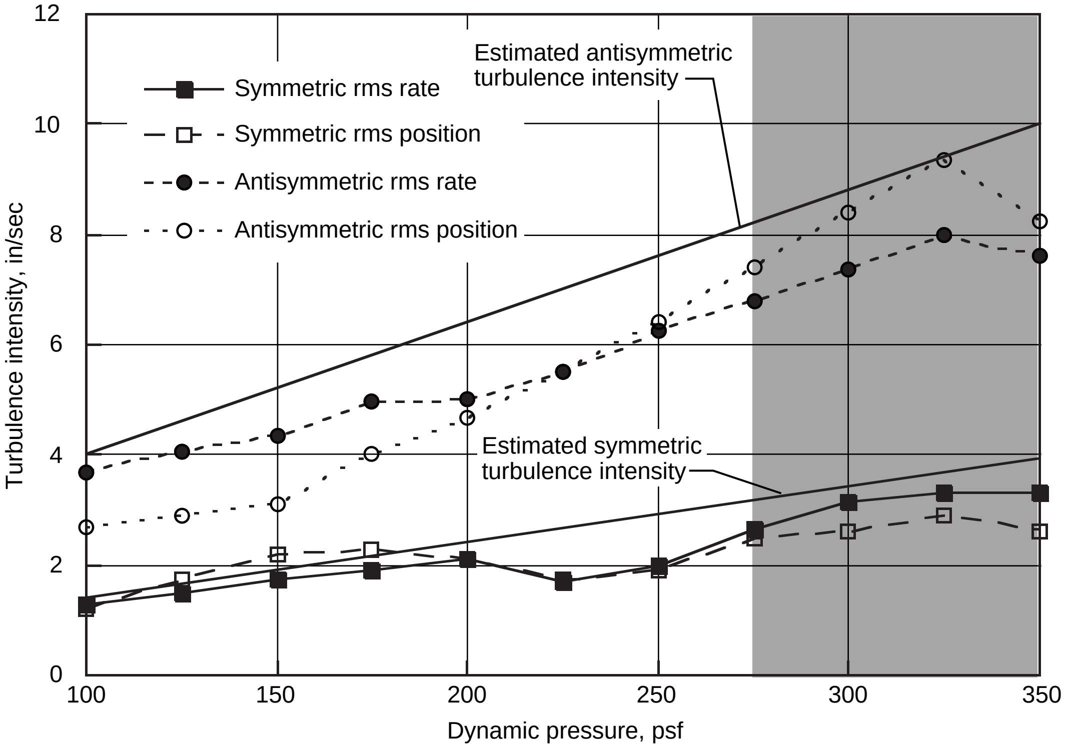

Figure 10. Turbulence intensities used for 1991 simulation derived from 1989 test results. Experimental target control surface activity measurements only available below 275 psf.

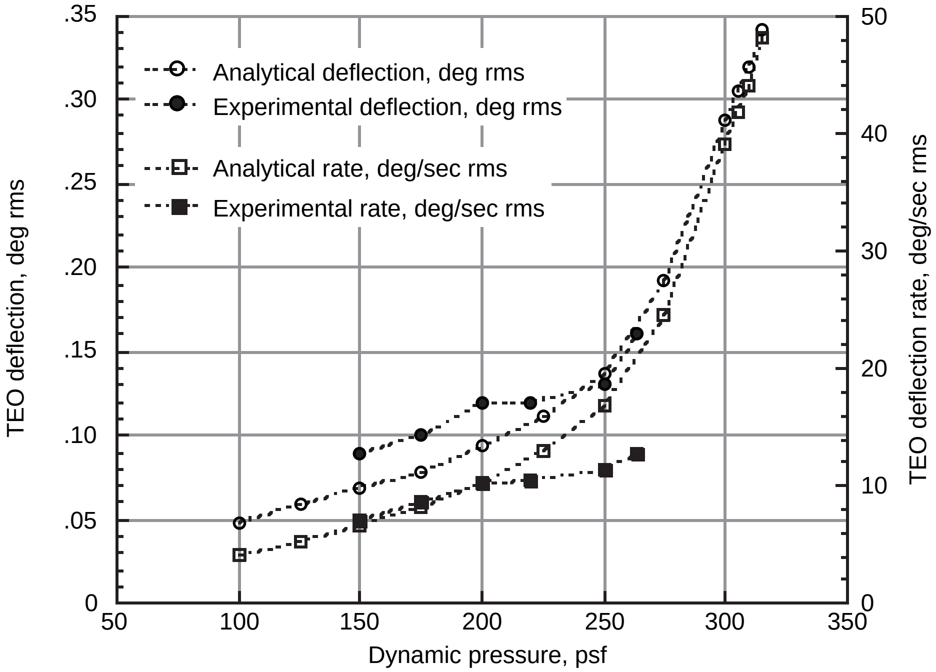

Figure 11. Predicted versus measured rms TEO control activity (roll brake on) for traditional pole-zero flutter suppression control law during 1991 tunnel test.

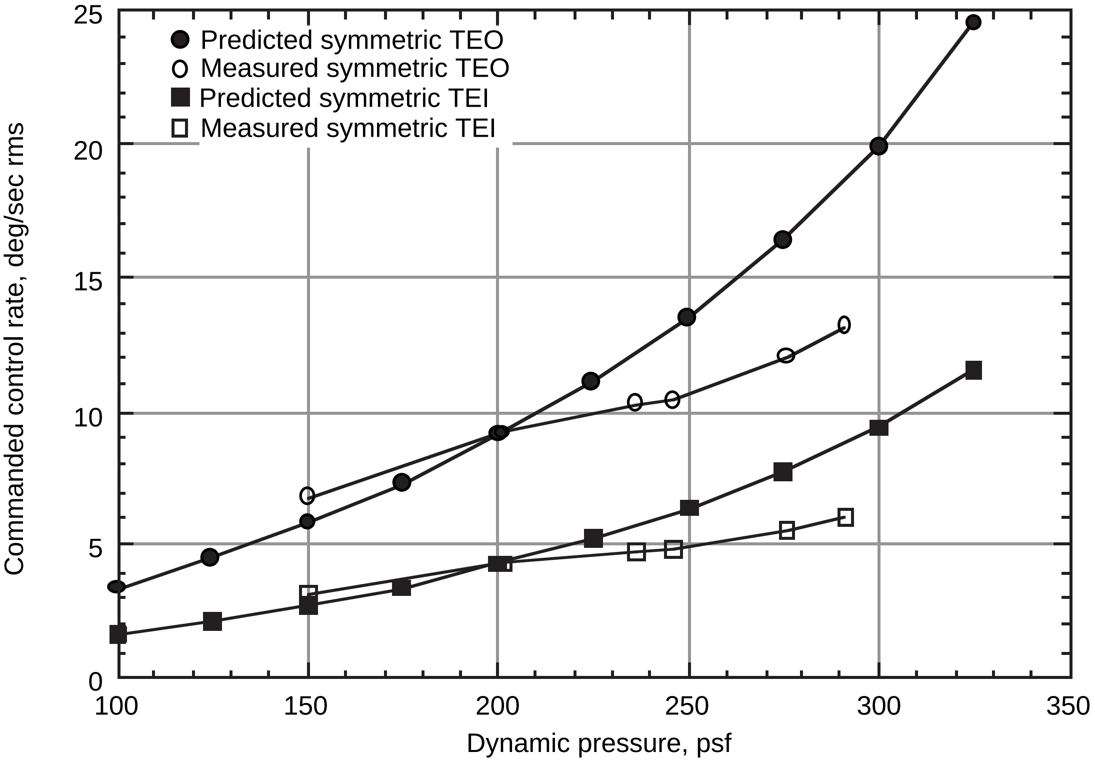

Figure 12. Comparison of predicted versus measured control activity for representative flutter suppression law during 1991 tunnel test. (From fig. 13 of Christhilf and Adams (1992).)

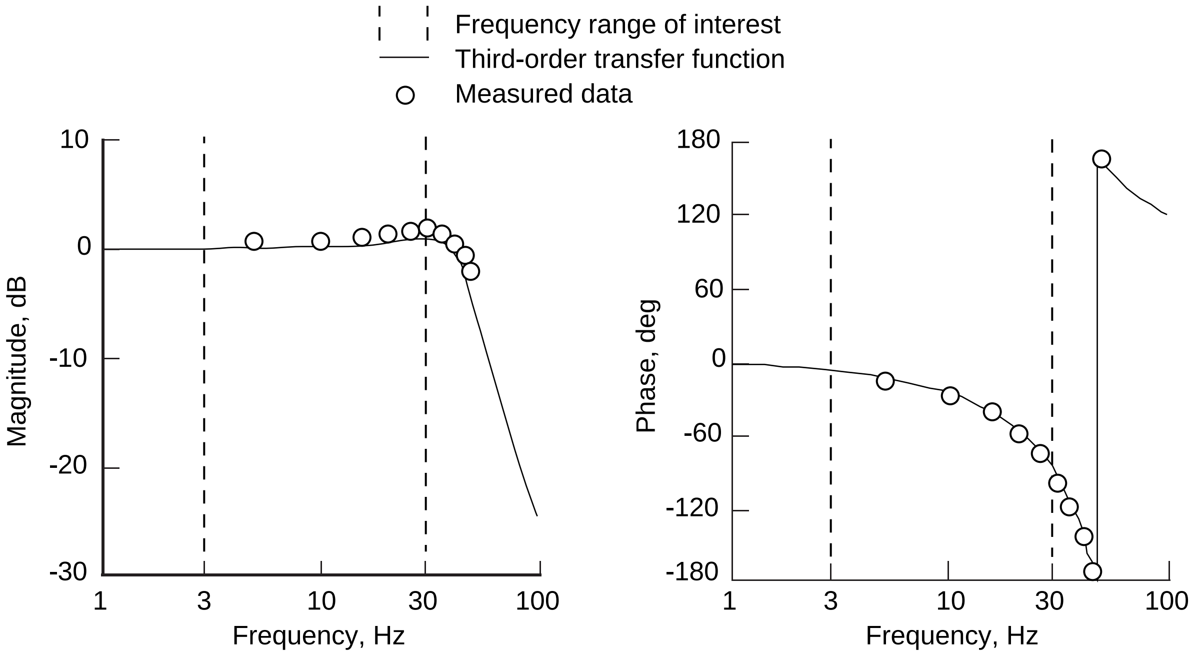

Figure 13. Magnitude and phase response of third-order analytical transfer function actuator model and measured data used for its derivation.

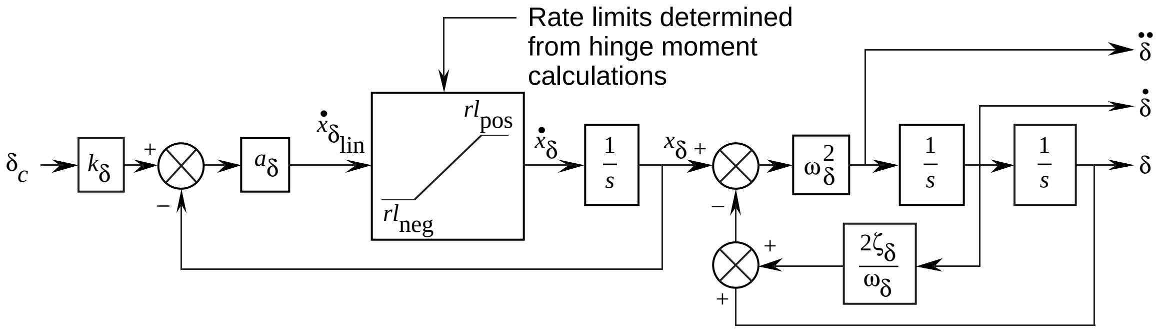
Rate limits determined from hinge moment calculations
δ_c
k_δ
+
−
a_δ
$\dot{x}_{\delta_{lin}}$
rl_{pos}
rl_{neg}
$\dot{x}_\delta$
$\frac{1}{s}$
x_δ
+
−
ω_δ^2
$\frac{1}{s}$
$\frac{1}{s}$
$\ddot{\delta}$
$\dot{\delta}$
δ
+
+
$\frac{2\zeta_\delta}{\omega_\delta}$

Figure 14. Mechanization of actuator transfer functions with rate limiting.

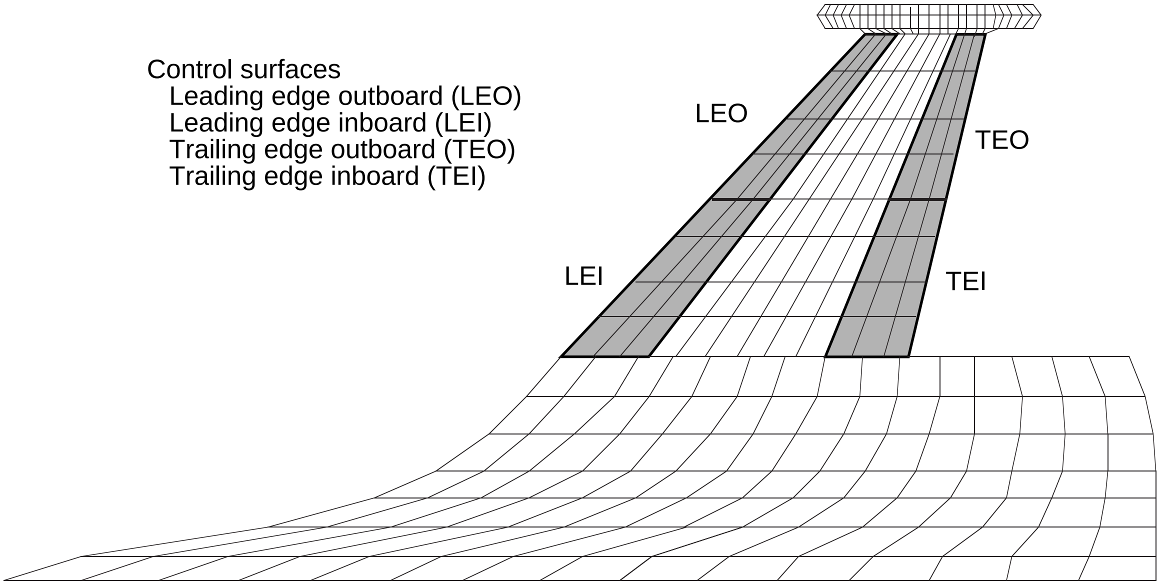
Control surfaces
Leading edge outboard (LEO)
Leading edge inboard (LEI)
Trailing edge outboard (TEO)
Trailing edge inboard (TEI)
LEO
TEO
LEI
TEI

Figure 15. Doublet-lattice aerodynamic box layout.

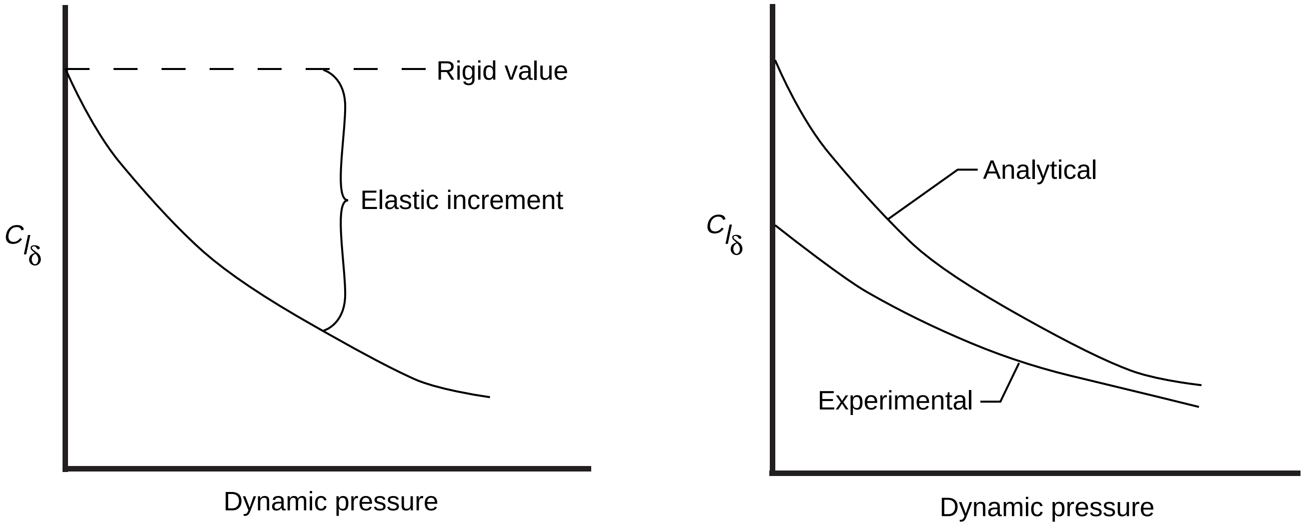

(a) Decomposition of C_l due to control deflection into rigid term and elastic increment.

(b) Analytical and experimental control effectiveness versus dynamic pressure.

Figure 16. Examples of rolling-moment coefficient decomposition and control effectiveness.

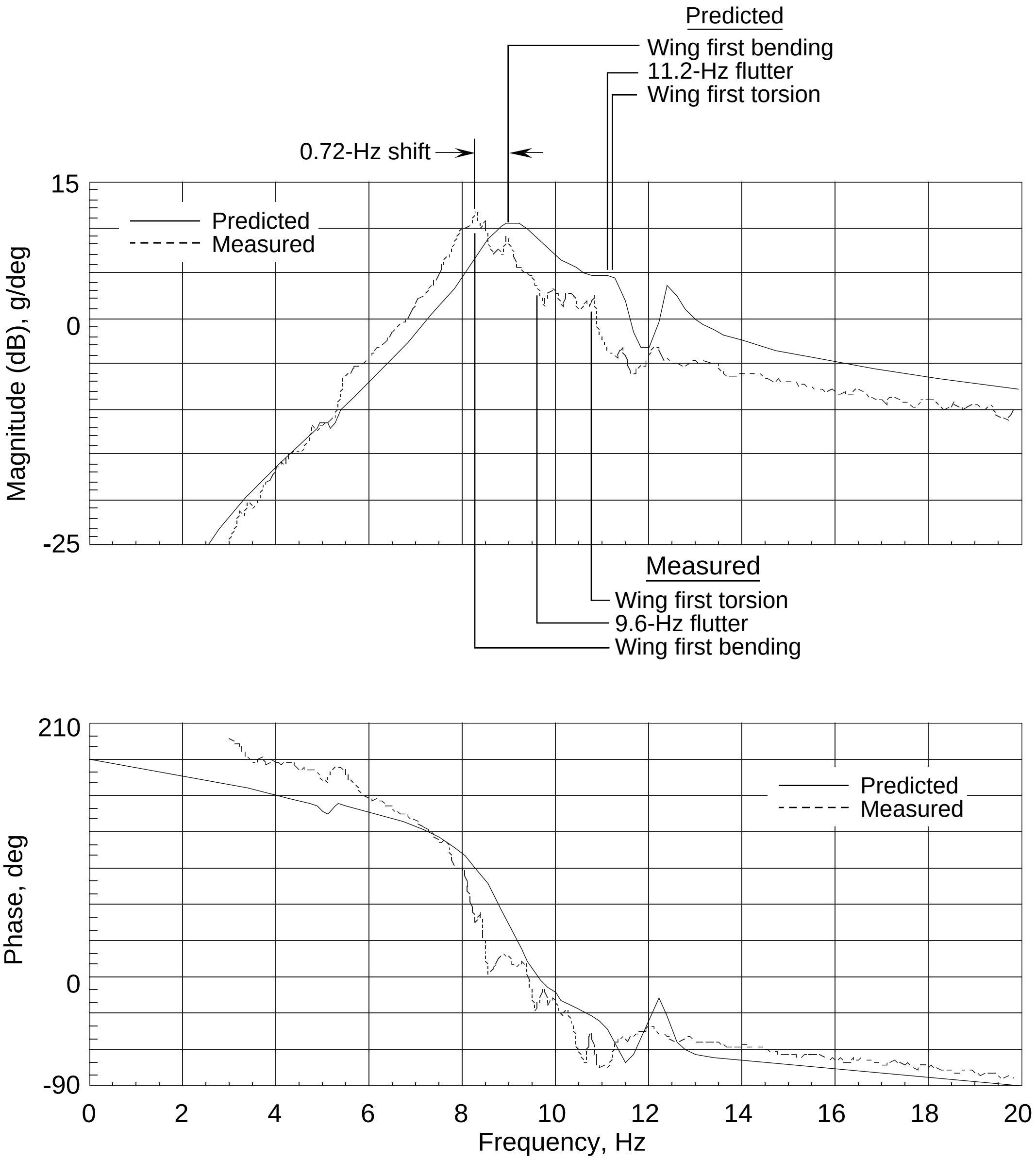

Figure 17. Predicted (1991) versus measured (1991 test data by Adams and Christhilf) magnitude and phase responses of symmetric component of wingtip accelerometer signal to commanded TEO control surface at 225 psf shown as functions of frequency.

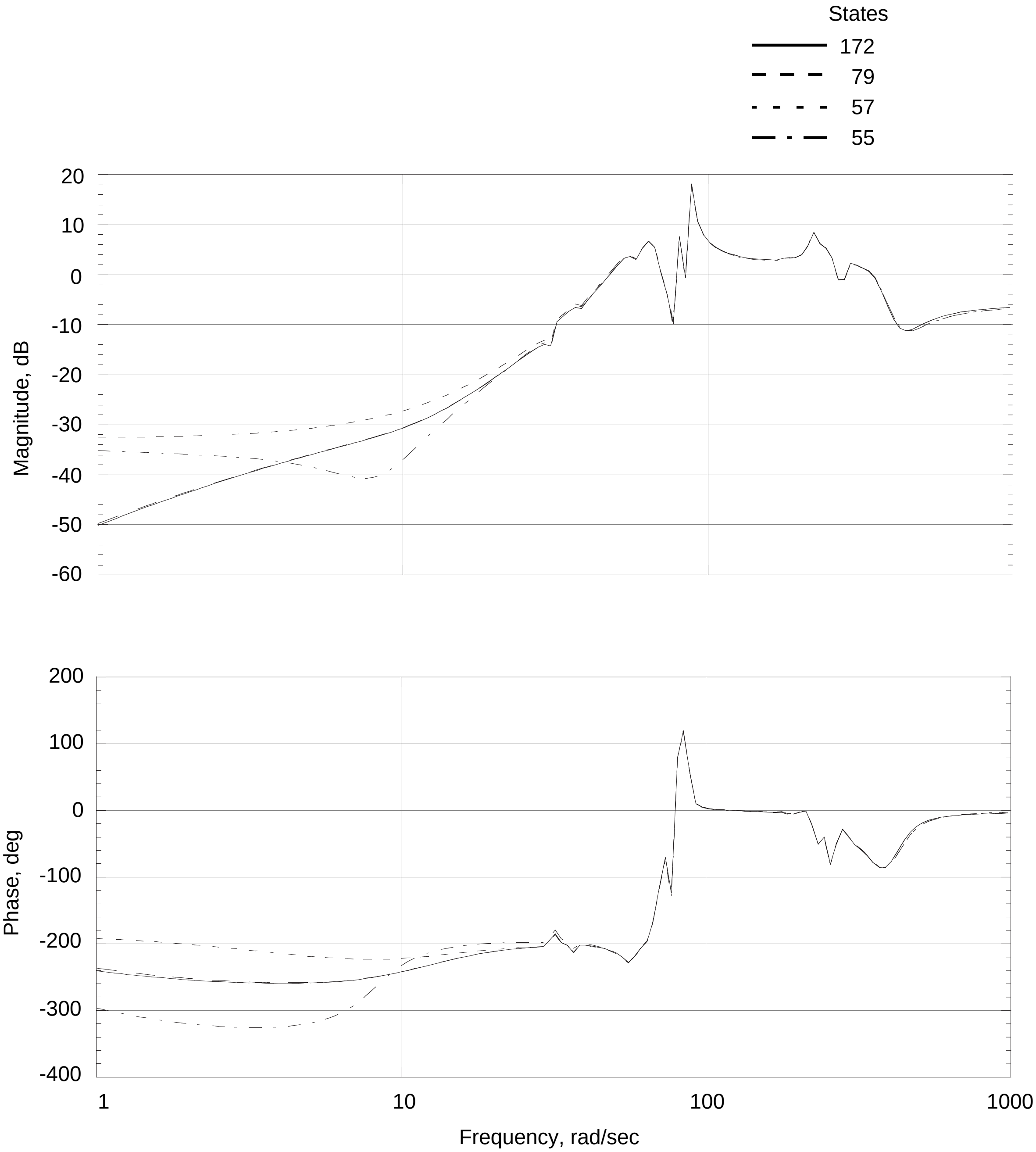

Figure 18. Frequency response of right wingtip accelerometer to commanded RTEO control for various levels of model reduction at dynamic pressure of 300 psf for free-to-roll 1991 model.

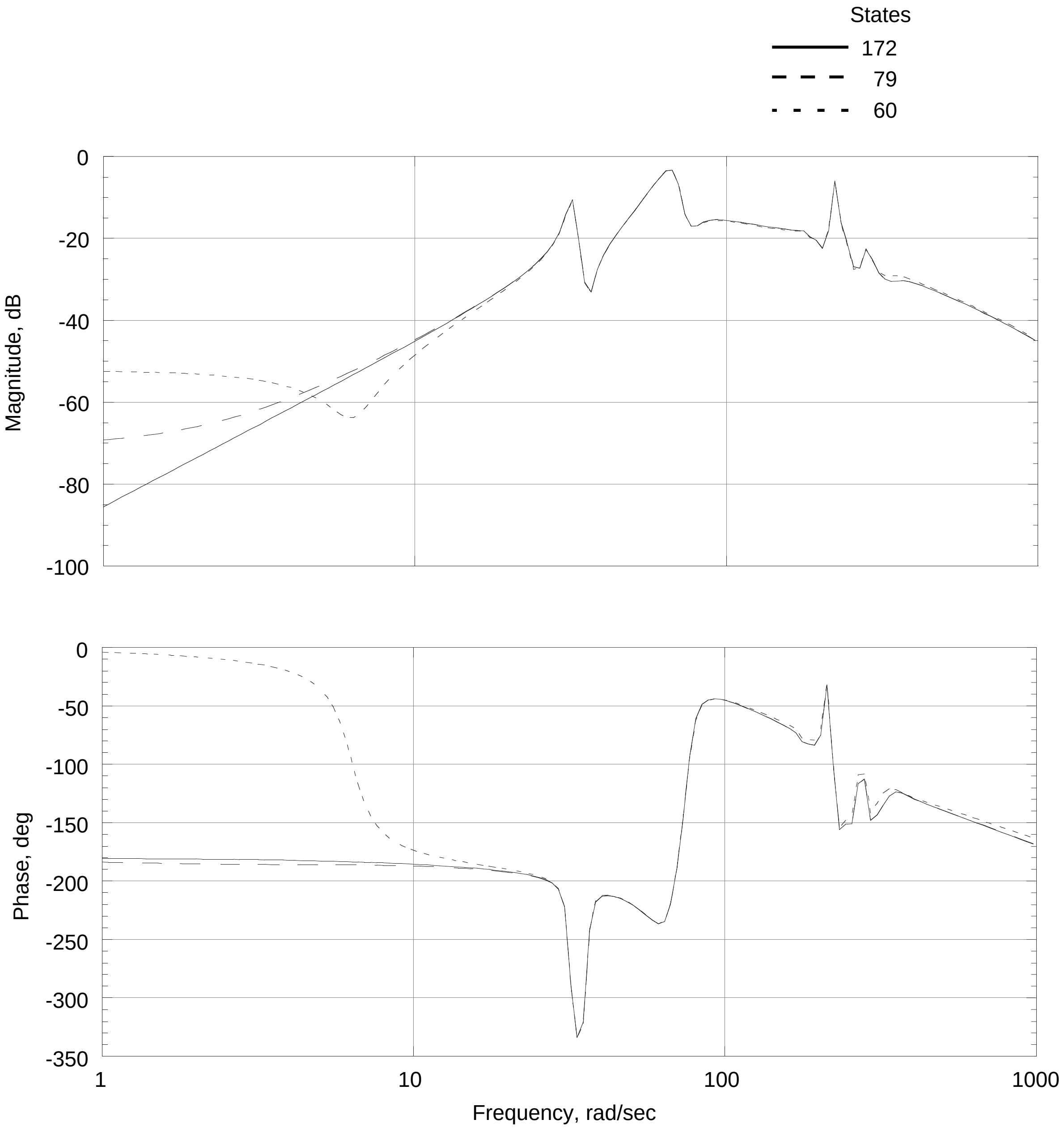

Figure 19. Frequency response of right wingtip accelerometer to symmetric turbulence input for various levels of model reduction at dynamic pressure of 300 psf for free-to-roll 1991 model.

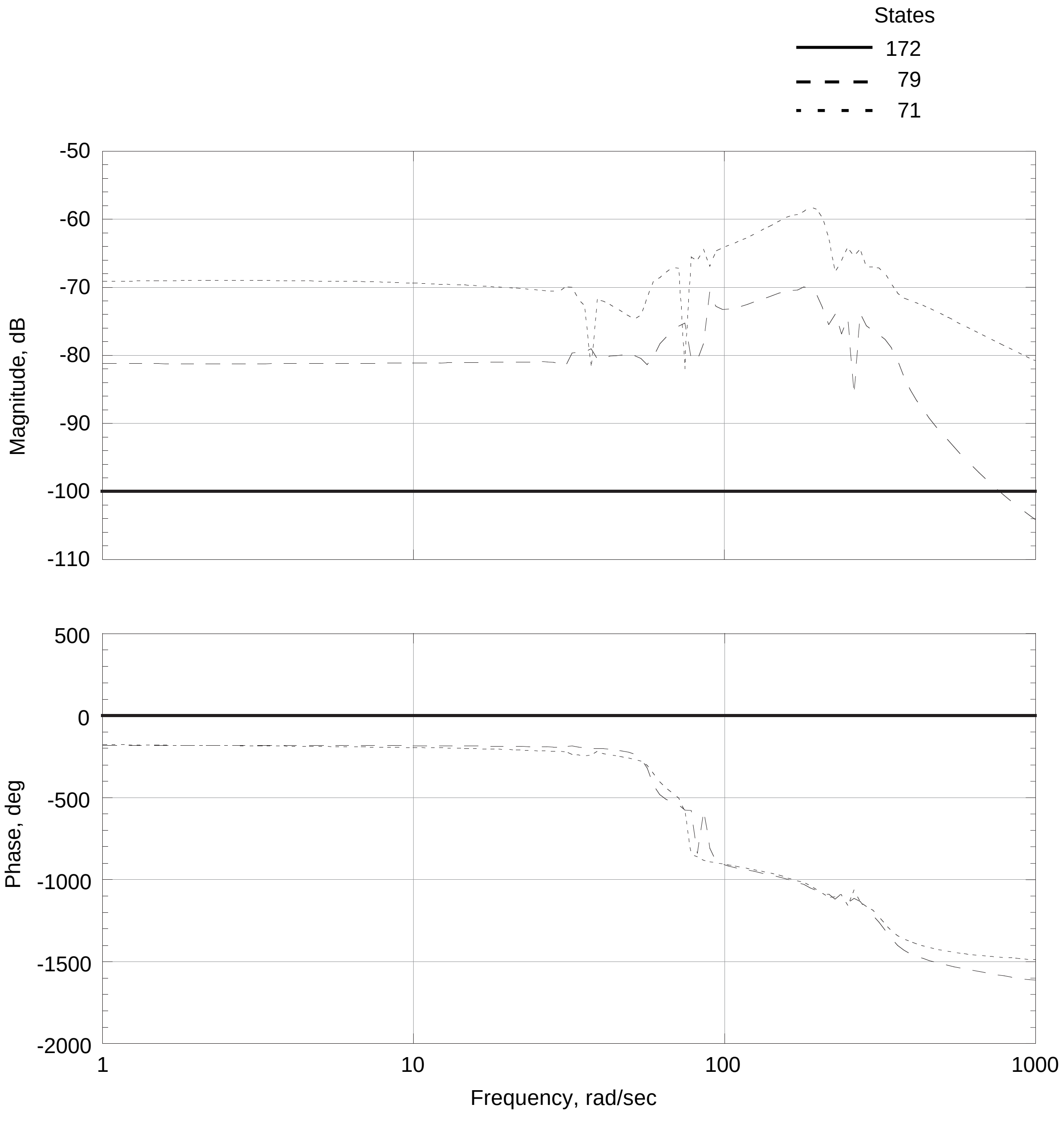

Figure 20. Frequency responses of LLEO control surface to command at RTEO actuator for various levels of model reduction at dynamic pressure of 300 psf for free-to-roll 1991 model.

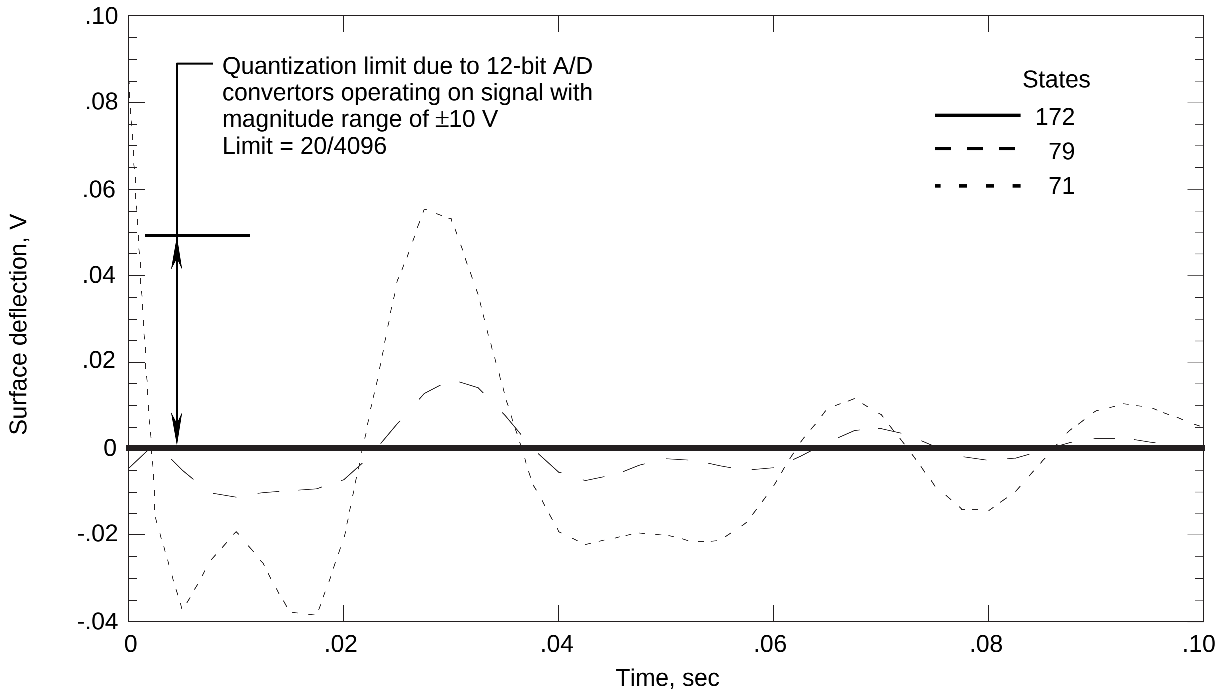

Figure 21. Predicted time response (ideally zero) of LLEO control surface to unit impulse command at RTEO actuator for various levels of model reduction at dynamic pressure of 300 psf for free-to-roll 1991 model.

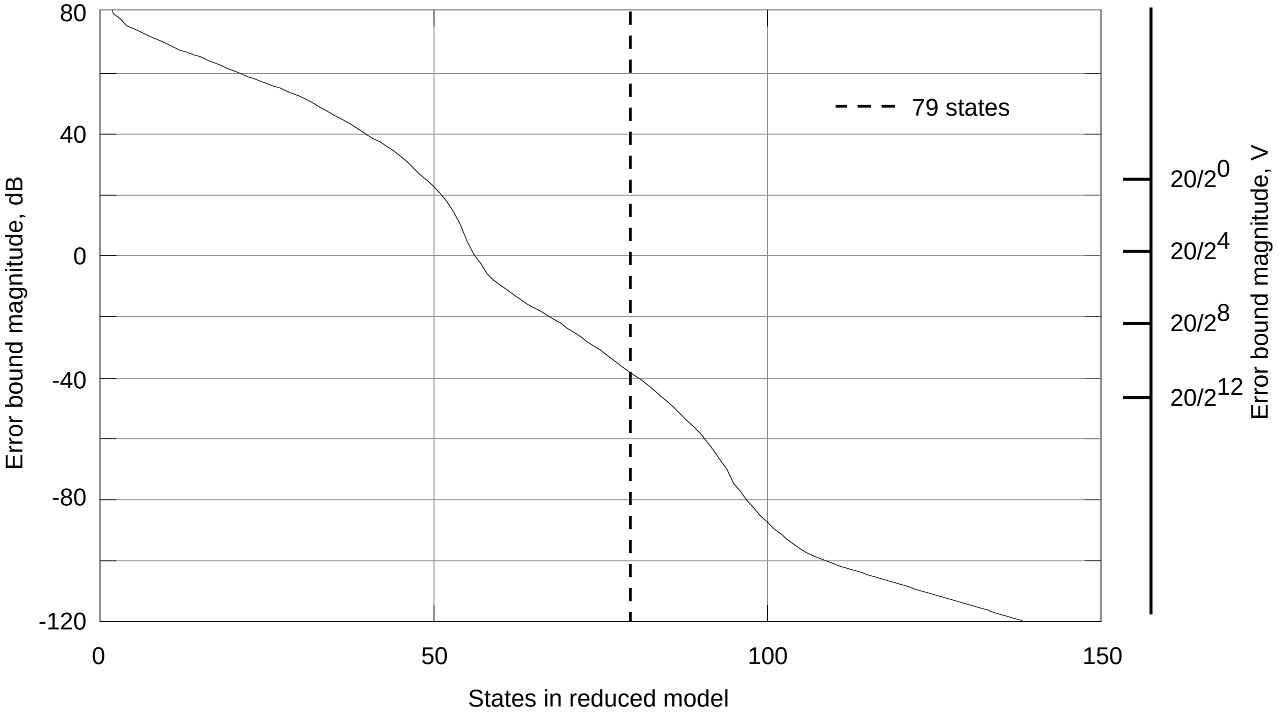

Figure 22. Error bound versus number of states for aeroelastic submodel at dynamic pressure of 300 psf for free-to-roll 1991 model.

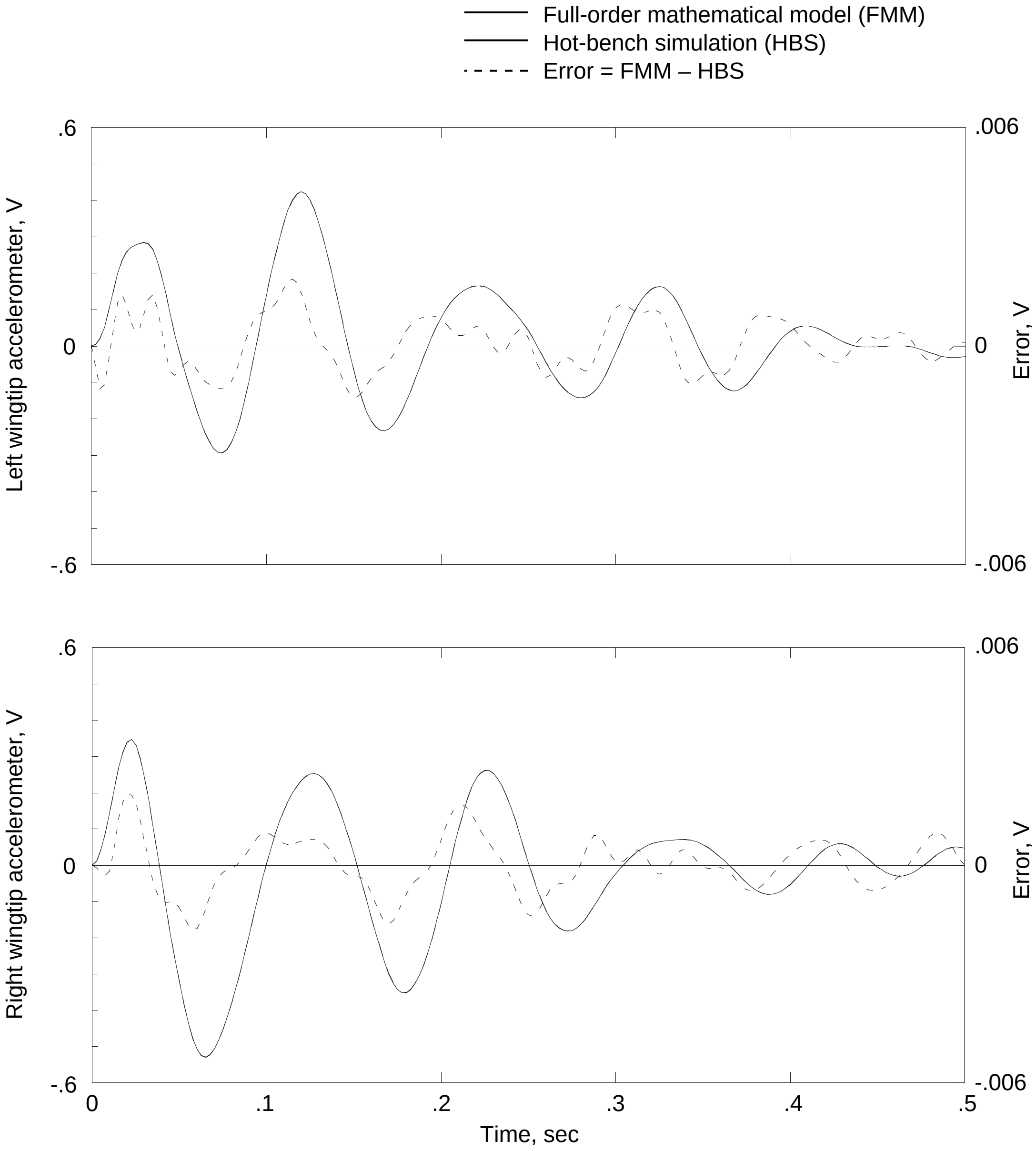

Figure 23. Error between full-order mathematical model and hot-bench simulation with 79-state aeroservoelastic submodel for left and right wingtip accelerometers for 1-V step command to RTEO control surface at dynamic pressure of 225 psf for free-to-roll model.

REPORT DOCUMENTATION PAGE

Form Approved
OMB No. 0704-0188

Public reporting burden for this collection of information is estimated to average 1 hour per response, including the time for reviewing instructions, searching existing data sources, gathering and maintaining the data needed, and completing and reviewing the collection of information. Send comments regarding this burden estimate or any other aspect of this collection of information, including suggestions for reducing this burden, to Washington Headquarters Services, Directorate for Information Operations and Reports, 1215 Jefferson Davis Highway, Suite 1204, Arlington, VA 22202-4302, and to the Office of Management and Budget, Paperwork Reduction Project (0704-0188), Washington, DC 20503.

1. AGENCY USE ONLY *(Leave blank)*

2. REPORT DATE
April 1996

3. REPORT TYPE AND DATES COVERED
Technical Paper

4. TITLE AND SUBTITLE
Aeroservoelastic Simulation of an Active Flexible Wing Wind Tunnel Model

5. FUNDING NUMBERS
WU 505-64-52-01

6. AUTHOR(S)
Carey S. Buttrill, Barton J. Bacon, Jennifer Heeg, Jacob A. Houck, and
David V. Wood

7. PERFORMING ORGANIZATION NAME(S) AND ADDRESS(ES)
NASA Langley Research Center
Hampton, VA 23681-0001

8. PERFORMING ORGANIZATION REPORT NUMBER
L-17276

9. SPONSORING/MONITORING AGENCY NAME(S) AND ADDRESS(ES)
National Aeronautics and Space Administration
Washington, DC 20546-0001

10. SPONSORING/MONITORING AGENCY REPORT NUMBER
NASA TP-3510

11. SUPPLEMENTARY NOTES
Buttrill, Bacon, Heeg, and Houck: Langley Research Center, Hampton, VA; Wood: Unisys Corporation, Hampton, VA.

12a. DISTRIBUTION/AVAILABILITY STATEMENT
Unclassified–Unlimited
Subject Category 05
Availability: NASA CASI (301) 621-0390

12b. DISTRIBUTION CODE

13. ABSTRACT *(Maximum 200 words)*

Mathematical models and implementation issues are described for simulations developed in the active flexible wing wind tunnel test program, which resulted in successful application of active flutter control. The wind tunnel test program required a truth batch simulation for off-line tests of proposed control designs and functional, hot-bench tests of digital controller hardware and software. To provide the hot-bench test environment, a real-time simulation of the wind tunnel model and test environment was desired. Although mathematical model complexity and computing power limitations prevented attainment of real-time operation, essential test goals were met with a hot-bench simulation running at a timescale ratio no slower than 1:5. To achieve the required timescale, model reduction methods were applied to the aeroservoelastic portion of the full-order mathematical model. The reduction method was based on the internally balanced realization of a linear dynamic system. The error-bound properties of the internally balanced realization contributed to the method utility in the model reduction process. The state dimensions of the aeroservoelastic model were reduced by a factor of 2. The errors due to reduction appeared beyond the 10th bit of the analog-to-digital converters for all 560 combinations of simulation inputs and outputs.

14. SUBJECT TERMS
AFW; Active flexible wing; Aeroservoelastic simulation; Model reduction; Turbulence; Real-time simulation

15. NUMBER OF PAGES
57

16. PRICE CODE
A04

17. SECURITY CLASSIFICATION OF REPORT
Unclassified

18. SECURITY CLASSIFICATION OF THIS PAGE
Unclassified

19. SECURITY CLASSIFICATION OF ABSTRACT
Unclassified

20. LIMITATION OF ABSTRACT

NSN 7540-01-280-5500

Standard Form 298 (Rev. 2-89)
Prescribed by ANSI Std. Z39-18
298-102